# Synthesis, Characterization, and Photophysical Investigations of Doped Semiconductor Nanocrystals

BY

ASRA HASSAN
B.Sc., University of Illinois at Chicago, 2013

THESIS

Submitted as partial fulfillment of the requirements
for the degree of Doctor of Philosophy in Chemistry
in the Graduate College of the
University of Illinois at Chicago, 2018

Chicago, Illinois

Defense Committee:

Preston T. Snee, Chair and Advisor, Department of Chemistry, UIC
Michael Trenary, Department of Chemistry, UIC
Jordi Cabana-Jimenez, Department of Chemistry, UIC
Neal Mankad, Department of Chemistry, UIC
Xiaoyi Zhang, Advanced Photon Source, Argonne National Laboratory

*"No Bird Soars Too High If HE Soars With His Own Wings"*

*To My Parents:*

*Nadereh Abu Romi & Talee Hassan,*

*This One Is For You!*

## ACKNOWLEDGMENTS

My PhD journey at UIC has been led and guided by many individuals along the way who I now have the pleasure and honor of thanking.

First and foremost, I owe my deepest gratitude to Prof. Preston Snee for giving me the opportunity to work in his group. I'm extremely fortunate to have worked with him and have grown and learned science under his guidance. I am constantly impressed with his understanding of chemistry and science in general, his enthusiasm for research is infectious and the time I spent with him in meetings always left me refreshed and inspired to work harder. It was through our conversations that I have honed my ability to communicate concisely, to become comfortable with silent reflection, and more importantly, to provide "big picture" context. Thank you for never settling for less than what you knew I was capable of doing and for always pushing me to do my best, until you are finally pushing me "out of the door." It has been pleasure working for you.

All the Snee group that I met, former and current students! I'm sincerely thankful for having a wonderful time with so many great individuals, and I appreciate every discussion, inspiration and conversation I had with all my lab members. I would like to thank some of them individually; Christina, thank you for your guidance during my early years of research; Adita, thank you for always being a great consultant when it comes to organic synthesis; and Armen, thank you for all the intellectual conversations and technical help.

Part of the work presented here was carried out at the Advanced Photon Source at Argonne National Lab (ANL-APS) where I had a great opportunity to work closely with so many amazing minds. Dr. Xiaoyi Zhang, I am particularly glad to have worked with you, and appreciate your help and assistance with analyzing X-ray data. I would like to thank the rest of my committee members, Prof. Michael Trenary, Prof. Jordi Cabana, and Prof. Neal Mankad for taking the time to read and comment on my thesis. I'm also grateful to the countless support staff within the chemistry department at UIC that truly keeps the motor running smoothly. Thank you all for your patience and help.

I have mentioned many people that helped me throughout my graduate school career, but I must express my very profound gratitude to those who helped me get there. My parents, thank you for providing me with unfailing support, love, laughs and continuous patience throughout my years of study. You have always encouraged me to be ambitious, curious, and hardworking, and this has been key to all accomplishments I might have had. To my sister, Anwar, the past few years have been quite difficult, thank you for keeping me sane and thank you for all your spot-on advice in all areas of life, because no one else seems to understand my way of thinking quite like you do.

## Contribution of Authors

**Chapter 1** was written exclusively for this thesis and provides a brief introduction to semiconductor nanocrystals including the quantum confinement effect, general synthetic strategies, traditional characterization techniques, and finally a review of the multimodal applications of semiconductor NCs. The results in **Chapter 2** were published in ACS Nano ("Charge Carriers Modulate the Bonding of Semiconductor Nanoparticle Dopants As Revealed by Time-Resolved X-ray Spectroscopy", A. Hassan, X. Zhang, X. Liu, et al., ACS Nano, 2017, 11 (10), 10070–1007) where I was the principle author and major contributor of this project. X.Z. assisted with TR-XAS experiments and data analysis, EXAFS modeling and interpretation; X.L. and A.J. contributed to synthetic method development; A.G., A.S., and R.F.K. collected TEM data; C.E.R. and R.D.S. collected and analyzed time-resolved photoluminescence data; S.C. assisted with ground state X-ray data collection; X.Z. measured SAXS data on doped NCs; and P.T.S. conceived the experiments, assisted with TR-XAS data collection and data analysis, performed theoretical modeling, and assisted with manuscript preparation. The results in **Chapter 3** have been submitted to JPCC ("Electronic Structure and Dynamics of Copper Doped Indium Phosphide Nanocrystals Studies with Time-resolved X-ray Absorption Spectroscopy and Large-Scale DFT Calculations", A. Hassan, X. Zhang, C. Liu. P. T. Snee, Journal of Physical Chemistry C.) where I was the principle author and major contributor of this project. X.Z. and C.L assisted with TR-XAS experiments and data analysis; and P.T.S. conceived the experiments, performed theoretical modeling, and assisted with manuscript preparation. The results in **Chapter 4** were published in JPCC ("Anomalous Perturbation of $O_2$ Sensitivity of Poly (aromatic) Hydrocarbon by Magnetic

Quantum Dots”**,** A. Hassan, A. Shamirian, X. Zhang, and P.T Snee, Journal of Physical Chemistry C, 2017, 121(7), 4060-4065), where I was the principle author and major contributor of this project. A.S. assisted with collecting some data and provided helpful discussion; X.Z. assisted with protocol development; and P.T.S supervised the experiments, preformed MD simulation and assisted with manuscript preparation.

## TABLE OF CONTENTS

**TABLE OF CONTENTS (Continued)**

**TABLE OF CONTENTS (Continued)**

## LIST OF FIGURES

## LIST OF FIGURES (Continued)

**Figures**.....**Page**

## LIST OF FIGURES (Continued)

## LIST OF SCHEMES

## LIST OF TABLES

# List of Abbreviations

| | |
|---|---|
| AAS | Atomic Absorption Spectroscopy |
| DFT | Density Functional Theory |
| DMF | Dimethylformamide |
| EDC | 1-Ethyl-3-(3-dimethylaminopropyl)carbodiimide |
| EMC | 1-Ethyl-3-(2- methoxyethyl)carbodiimide |
| EPR | Electron Paramagnetic Resonance |
| EXAFS | Extended X-ray Absorption Fine Structure |
| FWHM | Full Width Half Maximum |
| LED | Light Emitting Diode |
| L-J | Lennard-Jones |
| MD | Molecular Dynamics |
| MPEG CD | Methoxypolyethylene Glycol Carbodiimide |
| NBO | Natural Bond Order |
| NC | Nanocrystal |
| NTO | Natural Transition Orbital |
| NMR | Nuclear Magnetic Resonance |
| ODE | 1–Octadecene |
| PAH | Polycyclic Aromatic Hydrocarbon |
| PL | Photoluminescence |
| PMT | Photomultiplier Tube |
| QD | Quantum Dot |
| QY | Quantum Yield |
| Sulfo-SMCC | Sulfosuccinimidyl-4-(*N*-maleimidomethyl)cyclohexane-1-carboxylate |
| SAXS | Small Angle X-ray Scattering |
| STEM-EELS | Scanning Transmission Electron Microscopy-Electron Energy Loss Spectroscopy |

| | |
|---|---|
| TD-DFT | Time Dependent Density Functional Theory |
| TEM | Transmission Electron Microscopy |
| THF | Tetrahydrofuran |
| TOP | Trioctylphosphine |
| TOPO | Trioctylphosphine Oxide |
| TR-XAS | Time Resolved X-ray Absorption Spectroscopy |
| XAS | X-ray Absorption Spectroscopy |
| XANES | X-ray Absorption Near Edge Structure |
| XPS | X-Ray Photoelectron Spectroscopy |
| XRD | X-Ray Diffraction |

## SUMMARY

Semiconductor nanocrystals are emerging as a new class of novel materials with size-dependent properties that can be further tuned by the controlled incorporation of guest ions (dopants) into their lattice. Therefore, the majority of the research in this thesis was directed toward the study of the electronic structure of doped nanomaterials. **Chapter 1** consists of an introduction to the field of nanomaterials with a focus on the important aspects and terminologies. In addition, it highlights the rapid development of nanomaterial synthetic methodologies that have enabled the use of these materials for applications in diverse fields.

**In Chapter 2,** I present a detailed study of the electronic and structural dynamics of semiconductor dopants. This was enabled by using the cluster seed method for synthesizing exactly doped $Cu_4$:CdS nanocrystals. The results were obtained using time-resolved X-ray absorption studies along with DFT calculations and demonstrated that dopant bonding to the host matrix is modulated by its interaction with charge carriers. Furthermore, the transient photoluminescence and the kinetics of dopant oxidation reveal the presence of two types of surface-bound ions that create midgap states. **Chapter 3** continues to describe our further studies to the chemistry of doped materials where I present the successful controlled doping of III-V semiconductor materials (InP) and subsequent characterization using time resolved X-ray absorption spectroscopy at Argonne National Lab and Density Functional Theory (DFT) calculations to clarify the fundamental optical and electronic properties of copper guest ion as a function of the host matrix.

**In Chapter 4**, the potential applications of doped semiconductor nanocrystals are explored and a comprehensive study on a newly discovered phenomenon that offers the ability to modulate the optical properties of organic chromophores using magnetically doped fluorescent nanomaterials is presented. **Chapter 5** represents a brief conclusion of this research.

# 1 Introduction

*"What would the properties of materials be if we could really arrange the atoms the way we want them? They would be very interesting to investigate. I can't see exactly what would happen, but I can hardly doubt that when we have some control of the arrangement of things on a small scale we will get an enormously greater range of possible properties that substances can have, and of different things that we can do."*

Richard Feynman

## 1.1 Introduction

The evolution of science and technology is in great part determined by the development of new materials with the physical and chemical characteristics to meet specific needs. For example, we demark the different stages of human development by the materials that shape people's lives at those times; from sticks and swords in the Stone and Iron Ages, to wireless communications and clean energy in the Nano and Information Age. The development of the Information Age was initiated by technological breakthroughs in the field of semiconductor materials. Presently, the world is witnessing the advancement of nanotechnology where materials can be produced by the "bottom-up" approach as predicted by Feynman in 1959,[1] in which the materials are build up atom by atom starting from an increasingly larger molecular cluster and eventually evolving into a bulk crystal.

## 1.2 Semiconductor Nanocrystals: Quantum Dots

Semiconductor nanocrystals (NCs), also known as colloidal quantum dots (QDs), are a new generation of materials with typical dimensions in the range of 1-10 nm. They occupy a size regime that bridges the gap between the scientific disciplines of chemistry at the molecular level and physics in bulk materials.[2-4] An important parameter for semiconductor materials is the width of the band gap that separates the conduction band from the valence band.[5] In bulk materials, the width of the band gap is fixed, and is determined by the material's electronic structure. However, the situation changes at the nanoscale level, where the semiconductor nanocrystals electronic structure is size dependent as dictated by quantum confinement.[6] As shown in Figure 1.1, the band gap increases and quantized discrete energy levels are formed as the particle size decreases from the Bohr exciton radius to the crystal unit cell.[3,6] The quantum confinement effect was described by L. Brus and follows the particle-in-a-box paradigm according to the equation below,[6] which predicts an increase in the band gap as the dimensions of the particle are reduced.

$$E = \frac{\hbar^2\pi^2}{2R^2}\left[\frac{1}{m_e} + \frac{1}{m_h}\right]$$

Here E is the energy gap, $\hbar$ is Planck's constant, R is the particle radius, and $m_e$ and $m_h$ are the effective masses of the electron and hole, respectively.

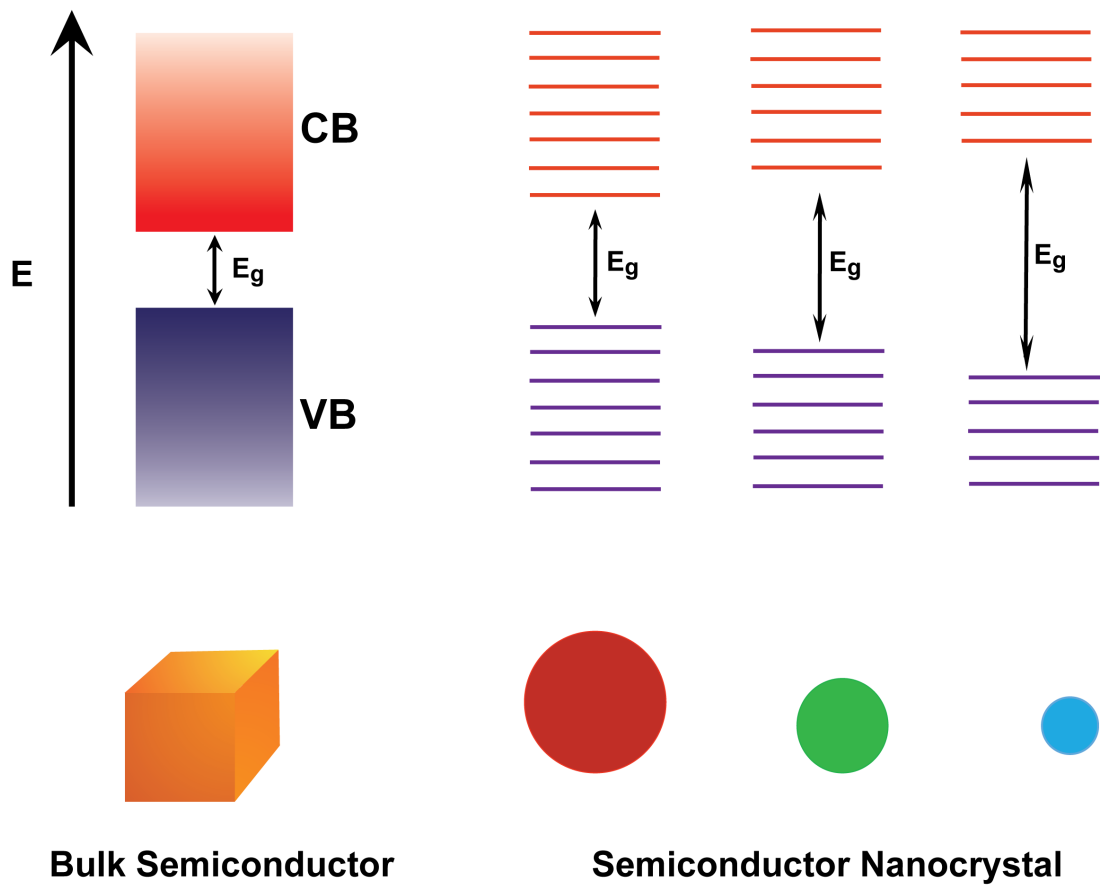


**Figure 1.1:** Electronic structure of a bulk semiconductor and quantum dots. (CB: conduction band, VB: valance band, $E_g$: band gap.)

The validity of the Brus equation can be probed by optical measurements. In moderate to wide bandgap semiconductors NCs, electrons generally only occupy the valence band, and when a photon of light is absorbed, an electron is prompted from the valence to the conduction band, leaving an equivalent positively charged "hole" behind it in the valence band. The electron and hole may interact via a Coulomb potential forming an electron-hole pair known as an exciton, as shown in Figure 1.2.[7-9] The most probable

distance between the electron and hole is the so-called exciton Bohr radius,[2,7] in which it provides a very useful length scale that is correlated to the band gap so that the wider band gap materials have relatively smaller Bohr radii. Therefore, due to size-dependent electronic structure, one can continuously tune NC properties by simply changing the NC size. This ability enhances the possibility for semiconductor NCs to be used in many different applications.

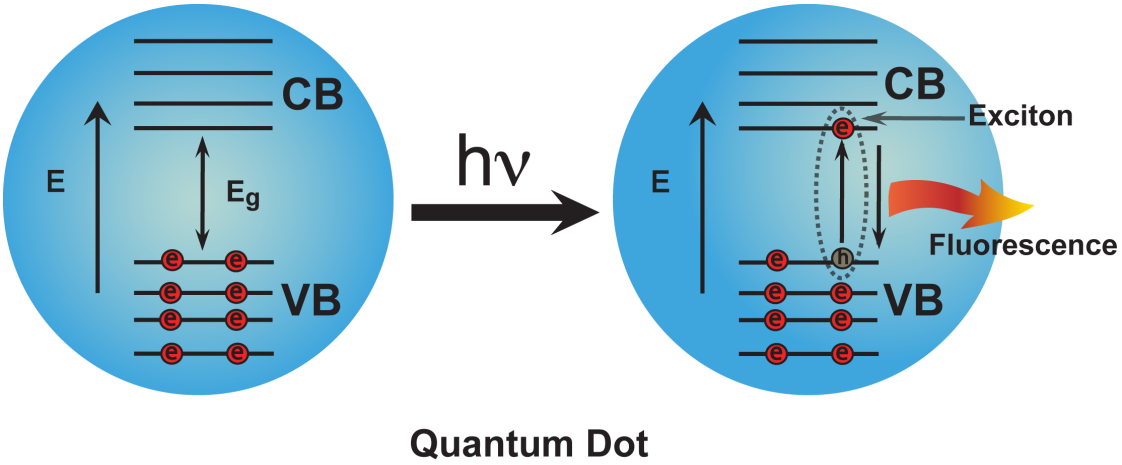


**Figure 1.2:** Creation of an electron-hole pair by excitation across the energy bandgap. (CB: conduction band, VB: valance band, $E_g$: band gap, e: electron, h: hole.)

## 1.3 Doped Semiconductors: Effects on the Band Gap

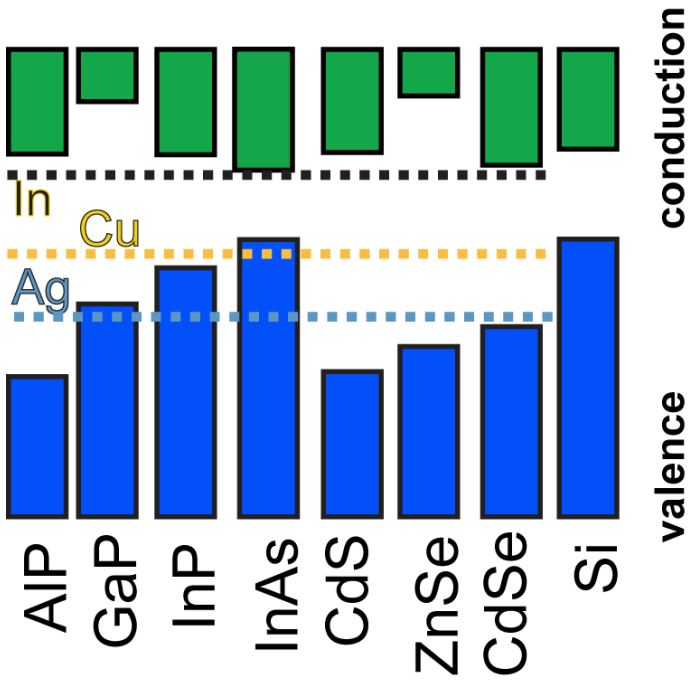


**Figure 1.3:** Relative band alignments of dopants and several semiconductor hosts.

The introduction of impurities (dopants) into the semiconductor lattice structure is a way to further tune the properties of the material. By changing the dopant type and concentration, one can achieve control of the electronic properties of semiconductor NCs beyond that offered by quantum confinement. For example, electrons can only occupy the valance band at zero temperature, and can move to the conduction band if an external energy higher than the band gap energy is supplied.[10,11] However, doping a semiconductor may introduce electronic states within the band gap.[12,13] The impurities can act as either donors or acceptors. Donor impurities have filled (occupied) states near the conduction band, while acceptor impurities have unoccupied states near the valence band, [14,15] as shown in Figure 1.3. Semiconductors doped with donor impurities are

called n-type, while those doped with acceptor impurities are known as p-type. By incorporating n- or p-type impurities into a semiconductor, the electron or hole density will increase with increasing the impurity concentrations.[16,17] Overall, doping provides possibilities of gaining further control of nanocrystal properties, which enables widespread of technological applications; as discussed further in section 1.4.2

## 1.4 Synthetic Routes

High quality materials are necessary to undertake accurate studies of nanocrystals. The NCs must be crystalline, monodisperse in size and shape, and well-passivated to ensure well-defined electronic states free of surface defects.[18] Therefore, in order for the nanocrystals electronic and optical properties to be studied and utilized, the development of reliable and reproducible synthetic methods is essential. The most common synthetic protocol for the preparation of nanocrystals is comprised of two main steps: the nucleation step followed by the growth step. Nucleation involves the formation of nanocrystal nuclei, often at high temperature, while growth involves the addition of reagents to achieve the target size. The first reported synthetic route is the arrested precipitation method, where the reaction is initiated by the mixing of metal and chalcogenide precursors in a polar solvent.[19-22] The initial NC size was determined by mixing kinetics, precursor concentrations, and temperature. The growth of NCs was achieved by varying the solution temperature. The average final size of the NCs depended on the initial size, growth time, and growth temperature. To prevent NCs from agglomerating, a polymer stabilizing agent was added to the initial reaction mixture.

These species bound to the NC surfaces and prevented fusion between the particles. However, significant drawbacks of this method included the large size dispersities of the particles, poor crystallinity, and low product yield. These problems were largely surmounted by development of a lyothermal synthetic method as first reported by Murray and coworkers,[18] in which dimethylcadmium ($CdMe_2$) and trioctylphosphine selenide (TOPSe) are quickly injected into a trioctylphosphine oxide (TOPO) solvent at high temperature (>280 °C). The rapid injection caused the nucleation and the growth steps to be effectively separated as, upon injection, the reaction temperature decreases below the nucleation threshold where the nanocrystals could grow. Although further modifications that increased the monodispersity were reported by Peng and Alivisatos,[23,24] a significant drawback of these reported lyothermal protocols was the necessity to use highly reactive and air sensitive precursors that were difficult to store and handle, and the reliance on the fortuitous presence of surfactants that were present in the low purity solvents employed.

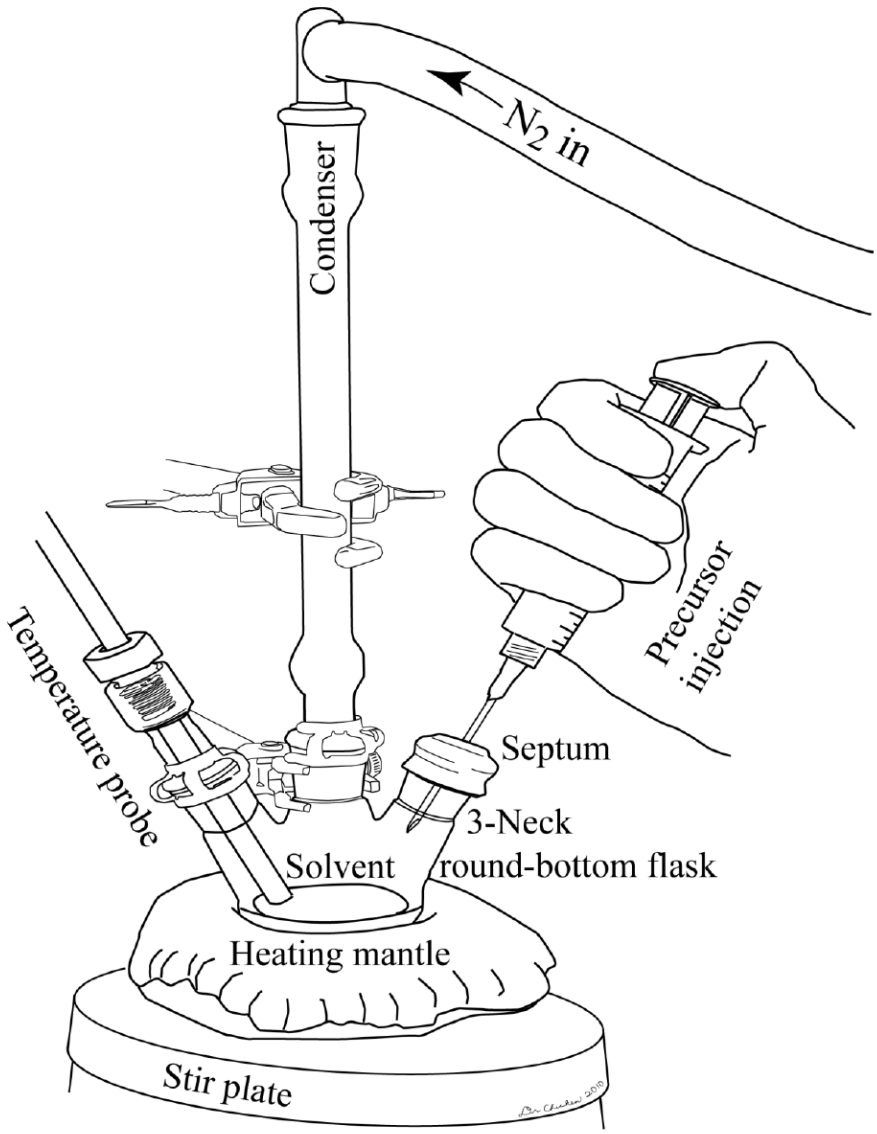


**Figure 1.4:** The rapid injection method for the synthesis of semiconductor NCs. The solvent and metal precursors are heated under a constant stir and the chalcogen precursor is rapidly injected into the reaction vessel, which induces the nucleation and growth events.

An alternative protocol for the synthesis of semiconductor nanomaterials is the single source precursor method. The materials are prepared using reagents that are stable under ambient conditions, have the metal-chalcogenide bonds already existing in the molecular precursor, and allow the nucleation to start at relatively lower temperatures.[25-27] This synthetic method allows for controlled growth of high quality nanomaterials using safe, less reactive, and inexpensive starting materials. The technique is based on the introduction of an inorganic metal-chalcogenide cluster into an alkylamine solvent, where the core of the clusters forms a nucleation site and cluster degradation in the coordinating solvent provides the source of active species for subsequent growth.[27] The precursors can be injected into a hot solvent or added at room temperature and then heated to the growth temperature. One of the concerns for this method is the limited availability of suitable precursors for different material systems that might restrict its further development. Moreover, the heat up method sometimes results in polydisperse samples.

Although there has been great progress in the development of synthetic methodologies for nanocrystals, there is a movement toward fully understanding the mechanism of particle nucleation and growth to clarify the key controllable parameters such as the reaction temperature, time and the surface energy. In general, these studies have been performed with UV−vis spectroscopy. Other techniques can be used to further study the formation processes such as the use of nuclear magnetic resonance (NMR) spectroscopy, X-ray absorption spectroscopy (XAS), as well as quantum chemical modeling (DFT). Generally, the development of a microscopic description of the NC formation mechanism will open the possibility to predict how a particle will form within

solution, hence obtain control of the synthesis much faster compared to the current methods.

### 1.4.1 Synthesis of Core/Shell Nanocrystals.

Impressive advances have been made in the synthesis of nanocrystals, and significant attention is now turning toward improving their properties *via* robust preparation protocols. Generally, there is a significant population of atoms on the surface of NCs resulting in a high surface to volume ratio. These surface defects act as "traps" for charge carriers (electrons or holes) that have significant effects on the optical properties of NCs.[28-30] Therefore, capping or passivation of the surface is essential for robust quantum confinement and for improving photostability.[31] This is done by growing epitaxial layer(s) of an inorganic material, particularly one that is lattice-matched and has a larger band-gap, over the core material to obtain core/shell quantum dots.[31,32] Generally, this results in a substantial improvement of optical and electronic properties of NCs. [31-33]

### 1.4.2 Synthesis of Doped Nanocrystals.

Extensive research efforts have been devoted to the incorporation of impurities into the semiconductor lattices to modulate the physical and chemical properties of these materials. [34-38] In modern technology, it is well known that doped semiconductor silicon is the most important material, in which atoms from the neighboring groups in the periodic table replace silicon in the lattice structure. This can result in either n- or p-type doping. These types of doping have built the foundation for p-n junction semiconductor microelectronic devices such as diodes and transistors that are used to create

semiconductor based memories. The range of properties achieved by doping bulk materials encouraged researchers to explore the same semiconductor nanocrystals due to the possibilities of gaining further control over their optical, electronic, and magnetic properties. [39,40] However, the incorporation of dopants into semiconductor nanocrystals is not always straightforward and several challenges come with their preparation. The main problem is the tendency of the nanocrsytals to exclude the dopant ions from its lattice at the high temperatures that are used to grow nanocrystals. In addition, the variation of dopant concentration in NCs due to Poissonian distribution results in major differences in the individual properties of dots produced within a single batch.[41,42] Finally, evaluating the successful doping of nanocrystals was also found to be problematic. For example, X-ray diffraction studies of doped crystals yield predominantly the characteristic diffraction features of the host and provide little reliable indication of the success or failure of doping. Elemental analysis and X-ray photoelectron spectroscopy cannot distinguish between surface-bound and interior dopants. Therefore to solve these problems, it is important to dope semiconductors uniformly, *i.e.* same number of guest ions per nanocrystal, [43-45] as well as turning to other analytical and spectroscopic techniques that are sensitive to the identity of the dopants themselves; this will be discussed in Chapters 2 and 3.

## 1.5 Functionalization and Water Solublization

Although semiconductor nanocrystals can be synthesized in water, they have more robust properties such as higher quantum yield and narrower size distribution when prepared in a hydrophobic solvent.[18] However, this results in making them only soluble in nonpolar organic solvents that are not biocompatible; thus, it is important to process the hydrophobic NCs to create aqueous dispersions.[47,48] Two methods have been developed that are widely employed to impart hydrophilic surfaces to NCs; cap exchange and polymer encapsulation, a representation is provided in Scheme 1.1. Cap exchange is accomplished by replacing the native hydrophobic ligands on the surface of the NCs with hydrophilic molecules that have NC surface binding functionalities such as thiol groups.[47,49-51] Although this approach of water solubilization is effective, the luminescence quantum yield tends to suffer and the materials are unstable.[52] In the encapsulation method, the nonpolar native ligands act as intermediate binding sites between the NCs and the amphiphilic polymers. The hydrophobic portion of the amphiphiles intercalates the native hydrophobic ligands while the hydrophilic section affords water solubility.[53-55] The use of amphiphilic polymers creates water soluble NCs with higher quantum yields, but larger hydrodynamic diameters,[56] which is less desirable for biomedical applications.

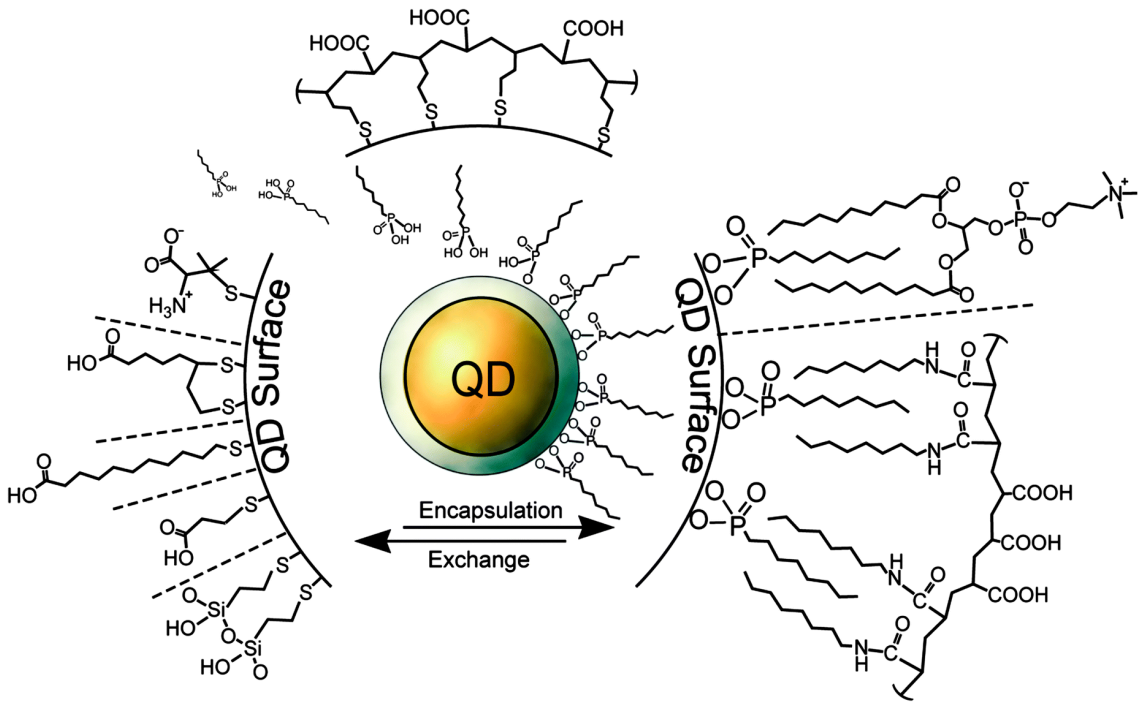


**Scheme 1.1**: Cap-exchange and encapsulation methods for water-solubilzation of QDs. Reprinted with permission from Ref. 57, Copyright 2014 The Royal Society of Chemistry.

To enable the use of NCs in a wider range of applications, they must be functionalized with chemical or biological components. While many physical interactions, such as, electrostatic [7,49,58] and nonspecific adsorption [59,60] interactions, can be exploited for attaching biomolecules to the surface of NCs, the formation of stable colloidal systems without aggregation was questionable using these approaches. Thus, the development of more robust conjugation methods for attaching biomolecules stably on the NC surface is important. A suitable ligand on the surface of water solubilized NCs should allow attachment of a variety of biological vectors such as proteins, nucleic acids, and peptides using a covalent cross-linking strategy. In the case of having carboxyl functional groups on the surface of a NC, carbodiimide coupling reagents such as, 1-

ethyl-3-(3-dimethylaminopropyl) carbodiimide hydrochloride (EDC),[49,61-63] methyl-polyethylene glycol carbodiimide (MPEG CD)[64] and 1-ethyl-3-(2-methoxyethyl) carbodiimide (EMC) could be used to link the NC with amine-functional substrates. In the case of thiol-funcional NC surfaces, the reagent sulfosuccinimidyl-4-(N-maleimidomethyl) cyclohexane-1-carboxylate (sulfo-SMCC)[64] is used. Great progress has been made in the field of functionalizing NCs, and at the present, research is moving toward the development of reagentless and bio-orthogonal coupling protocols[65-68] that can allow for the realization of the vast potential of NCs in biological applications.

## 1.6 Characterization

The rapid development of semiconductor nanocrystals for a diverse array of applications in nanotechnology requires rigorous but practical analytical and physical tools to characterize the optical and structural properties of these materials. Although many techniques are available, knowledge of the appropriate analytical method to use on a given system requires a fundamental understanding of both the strengths and limitation of the tool being used as well as chemical intuition. It is therefore, the aim of the next section to briefly provide an overview of the analytical techniques that are used to study the physicochemical properties of nanomaterials.

### 1.6.1 Optical (Absorption/Photoluminescence) Spectroscopic Characterization

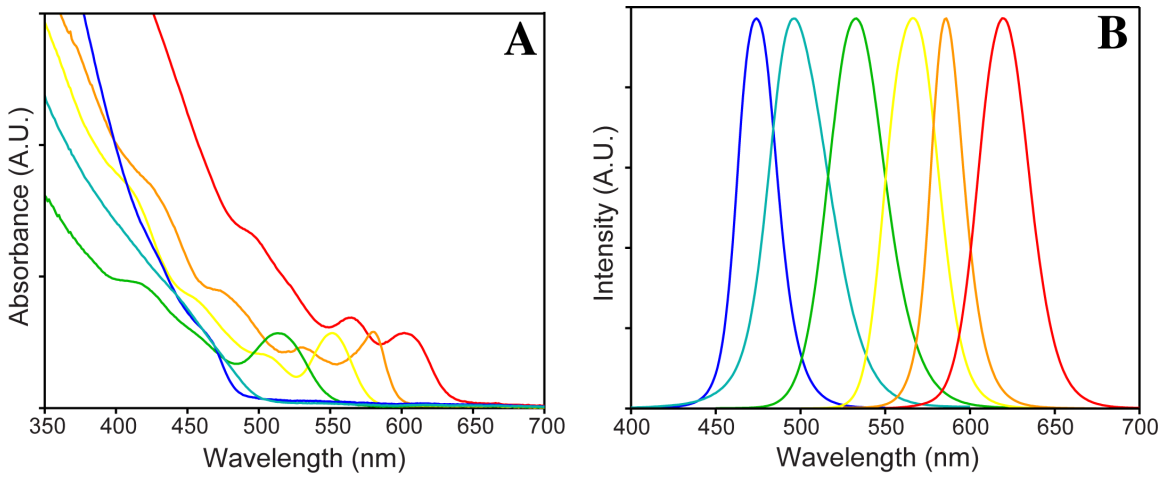


**Figure 1.5**: (A) Absorption and (B) Emission spectra of QDs with different sizes. Note that the spectra shift to high energy with decreasing size.

The unique properties of semiconductor nanocrystals arise almost entirely due to their size. Thus, determining the NC size is an important parameter for the characterization of the material. Optical absorption spectroscopy is one of the simplest techniques used to determine the size of NCs[69,70] as the band edge absorption is correlated to the NC size due to quantum confinement.[71] As shown in Figure 1.5A, the first exciton transition of a sample, has a relatively sharp absorption feature, the position of which depends on the band gap, which in turn depends on the size of the particles. Note that the absorption peak blue shifts as the particle size gets smaller.[70,72,73] Moreover, the particle size distribution can be estimated from both absorption and emission spectra by calculating the full width half maximum (FWHM) of the their features.[71] Monodisperse samples exhibit a sharp and narrow first absorption feature with small FWHM. Similarly, a symmetrical emission peak with a narrow FWHM indicates the high

quality of the NCs since only samples with proper surface passivation and good size distributions emit narrow and symmetrical spectral shapes.[74,75]

### 1.6.2 X-ray Absorption Spectroscopic Characterization

Atomic scale chemical and structural information of semiconductor nanocrystals can be obtained using X-ray absorption spectroscopy (XAS). Most XAS experiments are performed at a synchrotron source due to the requirement of high X-ray intensities and continuous energy resolution.[76] Great advances to synchrotron radiation sources have been made to not only enable static XAS measurements, but to facilitate detailed studies on the time scales, which allowed for the development of new applications such as time-resolved (TR) measurements of dynamic processes and structural analysis of nanomaterials.[77-79]

X-rays are ionizing radiation as they have enough energy to eject a core electron from an atom.[80] Each core level has a distinct binding energy, and as the X-ray frequency is scanned through, there is a sharp increase in the absorption at specific X-ray points corresponding to the binding energy of the core states.[81] This abrupt increase is called the absorption edge, and different core-electron binding energies are named according to the principle quantum number of the electron that is excited (K, L, M, etc.).[82] Therefore, XAS measures the energy-dependent fine structure of the X-ray absorption near the absorption edge of a particular element.[83] The X-ray absorption spectrum is commonly divided into two spectral regions, X-ray absorption near-edge spectroscopy (XANES) and extended X-ray absorption fine-structure spectroscopy (EXAFS). XANES is strongly sensitive to the valence state and chemical bonding of the absorbing element. Thus, it

provides information about the oxidation state and often the coordination structure (e.g., octahedral, tetrahedral, etc.).[84] On the other hand, the EXAFS spectral region is sensitive to the radial distribution of electron density around the absorbing atom. As a result, EXAFS can be used to determine the identity of the neighboring atoms, their distances from the excited atom, and the coordination number.[81,85]

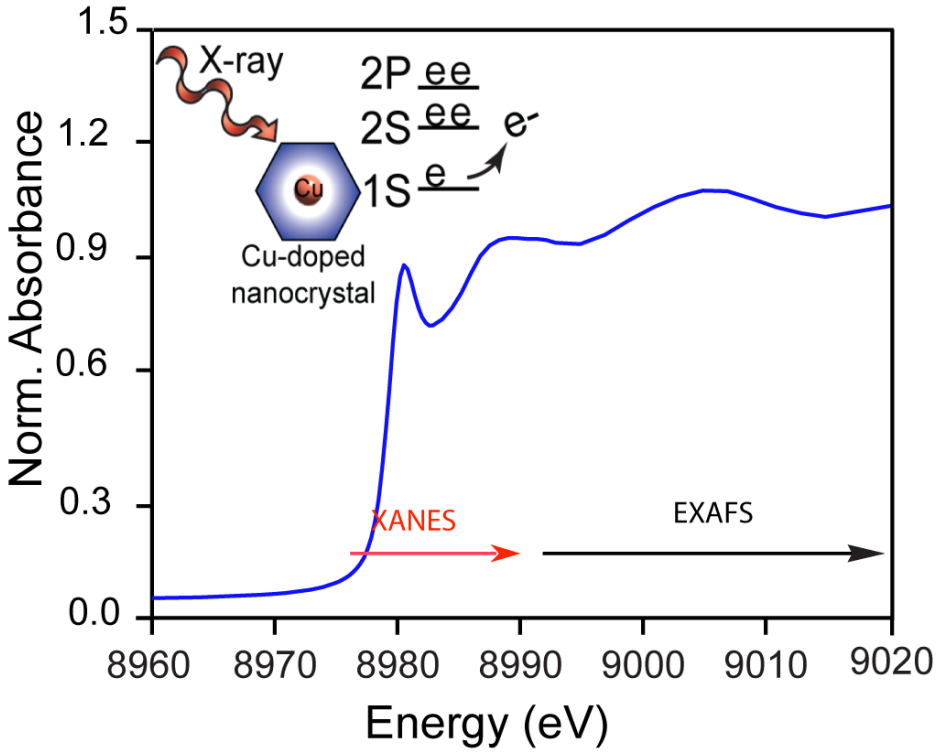


**Figure 1.6:** Cu K-edge X-ray absorption spectrum showing the near edge (XANES) and extended regions (EXAFS) regions. (Inset: Schematic illustration of the absorption process).

XAS it has permitted the study of dopants in semiconductors by providing a structural basis for the understanding of physical properties.[83,86] The local structure and

characterization of the incorporation sites of dopants in the different host matrices can be obtained by tuning the X-ray energy at the corresponding absorption edge of a particular atom or dopant. However, the main limitation of XAS to study dopants is that it only measures the average structure of all atoms of the photoexcited element.[87] Therefore, if the element of interest is present in different local atomic environments at different incorporation sites in the host matrix, extracting information about their contribution can be difficult. Nonetheless, the use of theoretical calculations and structural simulations such as density functional theory (DFT) in data analysis has allowed great advances in tackling this problem.[44,87-89]

## 1.7 Applications

Over the past two decades, semiconductor nanocrystals have been investigated due to their novel optical and electronic properties, which make them ideal candidates for a wide range of potential applications. The bright and size-dependent fluorescence emission of NCs can be used in lasers, displays, and light emitting diodes.[90-92] Similarly, their tunable absorption with high extinction coefficients makes them attractive for ultra sensitive photodetectors and photovoltaic applications.[93] Semiconductor NCs can also be used as the basis of new types of solar cells as the bandgap of the material can be tuned over a broad range of the solar cell's spectrum.[94-96] Finally, the most rapidly developing and exciting application of semiconductor NCs is their usage in biomedical research such as labeling, imaging, and sensing due to their high quantum yield (QY) and high resistance to photobleaching.[97-99] This wide range of potential applications has been the

driving force to push the size of nanomaterials to its smallest critical dimension. An example is semiconductor chip-technology where maintaining the pace of Moore's law is currently dictating industry to come up with new ideas and technologies to get around the barrier.[100]

# 2 Charge Carriers Modulate the Bonding of Semiconductor Nanoparticle Dopants as Revealed by Time-Resolved X-ray Spectroscopy

The content of this chapter has been published as " Charge Carriers Modulate the Bonding of Semiconductor Nanoparticle Dopants as Revealed by Time-Resolved X-ray Spectroscopy", A. Hassan, X. Zhang, X. Liu, C. Rowland, A. Jawaid, S. Chattopadhyay, A. Gulec, A. Shamirian, X. Zuo, R. Klie, R. Schaller, Preston T. Snee*, *ACS NANO,* **2017**, 11(10), 10070-10076. Reproduced with permission from the American Chemical Society.

## 2.1 Introduction.

Intrinsic semiconductors must be modified to create diodes and transistors that are the basis of modern electronics.[101] This is accomplished by the incorporation of dopants into the matrix to add (subtract) electrons to the conduction (valence) bands. However, the conduction of charge carriers is impeded by scattering off dopants, which is detrimental to device performance.[102,103] To study semiconductor dopant photophysics, we have examined the transient interaction of an excess charge carrier with a guest ion in a semiconductor matrix using time-resolved X-ray absorption spectroscopy (TR-XAS).[77,104-106] Several synthetic and experimental developments were realized to successfully perform such studies. For example, TR-XAS requires a large quantity of the substrate to flow through a liquid jet to avoid the buildup of oxidized byproducts.[77] To this end, we have developed a method for producing large batches of Cu-doped colloidal CdS semiconductor nanocrystals, where each NC contains the exact same number of guest ions. This procedure is based on the cluster seed method, where nanocrystals are nucleated around a small organometallic cluster in a process that can be easily increased in scale.[43,107,108] Doped NCs are created by the use of a seed that contains the guest ion(s).

Furthermore, the method resolves the problems associated with dopant loading level Poissonian inhomogeneity.[42,109]

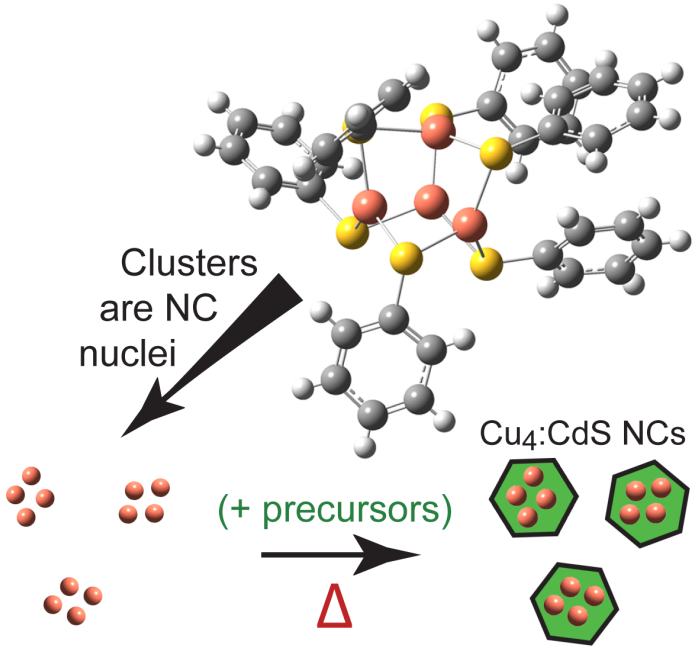


**Scheme 2.1.** The cluster seed method for synthesizing CdS NCs with four copper dopants (Color code: orange, copper; yellow, sulfur; grey, carbon; white, hydrogen).

The results discussed below provide an unambiguous demonstration of hole capture by the dopant due to the fact that photoexcitation of copper-doped cadmium sulfide nanoparticles resulted in a shift of the Cu K-edge X-ray absorption near-edge spectroscopy (XANES) absorption to higher energy. This in turn instigated a stronger bonding interaction of copper with sulfur within the semiconductor host as revealed by the excited-state extended X-ray absorption fine structure (EXAFS) spectrum. X-ray analyses also revealed two types of surface bound copper ions that display different

dynamics in the excited state. These data were augmented with large-scale density functional theory (DFT) calculations on ground and excited states of quantum dots.[110] Furthermore, the DFT results attest to the generality of the conclusions made with copper doped CdS dots. Overall, the modulation of dopant bonding by electrons and holes has implications for understanding the dynamics of charge carriers in semiconductor hosts.

## 2.2 Experimental.

### 2.2.1 Materials.

1-Octadecene (90%), oleylamine (90%), benzenethiol (97%), anhydrous methanol (99.8%), trimethylamine (97%), tetramethylammonium chloride (97%), cadmium acetate (99.999%), and thiourea (99%) were purchased from Sigma-Aldrich. Anhydrous dimethylformamide (DMF, 99.8%) and copper (II) nitrate trihydrate (99%) were purchased from Acros. 1-Butanol (95%) was purchased from Strem. Oleylamine was purified by recrystallization at -30 $^{o}$C from acetonitrile and was stored at 4 $^{o}$C. All other reagents were used without further purification.

### 2.2.2 Synthesis of $[N(Me_4)]_2[Cu_4(SPh)_6]$ cluster.

$[N(Me_4)]_2[Cu_4(SPh)_6]$ clusters were synthesized according to previously published protocols with slight modifications.[43,111] The procedure is restated here for completeness. Into a one-neck round-bottom flask connected with a dripping funnel, 25 mL of triethylamine, 50 mL of methanol, and 10 g of benezenethiol (97 mmol) were added, and the solution was flushed with $N_2$ for 1 hr. After heating the solution to reflux, 8.0 g (33.1

mmol) $Cu(NO_3)_2 \cdot 3H_2O$ dissolved in 40 mL of methanol was added dropwise. The solution quickly turned yellow, the coloring of which remained throughout the process. Addition of the copper nitrate solution was stopped when the reaction vessel was saturated with yellow products, evaluated by the increasingly lower solubility of $Cu(NO_3)_2$. After the solution cooled to room temperature, 2.5 g (23 mmol) of tetramethylammonium chloride dissolved in methanol was added to the solution, which was layered with 2-propanol immediately. The solution was allowed to equilibrate overnight at room temperature under $N_2$. The product precipitated as yellow crystals, which were filtered, washed with cold acetone and ether, dried under vacuum, and stored in a glovebox. See reference 43 for characterization data.

### 2.2.3 Synthesis of CdS:$Cu_4$ using $[N(Me_4)]_2[Cu_4(SPh)_6]$ as seeds.

Into a 50 mL three-neck flask, 7 mL of 1-octadecene, 2 mL of purified oleylamine, and 0.23 g (1 mmol) of cadmium acetate were added and heated to 110 °C under vacuum for 1 hr. The solution turned clear and the vessel was backfilled with $N_2$ and cooled to room temperature. Next, 0.8 →2.8 mg of $[N(Me_4)]_2[Cu_4(SPh)_6]$ dissolved into a minimal amount of DMF (~0.1 mL) was added at room temperature into the degassed solvent, followed by 0.038 g (0.5 mmol) thiourea in a minimal amount of DMF (~0.5 mL) and 2 mL of 1-butanol. The solution was slowly heated to 50 °C and monitored *via* absorption for 1 hr. Finally, the solution was heated gradually to 100 °C at a rate of 5 °C / min, and was maintained at this temperature for ~16 hrs.

### 2.2.4 Characterization

Optical UV/Vis absorbance spectra were taken using a Varian Cary 300 Bio UV/Vis spectrophotometer. Temperature-dependent photoluminescence spectra and dynamics were acquired using a 35 ps pulsed laser diode operating at 450 nm and 500 kHz repetition rate. The collected emission was directed to a 300 mm focal length grating spectrograph and either detected with a CCD for spectra or an avalanche photodiode for detection of a specific wavelength. Sample temperature control was afforded via a sample in vacuum, closed-cycle helium cryostat.

X-ray diffraction (XRD) studies were performed on a D8 Advance ECO Bruker XRD diffractometer using a graphite monochromator and a proportional detector. The power generator was operated at 40 kV and 20 mA.

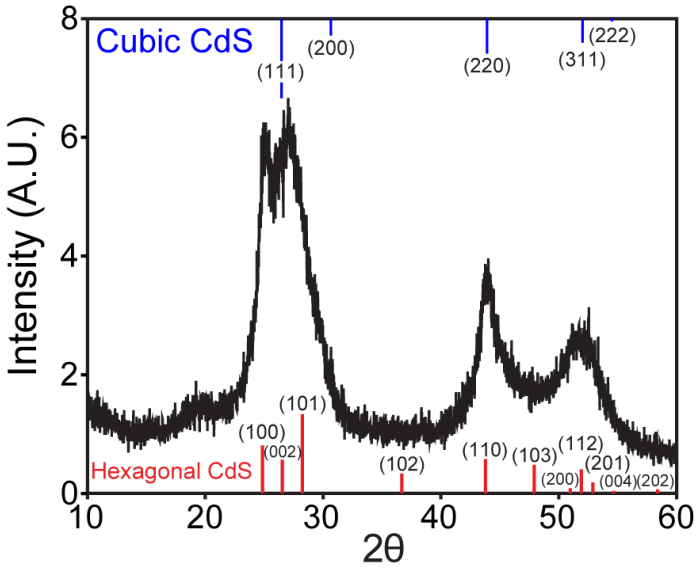


**Figure 2.1.** XRD shows a preeminent peak around bulk Wurtzite CdS (101) facet signal ($2\theta=27^{\circ}$) implying a Wurtzite dominating structure of $Cu_4$:CdS NCs

X-ray Photoelectron Spectroscopy (XPS) analyses were performed on a Kratos Axis 165 using a monochromatic Al Kα source operating at 12 kV and 10 mA to produce an X-ray power of 120 W. Spectra were collected with a photoelectron takeoff angle of 90° from the sample surface plane, in energy steps of 0.1 eV, and a pass energy of 20 eV for all elements.

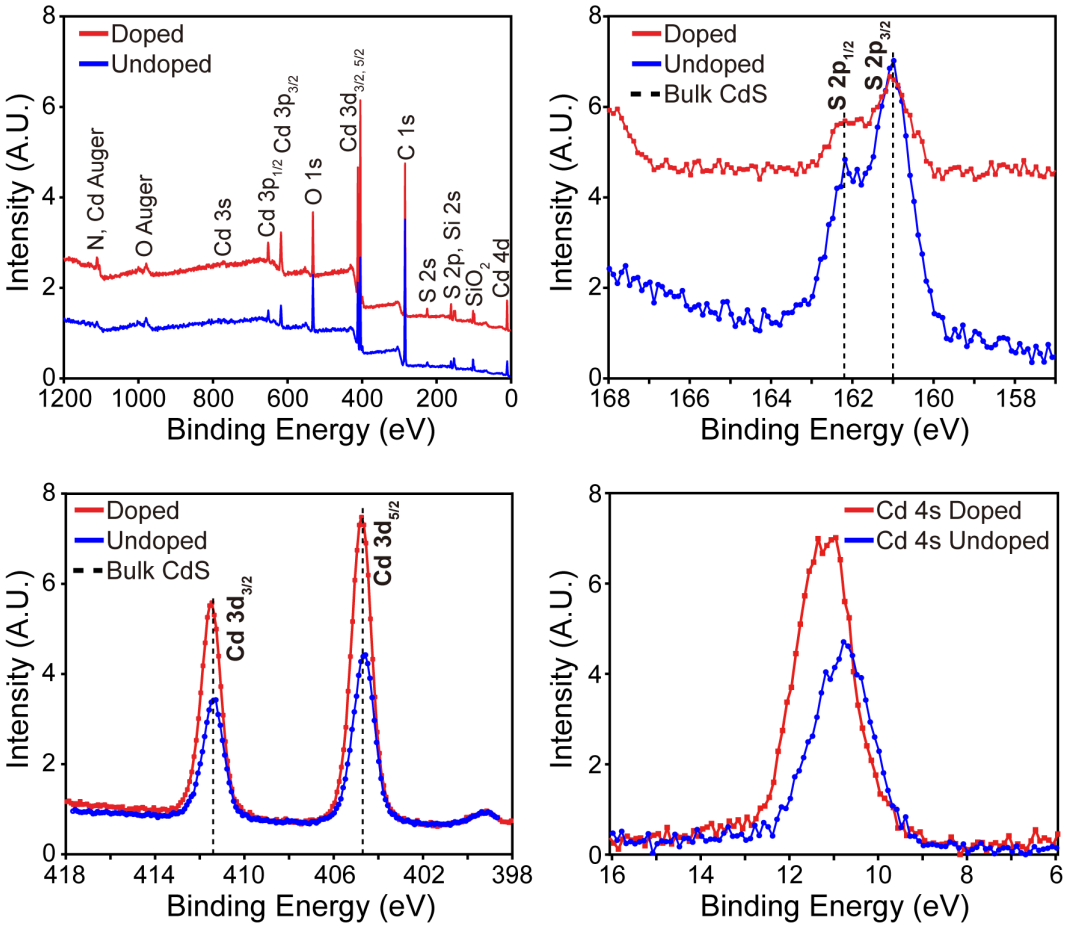


**Figure 2.2.** XPS spectra of neat and copper-doped CdS NCs. A comparison of the valence Cd-4s reveal a slight 0.1~0.2 eV blue shift, which could be explained by p-doping of the semiconductor hosts by the Cu guest ions.

Transmission Electron Microscopy (TEM) images were obtained on a JEOL JEMARM 200CF electron microscope operating at 200 kV with a cold field emission source for high spatial resolution with combination of imaging modes including high angle annular dark field (HAADF) imaging with an inner collecting angle of 68 mrad and outer collecting angle of 230 mrad, annular bright field (ABF) imaging with an inner collecting angle of 11 mrad and outer collecting angle of 22 mrad. A probe side Cs-corrector was used to yield a probe size of approximately 0.078 nm. Under daily operating conditions, the third order aberrations remain stable for days while the second order aberrations were monitored and corrected as needed during the experiments. Other images shown below were obtained using a JEOL JEM-3010 operating at 300 keV.

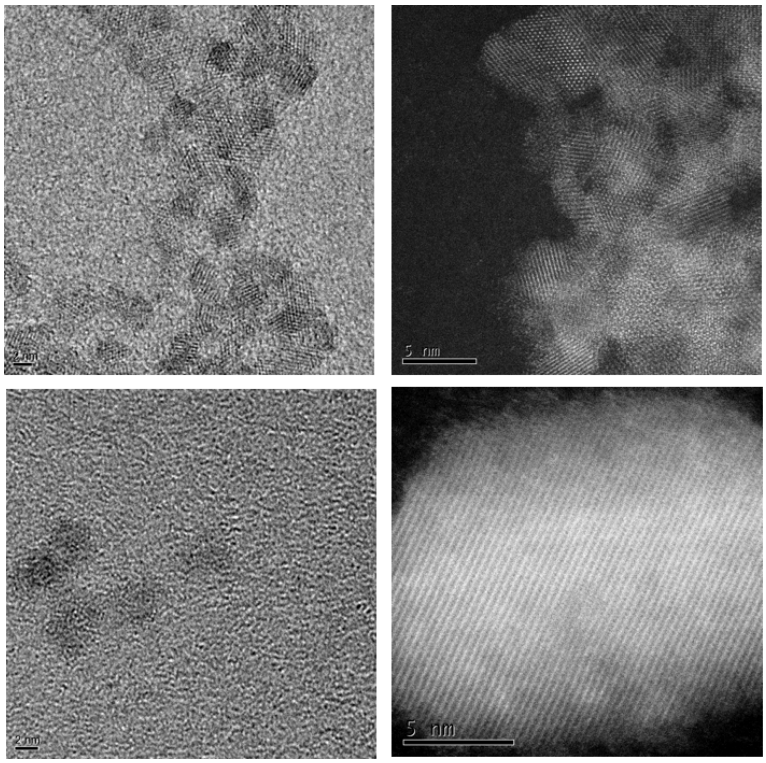


**Figure 2.3.** TEM micrographs of copper doped CdS NCs.

Magnetic susceptibility data were collected from 2 K to 300 K under magnetic fields of 1000 and 5000 G using a Quantum Design MPMS-XL SQUID magnetometer. Samples were pressed powders of the quantum dots sealed in a gel cap. Susceptibility was corrected for the diamagnetism of the sample holder and the diamagnetic response of the sample itself, estimated with a "molecular" formula of $Cd_{950}S_{950}Cu_4(C_{18}H_{37}N)_{50}$, using Pascal's constants.[112]

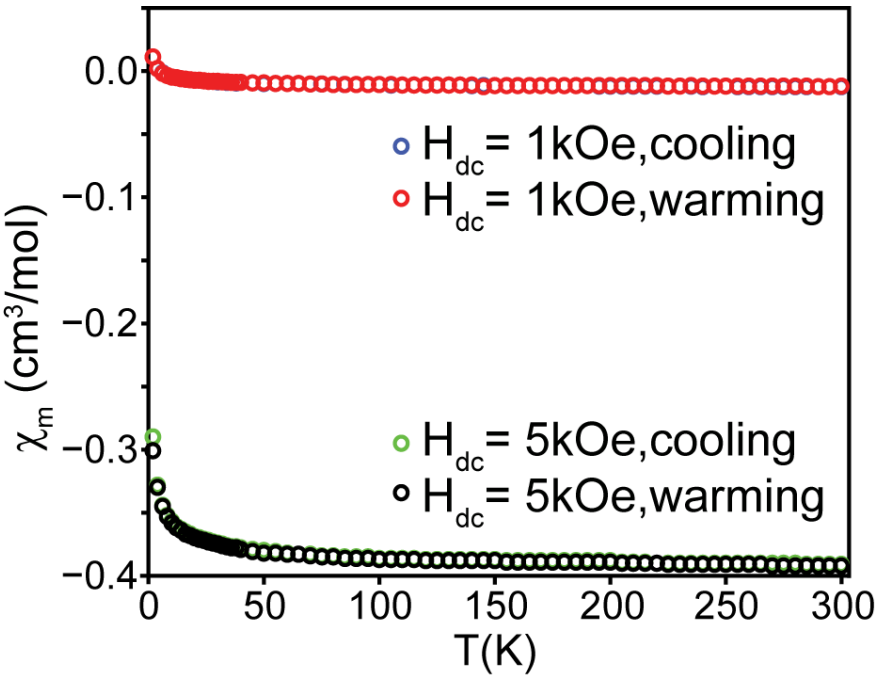


**Figure 2.4.** Variable temperature magnetic susceptibility data for the $Cu_4$:CdS NCs under 1 and 5 kOe magnetic fields.

Fourier-transform infrared spectroscopy was collected using a Bruker X FTIR. Samples of $Cu_4$:CdS NCs were processed *via* precipitation with a non-solvent to remove excess octadecene and oleylamine to characterize their surface ligands.

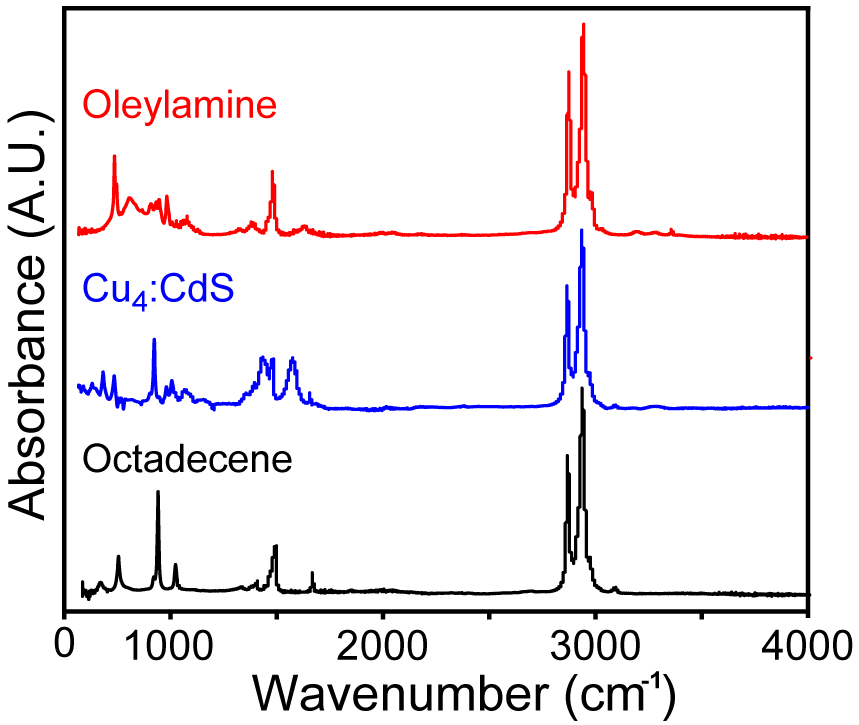


**Figure 2.5.** FTIR spectra of oleylamine, $Cu_4$:CdS NCs, and 1-octadecene reveal that the spectrum of NC surface ligands is composed of ODE and oleylamine. However, the ODE features are likely artefactual as the processing of samples to remove the organics proved highly problematic, and there is likely excess ODE present in the precipitate. As such, we are confident that the NCs are coated with oleylamine.

Small Angle X-ray Scattering (SAXS) analysis were performed at ANL-APS Beamline 12-ID-B beamline to study the size distribution of the $Cu_4$:CdS NCs suspended in 1-octadecene, with a concentration of 0.1 mmol/L, using 14 keV X-ray energy. The SAXS data were collected with a Pilatus 2M detector and the cutoff energy was set to 10 keV to eliminate possible fluorescence background. The beam size with 0.05 × 0.2 $mm^2$ and exposure time of ~1 s were used for the measurements. The data were fully corrected, reduced to intensity versus scattering vector (Q) profiles, and background subtracted with the Irena software integrated in Igor Pro.[113] These data were used to augment our estimation of NC size via absorption measurements.

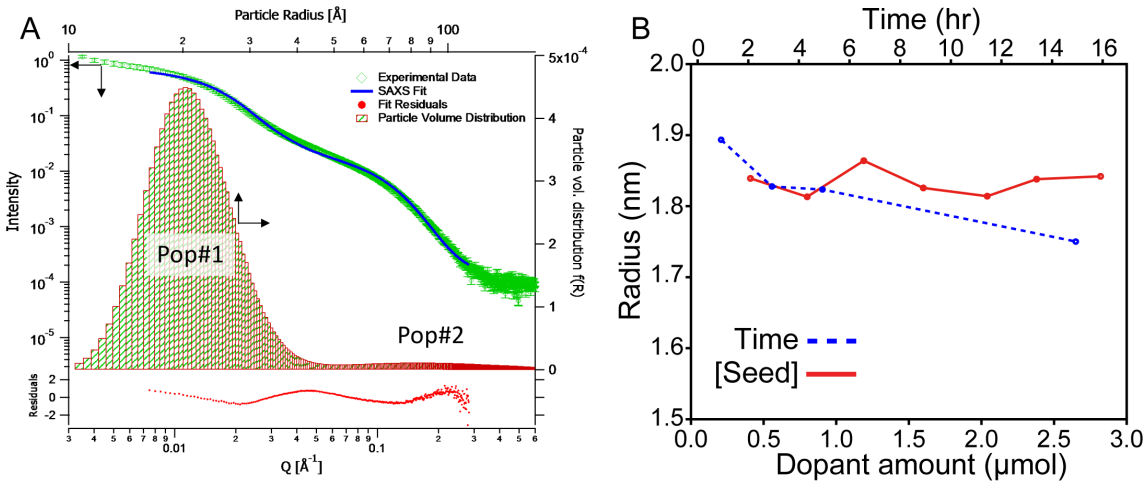


**Figure 2.6.** (A) The SAXS data (green) and fitting for particle size distribution (red bar). Two particle size populations were found, both of which are assumed to following LogNorm distribution. They are labeled as Pop#1 and Pop#2, which arise from SAXS peaks around q of ~0.06-0.3 $Å^{-1}$ and ~0.006-0.03 $Å^{-1}$, respectively. Pop#1 is the major population and the average radius is 19 ± 5 Å. Pop#2 is a minor population and the average radius is 61 ± 23 Å. (B) The NC size vs. cluster seed mass and growth time was studied which revealed that the synthetic method generate same size nanomaterials.

### 2.2.5 Elemental Analysis and Pyridine Cleaning.

To characterize the elemental composition, several ~1g portions of the growth solution containing $Cu_4$:CdS NCs were processed with precipitation several times to remove the solvent (mostly octadecene), and were digested according to EPA method 3050B.[114] Several blanks and other controls such as blanks spiked with copper and cadmium standards that reflected the estimated composition of the NCs were processed using the same protocol. Atomic absorption (AA) spectroscopy was performed using a PerkinElmer AAnalyst 200. Machine drift was tracked by bracketing every 10 measurements with calibration standards; if the standard was outside of 10% of its nominal value, the AA was recalibrated and the samples were re-analyzed.

### 2.2.6 Static X-ray Absorption.

X-ray Absorption Near-Edge and Extended X-ray Absorption Fine Structure Spectroscopy (XANES and EXAFS) measurements at the Cu K-edge (8979 eV) were carried out at the Advanced Photon Source at Argonne National Laboratory to study the local environment of Cu dopants before and after illumination with strong UV light (Norland Opticure LED 200). Static X-ray measurements were taken at beamline 10-ID-B, where Cu doped CdS samples dissolved in 1-octadecene were loaded into 0.5 mL circular safe-lock plastic Eppendorf tubes with a wall thickness of 700 μm. The absorption of the walls is minimal (0.392 at Cu K-edge); thus, it does not affect the Cu-edge absorption energy. All measurements were performed at room temperature at a 45° orientation to the beam. X-ray absorption measurements were collected in fluorescence mode using a four-element Vortex 411 solid-state fluorescence detector. The step size

across the edge was 0.25 eV, and the measurement time was set to 2 s per point. XANES scans covered ~250 eV below copper's K-edge energy (8979 eV) and up to 300 eV above the Cu edge. EXAFS scans started from ~250 eV below to 650 eV above the Cu edge. A typical scan took about 20 min with data in higher k-space taken with a step size of k = 0.05 $Å^{-1}$ and measurement time of 4 s per step. The energy resolution of the monochromator is 0.25 eV. The position of the X-ray beam was moved between each scan to minimize sample degradation. Reference samples were spread over Kapton tape and subsequently stacked together such that the thickness (x) of the samples corresponded to $\Delta\mu x = 0.5$, where $\Delta\mu$ is the edge step of the absorption coefficient at the Cu K-edge energy. $Cu_2S$ standard was measured in a transmission geometry using a quick scan mode with the monochromator measuring energy on the fly using step sizes of 0.3 eV and a measurement time of 0.1 s per step. Several scans were merged to obtain better statistics. A copper metal foil scan was simultaneously measured between the standard and NC sample using a reference ion chamber to calibrate the energy scale. These measurements used a reference detector composed of 70% He/30% $N_2$ and a transmission reference of 100% $N_2$. All measurements used an incident X-ray spot size of 500 × 500 μm.

### 2.2.7 Time-resolved X-ray Absorption.

Time-resolved Cu K-edge XANES measurements (TR-XAS) were performed in total fluorescence mode at beamline 11-ID-D of the Advanced Photon Source, Argonne National Laboratory. The laser pump pulse was the second harmonic output of a Ti:Sapphire regenerative amplified laser with 10 kHz repetition rate, giving 400 nm laser

pulses with 500 fs FWHM. The laser pulse was further stretched to 1.5 ps using a prism pair. The experiment was carried out under the hybrid-timing mode where an intense X-ray pulse was used as the probe pulse. This intense pulse (117 ps, 271.5 kHz) contains 16% of the total average photon flux and was separated in time from other weak X-ray pulses. A ~0.33 mM suspension of quantum dots was pumped through a stainless-steel tube to create a 600 mm diameter free jet. Two avalanche photodiodes (APDs) positioned at 90˚ on both sides of the incident X-ray beam collected the X-ray fluorescence signals. A soller slit and an additional Ni filter of 6 absorption length combination was inserted between the sample fluid jet and the APD detectors to block the scattering background. The outputs of the APDs were sent to a fast analyzer card (Agilent) triggered by a 10 kHz signal that is synchronized with the laser pulse. The card digitized the X-ray fluorescence signals as a function of time at 1 ns per point after each trigger and averaged repeated measurements using 4 s integration time. The fluorescence from the synchronized X-ray pulse at chosen delays after the laser excitation was used for creating the excited state spectrum. The ground state spectrum was obtained by averaging X-ray pulses in the previous 20 synchrotron ring cycles.

The synchronization between the laser and X-ray was achieved using a fast diode ("sample diode") with a 40 ps rise time positioned where X-ray and laser spatially overlap. The output of the sample diode was connected to an oscilloscope (Agilent, Infiniium, 8 GHz 20/40 GSa). The output trace of the sample diode was recorded with only the laser signal or X-ray input separately, then the delay between the laser and X-ray was adjusted until the signal traces from laser and X-ray overlaps on the screen of the oscilloscope. The delay was adjusted using a programmable delay line (PDL-100A-

20NS, Colby Instruments) that modulated the phase shift of the mode-lock driver for the seed laser relative to that of the RF signal of the storage ring with a precision of 500 fs. The precision of delay measurement is less than 10 ps.

The excited state X-ray spectra were created by adding the difference spectrum, increased by a specific weight ($\omega$), to the ground state spectrum. This composition is conceptually described in Figure 2.7, where the effect of weighting factors of 20×, 30×, and 40× are represented. The excited state spectra were constructed from data obtained at a delay of 90 ps. The kinetic trace was obtained by monitoring the magnitude of the X-ray absorption bleach at 8982 eV over various time delays.

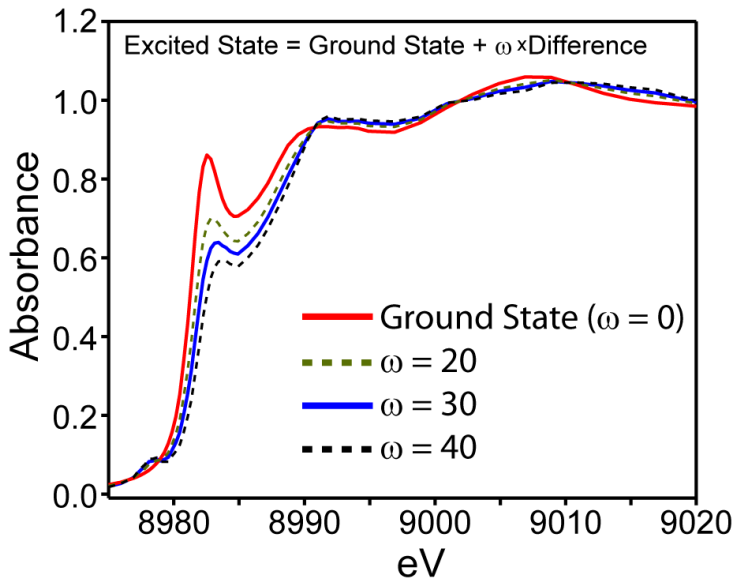


**Figure 2.7.** The excited state spectrum was created by adding an increasing weight (w) of the difference to the ground state spectrum. Shown here is the effect of using weighting factors of 20×, 30×, and 40×.

### 2.2.8 EXAFS Data Analysis.

The excited state is EXAFS spectrum was constructed by adding 20× difference spectrum (i.e., pump_on – pump_off) to the ground state spectrum to better illustrate the change in the excited state.

### 2.2.9 Experimental data reduction.

The Athena program was used to process ground state X-ray absorption data to extract the normalized oscillation amplitude in the ground state $\chi_{ground}^{exp}(k)$. Here, $k$ is the photoelectron wave number as defined by $k = \sqrt{(2m(E - E_0))/\hbar}$, where $E_0$ is the absorption edge energy, m is the electron mass, and $\hbar$ is the reduced Plank constant. Because the ground state and "pump_on" spectra were measured simutaneously, it is reaonable to assume that they have the same background aborption. Therefore, the same background as the ground state spectrum was used to extract $\chi_{excited}^{exp}(k)$ from the "pump_on" spectrum.

### 2.2.10 EXAFS Data Fitting.

The theoretical oscillation amplitude of the X-ray absorption spectrum, $\chi^{theory}(k)$, is determined using the EXAFS equation: $\chi^{theory}(k) = \sum_j \frac{S_0^2 N_j f_j(k)}{kR_j^2} e^{-2k^2\sigma_j^2} e^{-2r_j/\lambda(k)} \sin[2kR_j + \delta_j(k, r_j)]$ where $j$ indicates a shell with identical backscatters, $N_j$ is the coordination number of the $j^{th}$ shell, $f_j$ is the backscattering amplitude, $R_j$ is the average distance, $\sigma_j$ is the mean square variation, $\delta_j$ is the scattering phase shift, $\lambda$ is the effective mean free path, and $S_0^2$ is the amplitude reduction factor. In

this study, only the first Cu-S coordinate shell was used to calculate $\chi(k)$. Concerning the fit to the difference spectrum, in-house Perl scripts incorporating FEFF 9.05 were used to calculate $f_j$, $N_j$, $\delta_j$ and $\lambda$, while the structure parameters $S_0^2$, $R_j$, $\sigma_j^2$, and $E_0$ were refined by fitting the experimental data. $E_0$ were refined by fitting the experimental data. The difference spectrum fitting only included the path of the first Cu-S coordination shell. The ground and excited states shared a common $S_0^2$. The $\sigma^2$ was obtained by fixing the temperature at 300 K (i.e. room temperature) and fitting the Debye temperature.

### 2.2.11 Electronic Structure Calculations.

Density Functional Theory (DFT) modeling of small to large doped semiconductor clusters was performed using the PBE1/PBE hybrid functional,[115,116] with the SBJKC basis set and effective core potentials (ECPs).[117] Very large clusters employed the LANL2DZ basis set and ECPs[118-120] in NBO analyses. Cluster sizes varied from $CuCd_{32}S_{33}(H_4C_2O_2)_9$ to $CuCd_{137}S_{138}(H_2CO_2)_{25}$, all of which were modeled with a net single negative charge to assure a singlet spin in the ground state. The paradigm of Stener and co-workers was used to generate initial geometries, especially is it pertains to the surface ligand structure.[121] Other copper-doped semiconductors matrices, $H_{38}CuZn_{116}Se_{117}$, $H_{38}CuIn_{116}P_{117}$, and $H_{38}CuIn_{116}As_{117}$, were modeled with hydrogen termination in lieu of ligands. The indium complex $InCd_{65}S_{66}(H_2CO_2)_{18}$ was modeled with a net single positive charge to account for the loss of electron density upon replacement of an In(+3) site with Cd(+2) and to assure a singlet ground state. Undoped clusters were also studied, all of which were modeled as neutral and singlet. Gaussian '09 was used for the structure refinement and DFT, including TD-DFT, calculations,[122] as

well as natural transition orbital (NTO) analyses of the excited states.[123] The Natural Bonding Orbital (NBO) 6.0 package was used to analyze electron and hole localization in the excited states as well as bonding patterns.[124] Visualization was performed using GaussView.[125]

## 2.3 Results & Discussion.

### 2.3.1 Doped Quantum Dots.

Doped colloidal semiconductor nanocrystals have been the subject of intense study, as incorporation of guest ions allows for refinement of materials' properties beyond that afforded by quantum confinement effects.[35,36,38,42,109,126,127] Copper-doped cadmium chalcogenide NCs have been of special interest as holes are hypothesized to localize on copper.[37,128-130] This paradigm is supported by the observation of NC size-dependent dopant emission that shifts in accordance with the electron energy levels. However, in our previous study, we proposed that emission is due to copper bound electrons recombining with NC holes.[43] Clearly, indirect methods of observation will have some ambiguity in interpretation. For this reason, we sought to directly measure the oxidation state of a dopant in a semiconductor host matrix that contains free charge carriers created by photoexcitation. To this end, the cluster seed method was employed due to the method's ability to create a large quantity of homogeneous materials.

The cluster seed protocol was optimized to synthesize cadmium sulfide nanocrystals doped with four copper ions. Among the many characterizations performed, one of the simplest yet powerful demonstrations is the linear relationship that exists between the

number of seeds used and the ~5 nm quantum dots synthesized, as shown in Figures 2.8& 2.9 respectively. Furthermore, there is no evidence of emission from undoped NCs as the photoluminescence is dominated by sub-bandgap fluorescence.

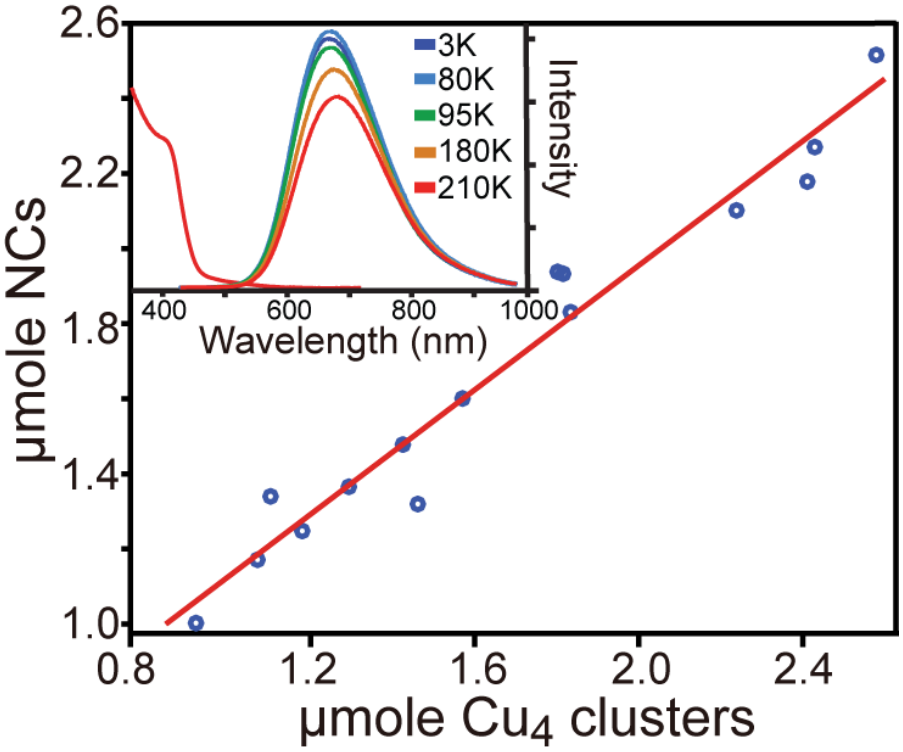


**Figure 2.8.** The number of clusters used in the synthesis is highly correlated to the quantity of nanocrystals produced. Inset: Absorption (left) and emission (right) spectra of $Cu_4$:CdS NCs.

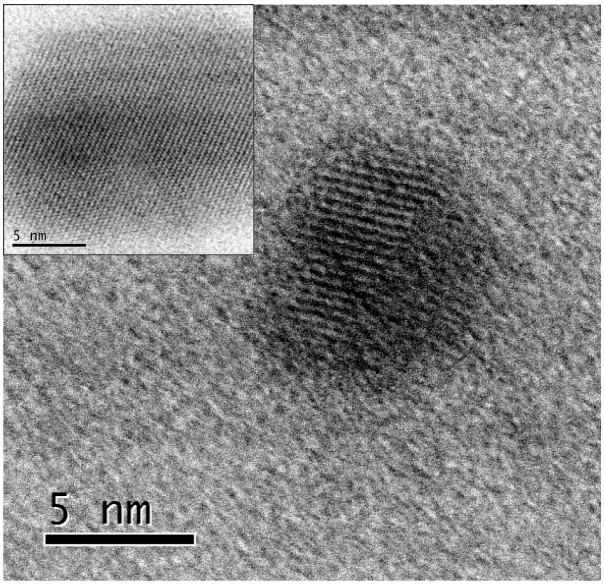


**Figure 2.9.** High resolution TEM micrographs of $Cu_4$:CdS NCs. Inset scalebar: 5 nm.

The X-ray absorption onset (Figure 2.10), lack of magnetism as revealed by SQUID measurements, and phosphorescent emission are consistent with copper dopants in the +1 oxidation state. Several other characterizations were performed, including high resolution electron microscopy, X-ray photoelectron spectroscopy (XPS), X-ray diffraction (XRD), small-angle X-ray scattering (SAXS), scanning transmission electron microscopy-electron energy loss spectroscopy (STEM-EELS), and elemental analysis (Table 2.2), all of which indicated doped $Cu_4$:CdS NCs. Moreover, the nanocrystals are not photooxidized as confirmed by emission and static XANES spectroscopies as shown in Figure 2.11, which allowed for the use of TR-XAS to study guest−host interactions.[77]

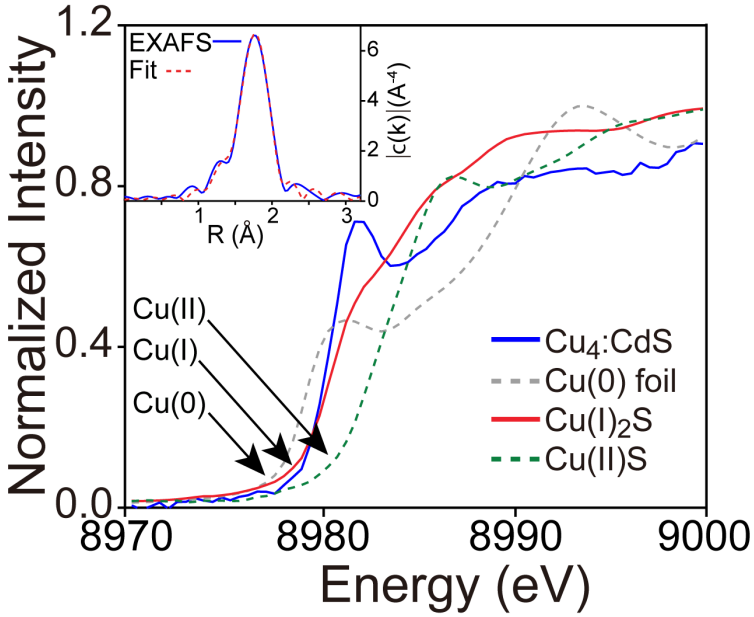


**Figure 2.10.** Static Cu K-edge XANES spectra of $Cu_4$:CdS NCs and various standards demonstrate that copper is in the +1 ground state. Inset: static EXAFS spectrum of $Cu_4$:CdS NCs.

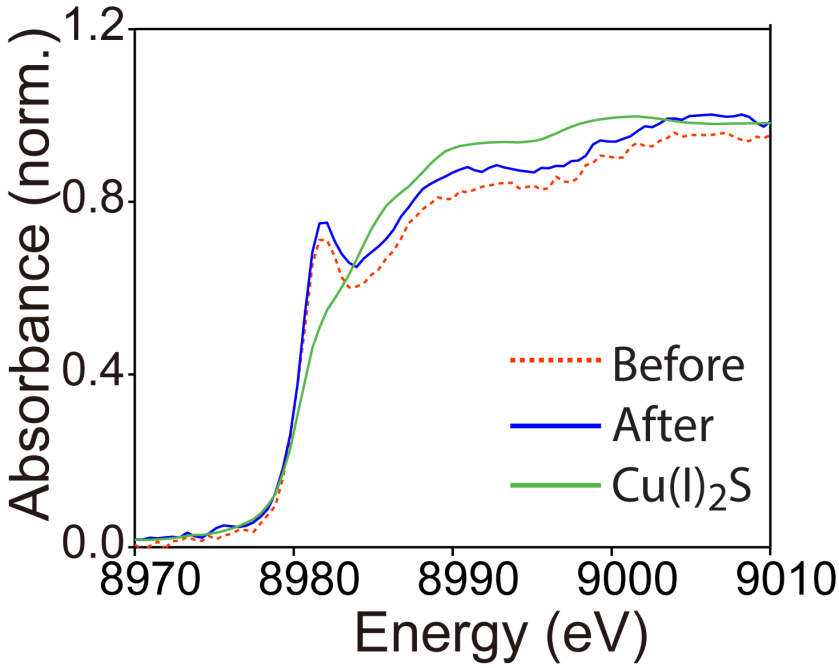


**Figure 2.11.** Copper K-edge XANES spectra of $Cu_4$:CdS samples before and after long-time exposure to high intensity UV radiation does not indicate dopant oxidation as was observed in $Cu_4$:CdSe in our previous report.[43] The photoluminescence was similarly found to be insensitive to significant exposure to UV excitation.

| Edge | Paths | Bond length (Å) | Coordination Number | Debye-Waller Factor ($Å^2$) | Energy Shift ΔE (eV) |
|---|---|---|---|---|---|
| R=1.0 – 2.2 Å<br>k= 2.0 – 12.5 $Å^{-1}$ | Cu-S | 2.177 ± 0.004 | 1.6 ± 0.1 | 0.0049± 0.0005 | 4.7 ± 0.8 |

**Table 2.1**: List of fit EXAFS parameters obtained from modeling the data for Cu edge of copper doped NC samples shown in Fig. 2.10 inset.

| Sample | Estimated Cu (ppm) | Recovered Cu (ppm) | % Incorporation |
|---|---|---|---|
| **1** | 5.0 | 4.89 ± 0.06 | 97.8 ± 1.2 |
| **2** | 5.0 | 4.538 ± 0.008 | 90.76 ± 0.16 |
| **3** | 10.0 | 9.50 ± 0.05 | 95.0 ± 0.5 |
| **Pyridine-etched** | 10.0 | 8.67 ± 0.06 | 86.7 ± 0.6 |

**Table 2.2:** Results of elemental analysis for copper in $Cu_4$:CdS NCs. Blank samples contained low levels of copper and cadmium, while the recoveries of cadmium and copper that were spiked into blank samples were within 90%. Various quantities of a freshly-prepared $Cu_4$:CdS NC sample were digested and diluted to create a sample with a concentration that was within the linear detection range of the flame AA. It was found that the amount of copper that was added in the form of clusters was recovered to 94.6 ± 0.4%, which supports the mechanism of cluster seeding. The amount of cadmium recovered was 80%, which is the same as the reaction yield. The Cd:Cu ratio was determined to be 188×, which is consistent with the size of the NCs given that each QD contains 4 copper ions. To ascertain the level of copper on the surface of the NCs, a sample was precipitated and washed with pyridine overnight. The Cu content was reduced by ~9%, which is an indicator that some ions reside on the surface. This is somewhat less than expected based on the X-ray data; however, we cannot validate the efficiency of pyridine removal of copper specifically from an NC surface.

### 2.3.2 XANES: Oxidation in the excited state.

Ultrafast time resolved X-ray absorption experiments were performed at the 11-ID-D beamline of the Advanced Photon Source at Argonne National Laboratory. The 400 nm laser pulses were stretched to 1.5 ps to negate multiphoton absorption effects as evident from the lack of nonlinear power dependence to the data as shown in Figure 2.12.

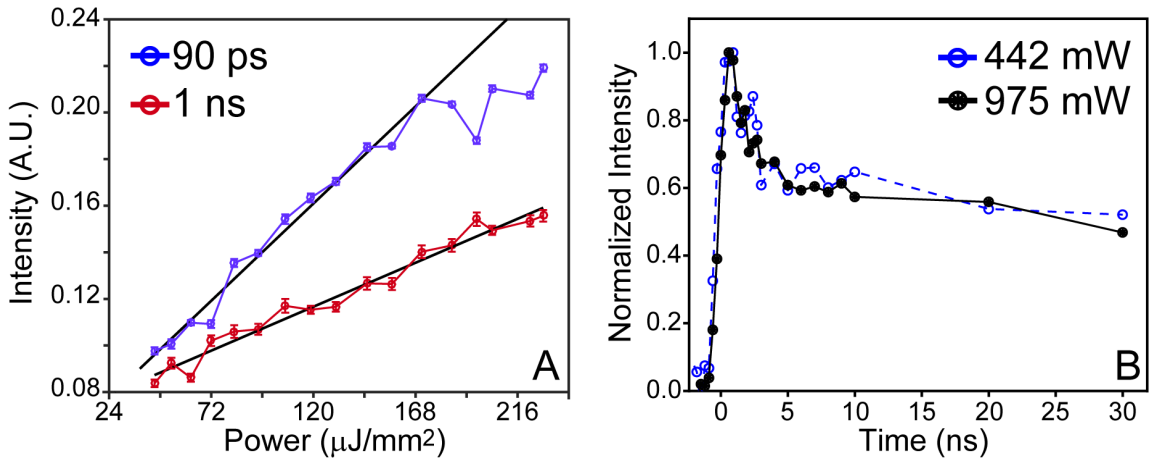


**Figure 2.12.** (A) The magnitude of the 8982 eV bleach vs. laser power at 90 ps and 1 ns delay times reveal linear power-dependent behavior, which indicates that non-linear effects. (B) Power dependent Cu oxidation kinetics as measured by the normalized magnitude of the 8982 eV XANES bleach vs. laser power.

Optical excitation was followed by X-ray interrogation at specific time delays to measure the Cu K-edge XANES and EXAFS spectra. Shown in Figure 2.13A are the difference absorption spectra (i.e., $Abs_{pump\_on}(\tau) - Abs_{pump\_off}$) at various time delays. These data were used to construct the excited-state XANES and EXAFS spectra by adding the appropriately weighted difference spectrum to the static. The result is shown in Figure 2.13B, demonstrating that the XANES absorption edge is blue-shifted by ~0.8

eV in the excited state. There is a pre-edge transition observed at 8978 eV, which originates from an electric quadrupole transition from the 1s to vacant 3d orbitals. The 1s to 3d transition feature here unequivocally demonstrates that copper dopants are oxidized to Cu(2+) by the exciton via the capture of holes because Cu(1+) and Cu(0) have no vacant 3d orbitals. The main edge transition between 8988 and 8997 eV corresponds to excitation from 1s → 4p unoccupied orbitals. The strong absorption at the rising edge peaked around 8982 eV is ascribed to a 1s → {4p + shakedown} transition.[131-133] The significant reduced intensity of this transition after excitation suggests increased 3d−4p hybridization. Stronger 3d−4p mixing increases the electron density in the 4pz orbital, thereby reducing the transition intensity.[134,135]

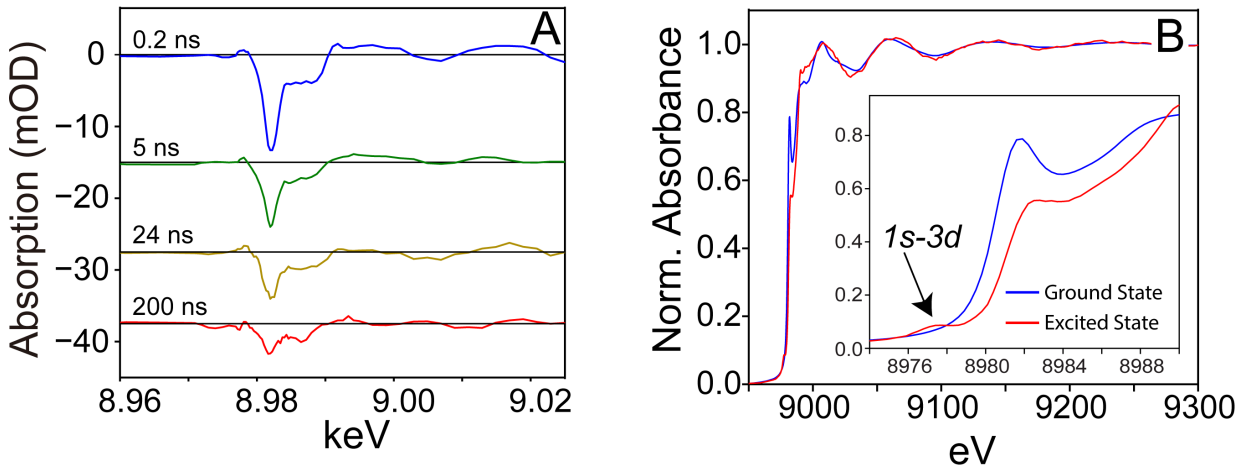


**Figure 2.13**. (A) TR-XAS difference spectra at the Cu K-edge. (B) The XANES spectra of the ground and excited states of copper in $Cu_4$:CdS semiconductor nanocrystals. A 1s → 3d pre-edge transition feature is observed at 8978 eV as shown in the inset.

### 2.3.3 DFT models: Surface and interior-doped NCs.

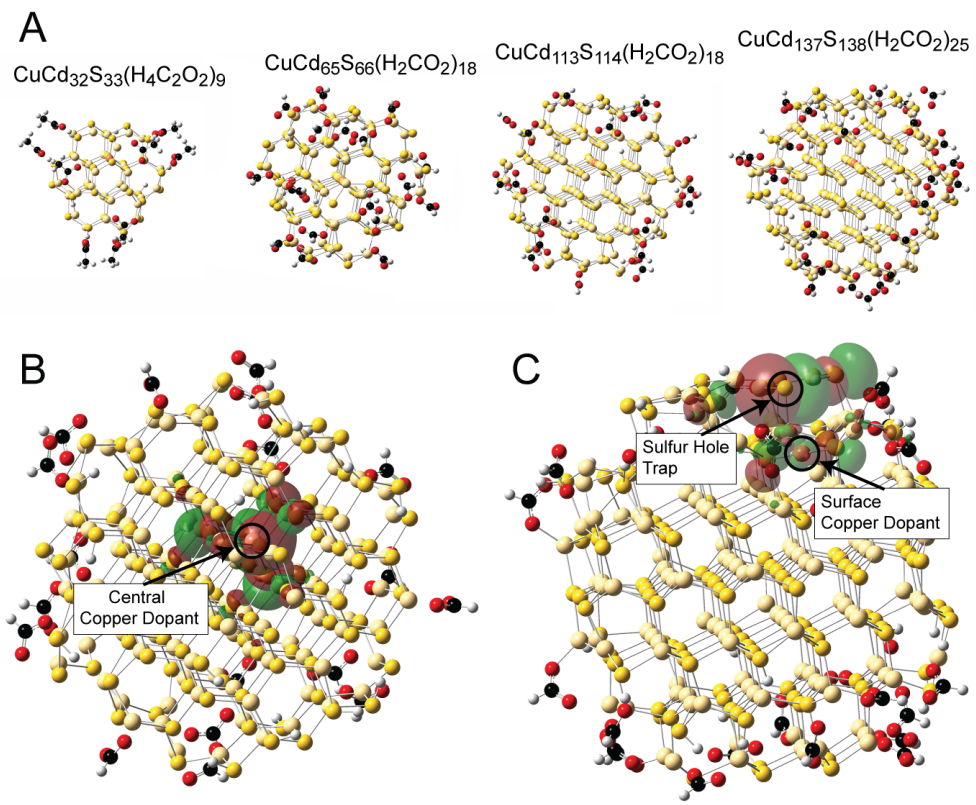


**Figure 2.14.** (A) Natural Transition Orbital analysis of the optimized DFT geometries of a size series of interior-doped clusters demonstrates the localization of holes by Cu in the 1st excited state. (B) Optimized DFT geometry of $CuCd_{113}S_{114}(H_2CO_2)_{18}$ where the copper dopant is localized near the surface of the NC. The hole is centered on the dopant in the excited state. (C) Copper near the surface of a larger $CuCd_{137}S_{138}(H_2CO_2)_{25}$ nanocrystal creates a S-centered hole state with some admixture of Cu character.

The 1s → 3d pre-edge XANES feature and other absorption shifts are indicative of a modulation of the local structure around the guest ion in the excited state. This prompted us to compare the ground state (i.e., static) and the excited state EXAFS spectra, the results from which were augmented with DFT-optimized geometries of both the ground and first excited (triplet) states of small $CuCd_{32}S_{33}(H_4C_2O_2)_9$ (1.3 nm) to large

$CuCd_{137}S_{138}(H_2CO_2)_{25}$ (2.2 nm) clusters, including ligands, as shown in Figure 2.14A. Natural Bond Orbital (NBO) analyses of the DFT results were employed to assist with describing the bonding and localization of charge in a manner similar to a Lewis diagram representation.[136] Both interior and surface doped systems were modeled because the fit to the ground state EXAFS data shown in Table 2.1 reveals that copper is coordinated with two nearest S atom neighbors. This strongly suggests that dopants largely reside at the surfaces of CdS NCs,[130,137] and that copper ions located within the interior must be a minority of the sample population. Such a heterogeneous population likely forms due to the known diffusivity of copper, even through a solid-state material.[138] Regardless, all the systems except the largest surface-doped model discussed below have copper ions that are formally nonbonded to the nearest sulfur sites according to NBO analysis of the ground state. However, oxidation of copper in the first excited state results in the formation of bond(s) with one or two of the nearest-neighbor sulfur sites to regain electron density as evident from the ~0.05 Å compression of the Cu−S distances in the excited states' optimized geometries shown in Figure 2.15 and from NBO analyses. This effect was observed in several copper doped semiconductor clusters such ZnSe ($H_{38}CuZn_{116}Se_{117}$), InP ($H_{38}CuIn_{116}P_{117}$), and InAs ($H_{38}CuIn_{116}As_{117}$)

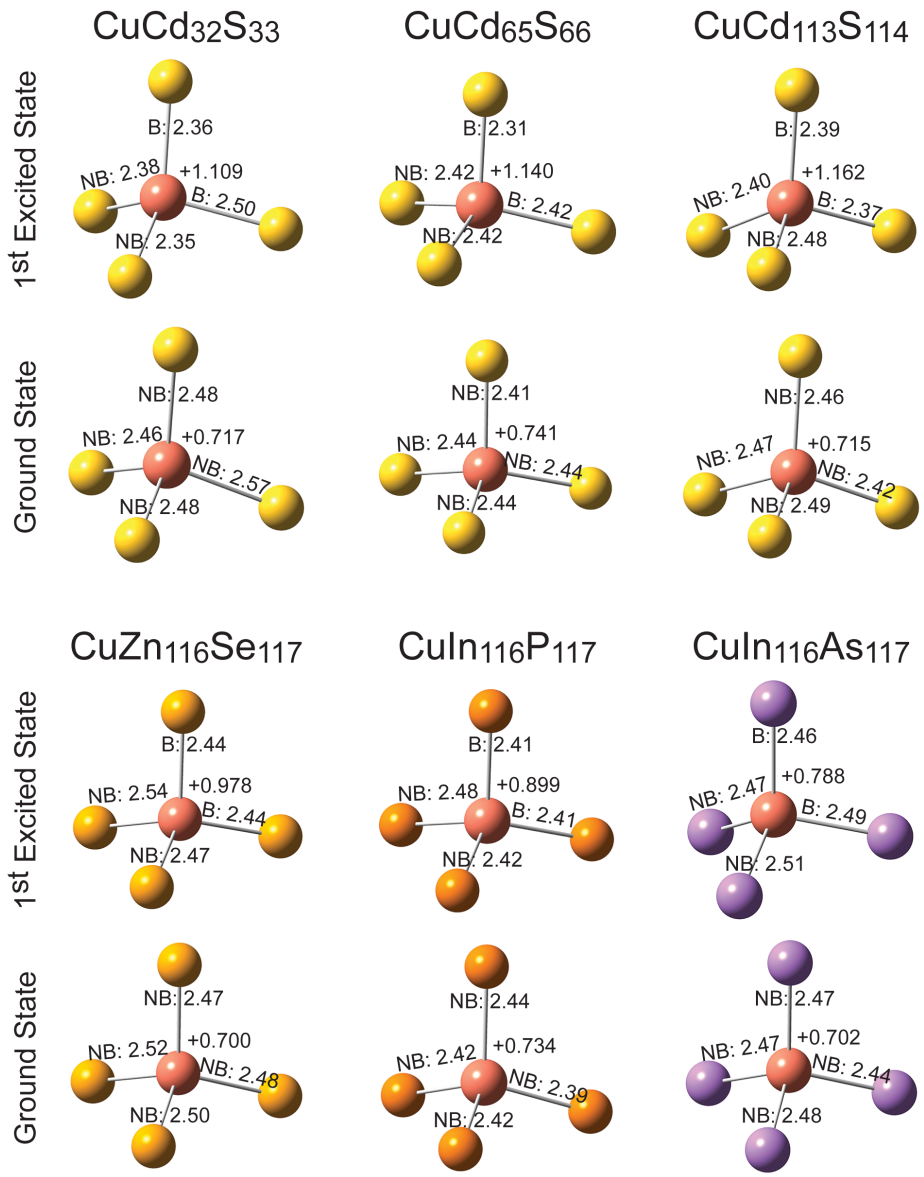


**Figure 2.15.** Optimized local Cu-centered geometries of copper-doped CdS, ZnSe, InP, and InAs clusters in the ground singlet 1st excited triplet states. The magnitude of bond rearrangement correlates with the degree of oxidation of the Cu dopant as indicated. The bond rearrangement is also proportional to the energy of the valence band, where shallow HOMO levels in the neat semiconductor (InAs, and InP to a lesser extent) result in less oxidation and bond rearrangement in the copper-doped cluster. NB: not bonded. B: single bond, although NBO analysis consistently finds occupancy of antibonding orbitals in all cases shown above.

As stated above, a different behavior was characterized from DFT calculations of the largest surface-doped $CuCd_{137}S_{138}(H_2CO_2)_{25}$ system. In "type-II" surface model, copper is flanked by two sulfur sites at 180°, as shown in Figures 2.14C and 2.16. This coordination environment creates a nearby sulfur-centered hole trap state with partial Cu character, which negates copper oxidation in the excited state. This also removed the electronic drive for Cu−S bond formation in the excited state. As detailed below, this configuration creates a surface-defect-type emission yet does not significantly contribute to the TR-XAS signal due to the fact that Cu is not oxidized in the excited state.

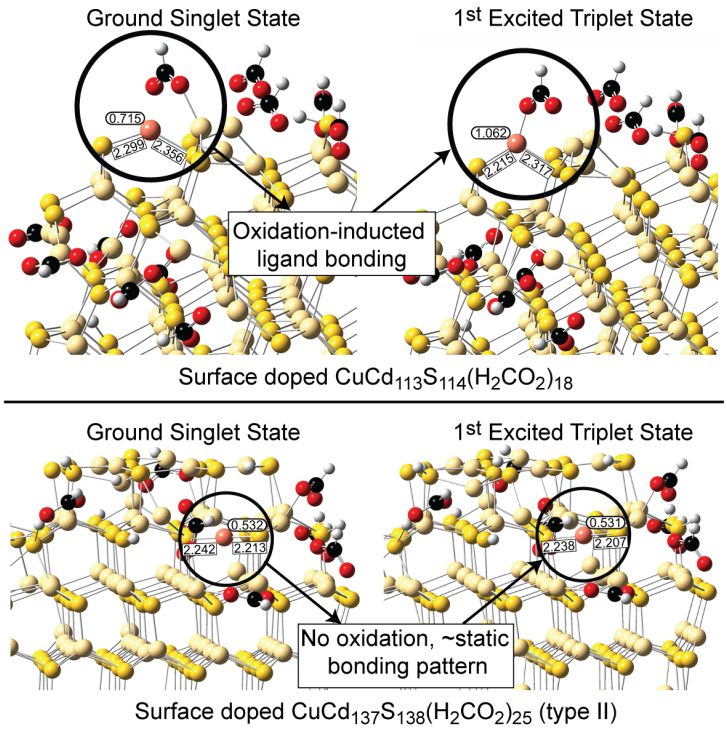


**Figure 2.16.** (Top) The effect of charge-modulated dopant bonding observed in copper atoms at the surfaces of smaller clusters. As shown here, oxidation of the surface-bound copper instigates bonding to a nearby ligand. (Bottom) For a type-II dopant found on the surface of the larger cluster, there is minimal rearrangement of the coordination sphere due to the lack of significant oxidation of the dopant in the excited state. Squares represents Cu-S distances, ovals convey the partial charge from NBO analysis.

### 2.3.4 EXAFS: Bonding in the excited state.

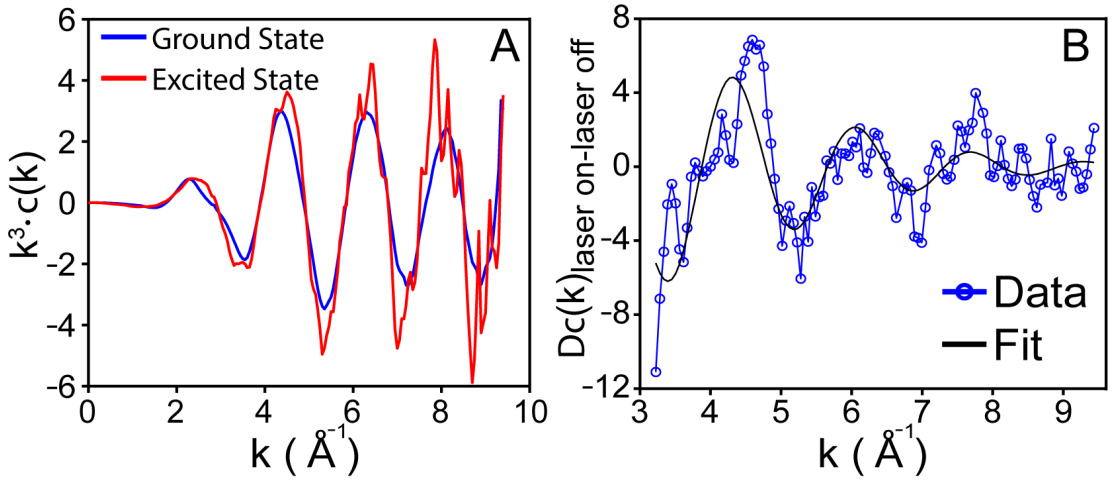


**Figure 2.17.** (A) EXAFS k-space spectra of the ground and excited states. (B) The ground to excited state difference EXAFS spectrum and the best fit demonstrate a shortening of the Cu-S bond length.

Figure 2.17A shows the Cu K-edge EXAFS ground- and excited-state spectra of the doped nanomaterials. The oscillation period in the excited state is shorter, potentially indicating that the Cu–S bond has expanded upon excitation. However, this is contradictory to the fact that copper should form shorter Cu–S bonds in the excited state due to oxidation of the dopant,[139] which is confirmed by the appearance of the 1s–3d transition peak, the blue shift of the transition edge in the excited-state XANES spectrum, and the DFT results. We propose that this paradox is due to heterogeneous Cu–S bond dynamics resulting from the existence of surface and interior copper species as predicted by DFT and corroborated by the kinetic behavior. Two types of Cu–S bonds have different structural responses upon photoexcitation, and the interferences created from the two oscillations may lead to an apparent overall shorter oscillation period. We conducted simulations to test this hypothesis. According to DFT calculations, the type-II surface

Cu–S bonds do not rearrange in the excited state, as shown in Figure 2.16. This prompted us to simulate a series of EXAFS spectra with scattering contributions from two types of Cu–S bonds that include a shrinking interior Cu–S bond and a static surface bond. Figure 2.18 shows one example of these simulated ground-state and excited-state spectra, the results of which show a similar effect (a shortening oscillation period) as observed in the experimental data.

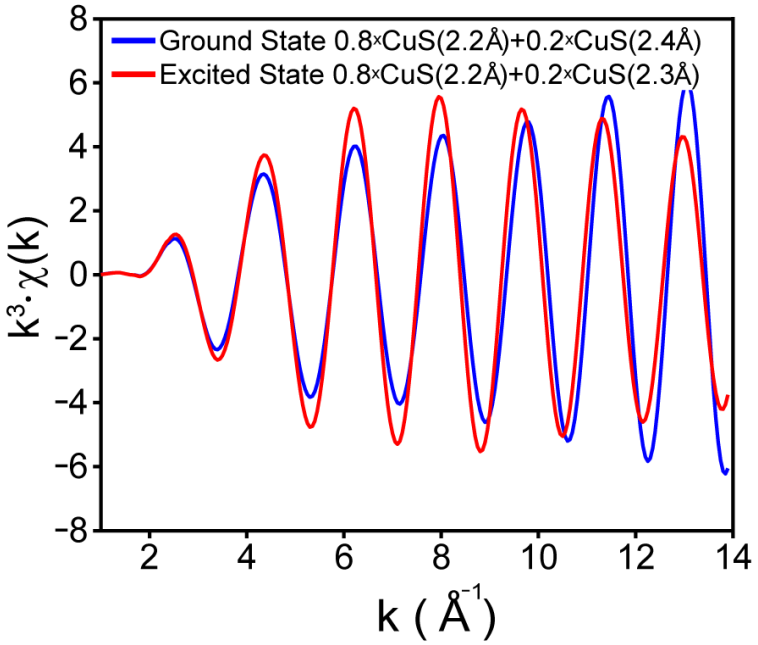


**Figure 2.18.** A simulated spectrum of the excited state Cu-K EXAFS (red line) has a smaller oscillation period in the k range of 3 $Å^{-1}$ to 9.4 $Å^{-1}$ compared to the ground state (blue line). However, this is the result of interference between two scattering signals as this simulation is composed of 80% amplitude from a 2.2 Å Cu-S bond and 20% from a 2.3 Å Cu-S bond, while the ground state is generated from a composition of 80% amplitude from a 2.2 Å Cu-S bond and 20% from a 2.4 Å Cu-S bond. These simulations reproduce the data shown in Fig. 2.17.

It is challenging to directly extract excited-state structural parameters using conventional X-ray absorption data analysis due to this heterogeneity. Assuming static surface Cu−S bonds, the net change in the EXAFS spectrum is only defined by the absorption difference with the interior Cu−S bond, A × [ $\mu_{excited}^{inter}(k) - \mu_{ground}^{inter}(k)$], where μ is the experimental measured absorption coefficient and A is a constant. This approach allowed us to determine the Cu−S bond lengths. Due to the fact that the pump_on and pump_off spectra were measured simultaneously, it was assumed that they have the same background absorption. Therefore, $[\mu_{excited}^{inter}(k) - \mu_{ground}^{inter}(k)] = [\chi_{excited}^{inter}(k) - \chi_{ground}^{inter}(k)]$. Figure 2.17B shows the data and the best fit to the difference spectrum. The average interior Cu−S bond lengths for ground and excited state were determined to be 2.40 ± 0.02 and 2.32 ± 0.02 Å, respectively, from the best fit. Note that the 0.08 Å bond compression in the excited state is similar to that predicted by DFT.

Overall, these data demonstrate that copper is oxidized in the excited state, which instigates a shortening of the Cu−S bond length for interior-bound guest ions. This is consistent with the DFT data that dictate that interaction of the dopant with the excess charge carrier results in a modulation of the dopant bonding to the semiconductor host matrix. Such an interaction phenomenon that is akin to small polaron dynamics as the modulation of dopant ion bonding induced by interaction with a charge carrier likely results in lower charge carrier mobility.[140-142] To examine the generality of this phenomenon, additional guest/host systems were theoretically investigated, including Cu-doped CdSe, ZnSe, InAs, and InP. It was found that interaction of charge carriers modulated the bonding of the dopant in the excited state in every model system, shown in Figure 2.15. The impact of the effect was found to be dependent on the valence potential

of the host, as copper is less oxidized and subsequently has weaker bonding to a matrix with a higher energy valence state. The effect of electron capture by a guest ion was also studied using an indium-doped $InCd_{65}S_{66}(H_2CO_2)_{18}$ cluster model. Indium is bonded to four nearest-neighbor S-sites in the ground state. However, in the first excited state, the dopant is reduced, which ruptures a bond with one of the nearest-neighbor sulfur atoms; shown in Figure 2.19.

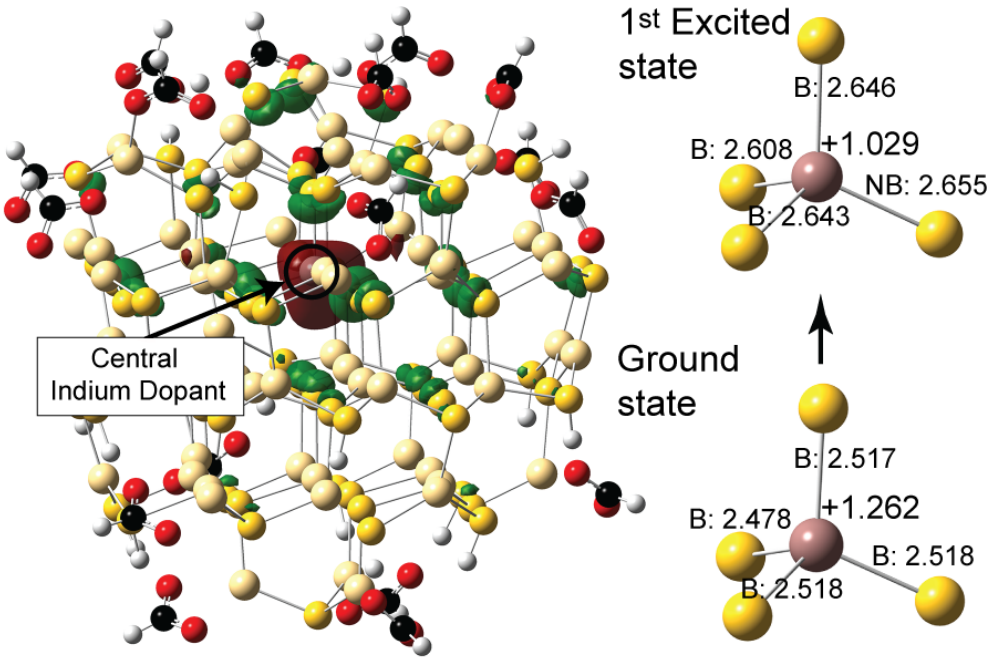


**Figure 2.19.** NTO orbital analysis of the 1st excited state of an interior-doped $InCd_{65}S_{66}(H_2CO_2)_{18}$ cluster demonstrates the addition of electron density on the In dopant in the excited state. The optimized geometry of the 1st excited state displays longer In-S bonds, while NBO analysis dictates that one of the bonds is broken while the remaining gain additional charge density in antibonding orbitals. NB: not bonded. B: single bond.

Theoretical calculations also predict that the effect of carrier-modulated dopant bonding can be mollified or enhanced by tailoring the material system. To demonstrate, the four nearest neighbors of an interior doped $CuCd_{65}S_{66}(H_2CO_2)_{18}$ model were replaced with either oxygen or selenium. It was found that the extent of rebonding in the excited state was significantly reduced with selenium nearest neighbors, whereas the opposite was true with oxygen, as shown in Figure 2.20. This information may allow for the design of materials to tune the dopant−charge carrier interaction and potentially reduce scattering. Furthermore, the cluster seeded doping method may allow for the experimental realization of such advanced materials, as we demonstrated in our previous publication that the cluster seed remains partially intact during QD synthesis.[43]

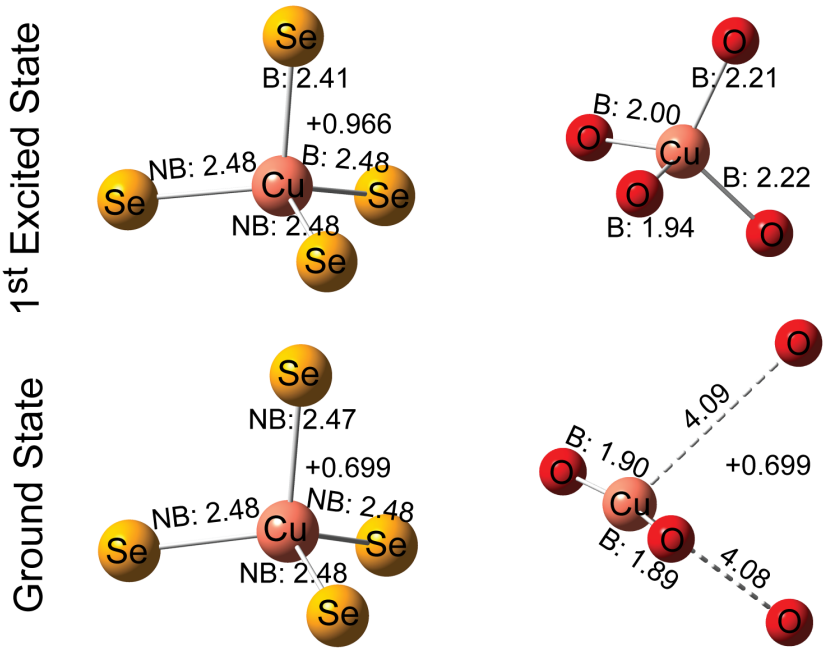


**Figure 2.20.** Optimized local Cu-centered geometries of copper-doped $CuCd_{65}Se_4S_{62}(H_2CO_2)_{18}$ and $CuCd_{65}O_4S_{62}(H_2CO_2)_{18}$ clusters in the ground singlet 1st excited triplet states. The magnitude of bond rearrangement and oxidation of the dopant is dependent on the identity of the nearest neighbors. NB: not bonded. B: single bond.

### 2.3.5 Oxidation and PL dynamics.

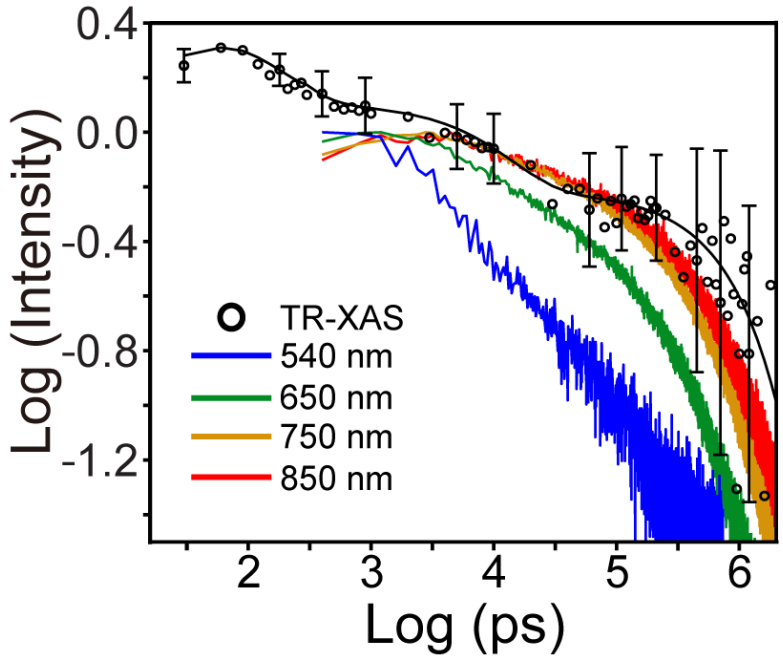


**Figure 2.21.** Copper oxidation kinetics compared to time-resolved emission dynamics at different probe wavelengths.

The kinetics of dopant oxidation shown in Figure 2.21 reveals significant complexity as they are only partially consistent with the time-resolved photoluminescence data. There is an initial sub-nanosecond relaxation that is not observed in the photoluminescence data at any wavelength. This dynamic must originate from the recombination of electrons with oxidized surface-bound copper for several reasons, including the fact that surface-doping preformed QDs with copper results in significant fluorescence quenching. Furthermore, the EXAFS fitting was consistent with a population of surface-dopant species. This nonradiative recombination is followed by short ~10 ns and longer ~1 μs time scale components that have analogs in the

photoluminescence data. Most likely, these are the radiative dynamics of interior-bound copper-centered holes recombining with excitonic and surface-trapped electrons. What is very curious is that there is a ∼100 ns dynamic in the photoluminescence that is not observed in the TR-XAS data. As this time scale is very similar to that observed from electron−hole recombination at charge trapping surface states,[143,144] and the fact that DFT modeling reveals that dopants may not be significantly redox-active if they generate hole-trapping surface states,[143] this dynamic is attributed to emission from type-II surface-doped copper species. Overall, these data demonstrate that one may not assume that time-resolved dopant-modulated emission tracks the photochemical dynamics of the same species. Rather, the sub-bandgap emission from doped semiconductors may result from a complex convolution of interior and surface-bound species that may, or may not, have redox-active excited-state behavior.

| Wavelength (nm) | Amp. | τ (ps) | Amp. | τ (ns) | Amp. | τ (ns) | Amp. | τ (ns) |
|---|---|---|---|---|---|---|---|---|
| **540** | - | - | 0.733 | 2.65± 0.06 | 0.190 | 35.5±1.3 | 0.076 | 348±8 |
| **550** | - | - | 0.699 | 3.46± 0.06 | 0.214 | 55.5±1.3 | 0.087 | 428±7 |
| **600** | - | - | 0.481 | 9.51± 0.10 | 0.317 | 118.1±1.2 | 0.203 | 546±3 |
| **650** | - | - | 0.375 | 17.06± 0.15 | 0.377 | 178.5±1.3 | 0.248 | 695±3 |
| **690** | - | - | 0.346 | 21.5±0.2 | 0.377 | 210.9±1.7 | 0.277 | 782±3 |
| **700** | - | - | 0.335 | 21.6±0.2 | 0.382 | 219.0±1.7 | 0.283 | 814±3 |
| **750** | - | - | 0.303 | 20.3±0.3 | 0.369 | 225±2 | 0.328 | 881±4 |
| **800** | - | - | 0.304 | 20.1±0.5 | 0.348 | 234±4 | 0.347 | 954±6 |
| **850** | - | - | 0.306 | 18.4±0.9 | 0.336 | 223±7 | 0.358 | 993± 11 |
| **900** | - | - | 0.343 | 16.1±1.1 | 0.349 | 235±7 | 0.308 | 1088± 11 |
| **TR-XAS** | 0.49 ± 0.07 | 160 ± 80 | 0.27 ± 0.04 | 11 ± 9 | - | - | 0.24 ± 0.04 | 1100 ± 500 |

**Table 2.3.** Multi-exponential fit parameters to time- and wavelength-resolved photoluminescence data. The TR-XAS oxidation kinetic data were quantified by integrating the magnitude of the bleach signal at 8982 eV.

## 2.4 Conclusion.

Time-resolved X-ray absorption spectroscopy coupled with large-scale DFT calculations offers unambiguous insight into the photophysical properties of semiconductor dopants in nanostructures. To conduct this study, large batches of exactly doped $Cu_4$:CdS NC samples were synthesized via the cluster seeding method. The population of copper ions is found to be divided between interior doped and two types of surface-bound species. A microscopic picture of the electronic structure of these guest ions in the presence of charge carriers was obtained, the dynamics of which demonstrate that dopant bonding is modulated by their interaction with free charge carriers. Note that there were some differences in the dynamics of interior dopants versus the surface-bound ions. We believe that a variety of doped semiconductor materials display these dynamics, which likely impacts charge transport characteristics of QD "artificial solids" and even bulk materials due to chemical trapping of charge carriers at dopant sites. These results demonstrate the necessity of using powerful techniques such as TR-XAS to generate a comprehensive understanding of the electronic structure and dynamics of advanced materials.

# 3 Electronic Structure and Dynamics of Copper Doped Indium Phosphide Nanocrystals Studies with Time-resolved X-ray Absorption Spectroscopy and Large-Scale DFT Calculations

The content of this chapter has been published as "Electronic Structure and Dynamics of Copper Doped Indium Phosphide Nanocrystals Studies with Time-resolved X-ray Absorption Spectroscopy and Large-Scale DFT Calculations", A. Hassan, X. Zhang, C. Liu P. T. Snee*. *Journal of Physical Chemistry C*, 2018, ASAP. Reproduced with permission from the American Chemical Society.

## 3.1 Introduction

A central theme of the research of this thesis is the study of doping transition metal ions into semiconductor nanocrystal hosts. This creates materials with new optoelectronic properties that result from modulation of the bandgap, an increase in charge carrier density, and guest ion−semiconductor exciton interactions among others as described in the previous chapter.[38,42,128,145-149] As a result, doped NCs are an emerging class of materials that have been frequently studied and used in numerous applications due to tunability of high quantum yield emission, long radiative lifetimes, large Stokes shift, and enhanced charge carrier density.[126,150,151] Doped NC films are being extensively explored for alternative energy generation.[152,153] The results presented in chapter two focused on cadmium-based material host. However, concerns over the use of RoHS-prohibited metals impairs commercial realization.[154-156] There is significant potential for developing applications with other NC core materials such as silicon, zinc selenide, copper indium sulfide, and members of the III-V semiconductor family.[157-161] For example, indium phosphide semiconductor nanomaterials are of interest in lighting and display

technologies.[162,163] However, InP NCs are known to be very difficult to synthesize,[164-166] and there are correspondingly few reports on the doping of the same.

We previously used cluster seeding to produce exactly Cu-doped II-VI semiconductor NCs, specifically CdSe:$Cu_4$ and CdS:$Cu_4$,[43,44] that were examined with time resolved X-ray absorption spectroscopy (TR-XAS) and density functional theory (DFT) modeling as reported in chapter two. These data unambiguously revealed a microscopic description of dopant electronic structure in the ground and excited states, including the observation that charge carrier localization on a dopant may result in a modulation of the guest ion's bonding to the underlying semiconductor matrix.[44] We now investigate InP:$Cu_4$ NCs to study dopant electronic structure in III-V semiconductor hosts. Semiconductor InP has a direct band gap, a diamond-like zinc blende crystal structure, and is covalently bonded.[167] The III-V family is very important in applications for efficient solar cells, lasers, and many others.[168-170] As such, the study of dopant dynamics in this material provides an interesting contrast to that observed in II-VI host NCs and will guide the development of new material systems with enhanced electrical properties. We can also characterize the dynamics of the dopant electronic structure, which would be erstwhile impossible in this non-emissive InP semiconductor system.

## 3.2 Experimental.

### 3.2.1 Materials.

1-Octadecene (90%), oleylamine (90%), indium (III) acetate ($In(ace)_3$, 99.99%), myristic acid (99%), and tris(trimethylsilyl)phosphine ($(TMS)_3P$, 95%) were purchased from Sigma-Aldrich. Trioctylphosphine (97%) was purchased from Strem. Oleylamine was purified by recrystallization at −30 °C from acetonitrile and was stored at 4 °C. All other reagents were used without further purification.

### 3.2.2 InP:$Cu_4$ Synthesis Using $[N(Me_4)]_2[Cu_4(SPh)_6]$ as Seeds.

Into a 50 mL three-neck flask were added 10 mL of 1-octadecene, 1.4 mL of purified oleylamine, 0.14 g (0.5 mmol) of indium acetate, and 0.45 g (2 mmol) of myristic acid. The solution was heated to 110 °C under vacuum for 1 h. After the solution turned clear the vessel was backfilled with $N_2$ and cooled to room temperature. Next, a solution of 1.6→4.8 mg of $[N(Me_4)]_2[Cu_4(SPh)_6]$ and 0.128 g of tris(trimethylsilyl)phosphine in 1.7 mL TOP was added dropwise at room temperature into the degassed solvent. The solution was slowly heated to 50 °C, and after ~1 hr a slight yellow color was observed. The solution was then heated gradually to 110 °C at a rate of 5 °C/min and was maintained at this temperature for ~16 h. The doped NCs prepared using this method were stored in a glove box and were later used for optical, XRD, and XPS characterization.

### 3.2.3 Scaled synthesis of InP:$Cu_4$ using $[N(Me_4)]_2[Cu_4(SPh)_6]$ as seeds.

Into a 100 mL three-neck flask were added 70 mL of 1-octadecene, 10 mL of purified oleylamine, 1.04 g (3.56 mmol) of indium (III) acetate, and 3.05 g (13.35 mmol) of myristic acid. The solution was heated to 110 °C under vacuum for 1 h. After the solution turned clear the vessel was backfilled with $N_2$ and cooled to room temperature. Next, a solution of 9.0 mg of $[N(Me_4)]_2[Cu_4(SPh)_6]$ and 0.9 g of tris(trimethylsilyl)phosphine in 12 mL TOP was added dropwise at room temperature into the degassed solvent. The solution was slowly heated to 50 °C, and after ~1 hr a slight yellow color was observed. The solution was then heated gradually to 110 °C at a rate of 5 °C/min and was maintained at this temperature for ~16 h. The doped NCs prepared using this method were stored in a glove box and were later used for XAS measurements.

### 3.2.4 Characterization.

UV−vis absorbance spectra were measured using a Varian Cary 300 Bio UV−vis spectrophotometer. Transmission electron microscopy (TEM) measurements were performed using a JEOL JEM-3010 operating at 300 keV. A 300 mesh gold grid was used for TEM analysis. X-ray diffraction (XRD) studies were performed on a D8 AdvanceECO Bruker XRD diffractometer using a graphite monochromator and a proportional detector. The power generator was operated at 40 kV and 20 mA. X-ray Photoelectron Spectroscopy (XPS) analyses were performed on a Kratos Axis 165 using a monochromatic Al Kα source operating at 12 kV and 10 mA to produce an X-ray power of 120 W. Spectra were collected with a photoelectron takeoff angle of 90° from

the sample surface plane, in energy steps of 0.1 eV, and a pass energy of 20 eV for all elements. X-ray absorption spectroscopy measurements and density functional theory (DFT) modeling were obtained as discussed previously in Chapter 2.

## 3.3 Results & Discussion.

### 3.3.1 Doped Quantum Dots: structure and composition.

The synthesis of colloidal semiconductor nanocrystals doped with transition metal ions has been studied as the incorporation of guest ions allows for refinement of materials' electronic, optical, and magnetic behaviors beyond that realized by quantum confinement effect.[38,42,128,145-149] As such, it is important to understand the electronic structure of doped semiconductors to further aid the incorporation of these materials for applications such as alternative energy generation. As discussed in the previous chapter, we recently reported that dopant ions modulate their bonding to the underlying semiconductor matrix as they interact with charge carrier.[44] This phenomenon was observed in copper doped cadmium sulfide NCs, and we predicted that the same would occur in several other systems including indium phosphide doped with copper. This effect has implications on our understanding of doped semiconductor systems that may lead to more efficient electronic devices, as such bonding dynamics creates a charge carrier scattering potential that is detrimental for efficient conduction.[171]

The III-V family has significant relevance to the semiconductor industry.[172-174] For this reason, we sought to investigate the electronic structure and dynamics in Cu-doped InP NCs. Key to success is our recent developed cluster seeding method to synthesize

doped semiconductor NCs where each particle contains the same number of guest impurities.[43,44] Using this strategy, indium phosphide nanocrystals were nucleated around a small organometallic $[N(Me_4)]_2[Cu_4(SPh)_6]$ cluster with $(TMS)_3P$ and $In(ace)_3$ at low temperature to incorporate four copper atoms per NC. The obtained InP:$Cu_4$ NCs were characterized optically and with transmission electron microscopy (TEM), as well as with X-ray based techniques such as powder X-ray diffraction (XRD), X-ray photoelectron spectroscopy (XPS), and X-ray absorption spectroscopy at the Cu-K edge.

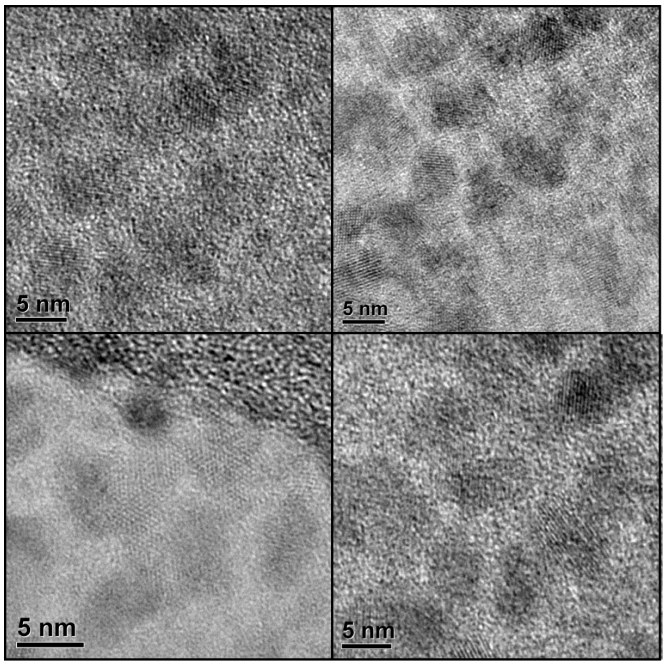


**Figure 3.1.** TEM micrographs of copper doped InP NCs demonstrates the formation of ~5 nm InP nanoparticles.

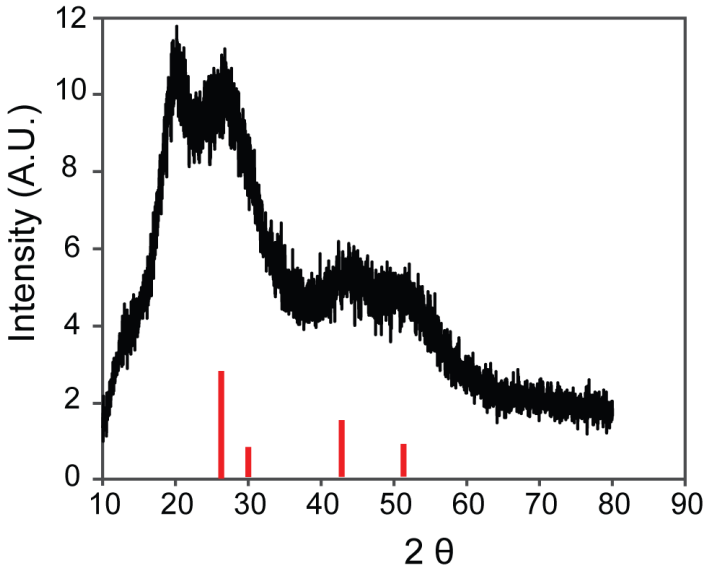


**Figure 3.2.** X-ray diffraction spectrum of copper doped InP NCs is consistent with small particles that have a zinc blende structure; bars are from PDF 00-032-0452.

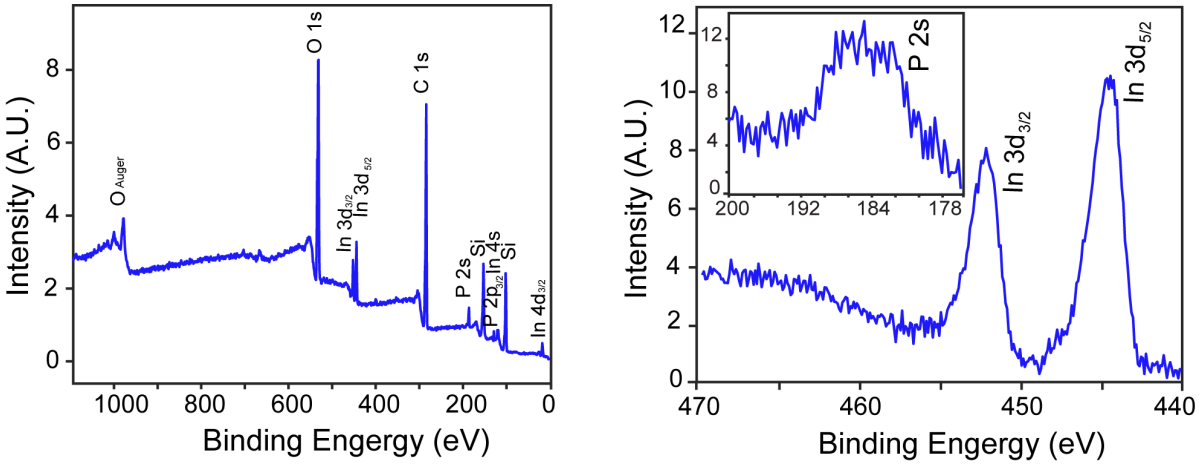


**Figure 3.3.** XPS spectra of copper doped InP. Analysis of the spectra validates the formation of indium phosphide NCs when compared to the NIST database.

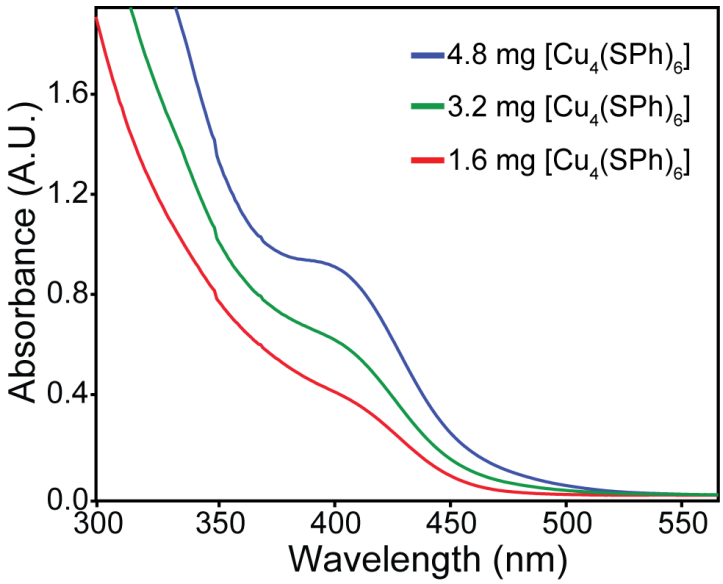


**Figure 3.4.** Absorption spectra of InP:$Cu_4$ NCs as a function of the addition of Cu cluster.

The materials characterization data reveal that $[N(Me_4)]_2[Cu_4(SPh)_6]$ clusters are functional seeds for the growth of InP nanocrystals. The TEM micrographs in Figure 3.1 demonstrate the synthesis of small, ~5 nm diameter crystals using the seeded growth protocol. The crystal phase of the NCs was confirmed by powder X-ray diffraction (XRD), see Figure 3.2. It is consistent with the characteristic pattern of the zinc blende crystal lattice of InP, and has broad resonances that are indicative of the small sizes of the individual particles. XPS spectra shown in Figure 3.3 reveal the elemental signatures of InP. Most telling is the fact that the absorption spectra in Figure 3.4 are a function of the number of cluster seeds used in the synthesis. These data demonstrate that the materials' bandgaps and overall absorptivities increase with addition of greater quantities of cluster seeds in the syntheses. The bandgap widens due to the fact that more dots are competing

for less precursors, which results in the synthesis of smaller InP NCs. The overall absorptivity is greater due to the formation of more dots as well. Overall, there appears to be a linear relationship between the amounts of cluster used *vs.* the NCs produced, and thus we conclude that the copper clusters are acting as nucleation sites for the NCs. Unlike the previous work CdS:$Cu_4$ NCs, we could not create a regression of NCs produced *vs.* cluster used due to the due to the small sizes of the copper doped InP dots.

### 3.3.2 Static and Time Resolved X-ray Absorption

Static and time resolved X-ray Absorption Near Edge Spectroscopy (XANES) and Extended X-ray Absorption Fine Structure Spectroscopy (EXAFS) were used to characterize the doping of InP:$Cu_4$ NCs and to examine the excited state electronic structure of the copper guest ions in the presence of photogenerated charge carriers.[175,176] The static XANES data discussed below reveal that Cu is in the +1 oxidation state, while the EXAFS spectra shown in Figure 3.5 were used to calculate the radial distribution function that is dependent on the identity of nearby scattering centers in the 1$^{st}$ coordination shell. Although consideration of only phosphorus nearest neighbors provides a good fit to the EXAFS data, the most robust model shown in Figure 3.5 was realized by inclusion of both Cu-P and Cu-S scattering and the parameters are provided in Table 3.1. This result suggests that some copper NC dopants remain bound to sulfur that originated from the original cluster seed. A similar observation was made in our previous study on Cu-doped CdSe, and overall demonstrates that the cluster seed method allows for doping NCs with both the guest ions and potentially for tuning the local coordination sphere of the dopants.

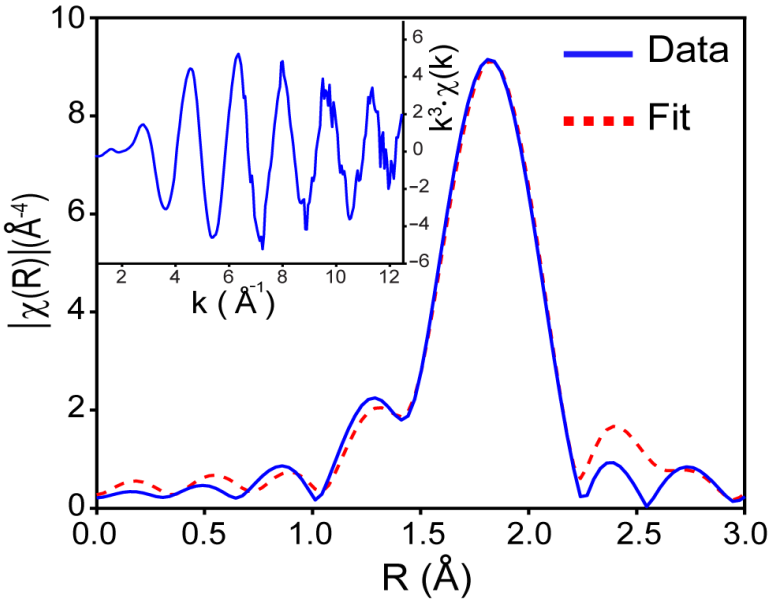


**Figure 3.5.** Static EXAFS scattering radial distribution of copper doped InP NCs as fit with both Cu-P and Cu-S scattering components. Inset: Weighted k-space of the EXAFS region.

| Edge | Paths | Bond length (Å) | Coordination Number | Debye-Waller Factor ($Å^2$) | Energy Shift ΔE (eV) |
|---|---|---|---|---|---|
| R=1.0 – 2.4 Å<br>k= 3.0 – 11.5 $Å^{-1}$ | Cu-P | 2.240 ± 0.006 | 2.34 ± 0.14 | 0.0041± 0.0007 | 1.8 ± 0.7 |
| | Cu-S | 2.840 ± 0.006 | 0.32 ± 0.14 | 0.0041± 0.0007 | 1.8 ± 0.7 |

**Table 3.1**: List of fit EXAFS parameters obtained from modeling the data for Cu edge of copper doped NC samples shown in Fig. 3.5.

Time-resolved X-ray absorption experiments were performed to construct the excited state XANES spectra of InP:$Cu_4$ NCs. Copper doped InP nanocrystals were optically pumped at 400 nm and were probed at the Cu-K edge. The output of the experiment generates difference absorption spectra (i.e., $Abs_{pump\_on}(\tau) - Abs_{pump\_off}$); data at two time delays are shown in Figure 3.6A. These data were used to construct the excited-state XANES spectrum by adding the difference spectrum to the ground state, whereby the difference spectrum is weighted by a factor ($\omega$=20) that approximately accounts for the excited state population. The result is shown in Figure 3.6B. In the excited state the XANES absorption edge is blue-shifted, which is due to copper dopant oxidation that occurs when InP excitonic holes localize on them.[128] These data are consistent with our previous TR-XAS study on CdS:$Cu_4$ NCs, as well as many other previous investigations.

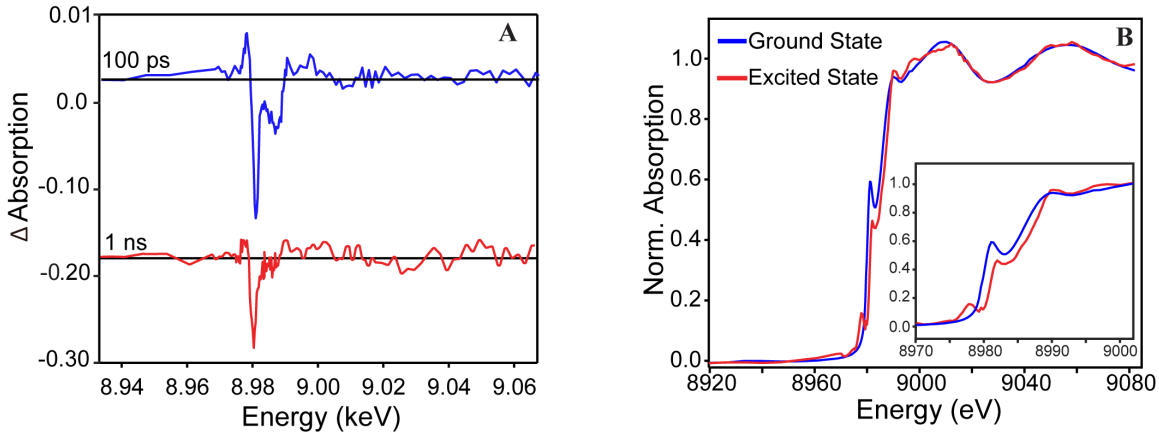


**Figure 3.6.** (A) Time-resolved X-ray absorption difference spectra of InP:$Cu_4$ NCs in the Cu-K edge region. (B) Time resolved XAS spectra of the ground and excited states of copper in InP NCs. Inset: Closeup of the XANES region reveals a feature at 8978 eV.

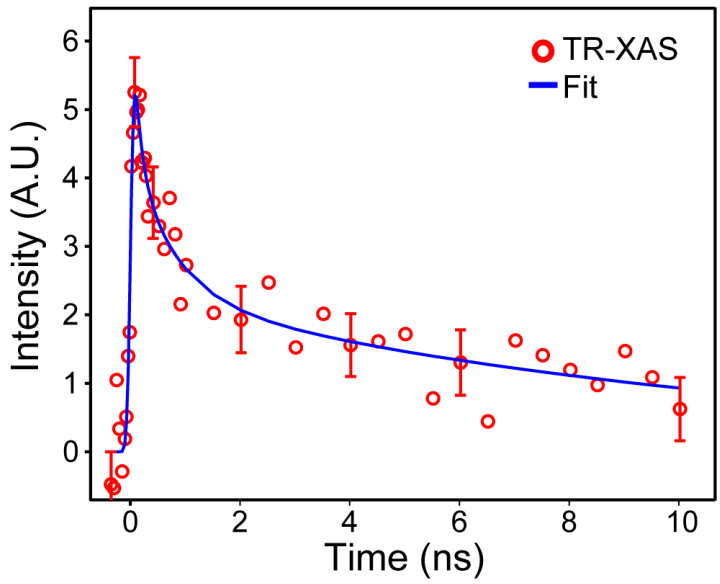


**Figure 3.7.** Copper oxidation kinetics as measured by the intensity of the bleach of the difference spectra at 8980.6 eV. Error bars represent standard deviations of the mean; note that a few representatives are provided for clarity.

The dopant relaxation dynamics of NCs was characterized by monitoring the dopant oxidation signal at 8980.6 eV. A multiexponential fit to the kinetics of dopant oxidation shown in Figure 3.7 yielded three decay components with lifetimes of 0.12 ± 0.15 ns, 0.8 ± 1.4 ns, and 10 ± 30 ns. Given that there must be a population of both interior and surface-doped copper species, the fast timescale component is likely due to fluorescent-quenching recombination of electrons with oxidized surface-bound copper. The later nanosecond components are more difficult to phenomenologically assign, as recombination dynamics of interior-bound copper holes with excitonic electrons would result in red-visible emission.[177-178] However, there is no emission from InP:$Cu_4$ samples. Furthermore, long lifetime emission components on the order of 500 to 1000 ns have been observed from similar copper-doped semiconductor nanomaterials.[177] Here no such dynamic was observed, which is consistent with the lack of visible emission. As a result,

the ~1 ns and 10 ns lifetime components are likely due to surface trap and defect state electrons (perhaps from vacancies) recombining with interior-doped oxidized copper. Overall, this demonstrates the ability to characterize the dynamics of copper dopants in a non-photoluminescent system.

### 3.3.3 DFT models.

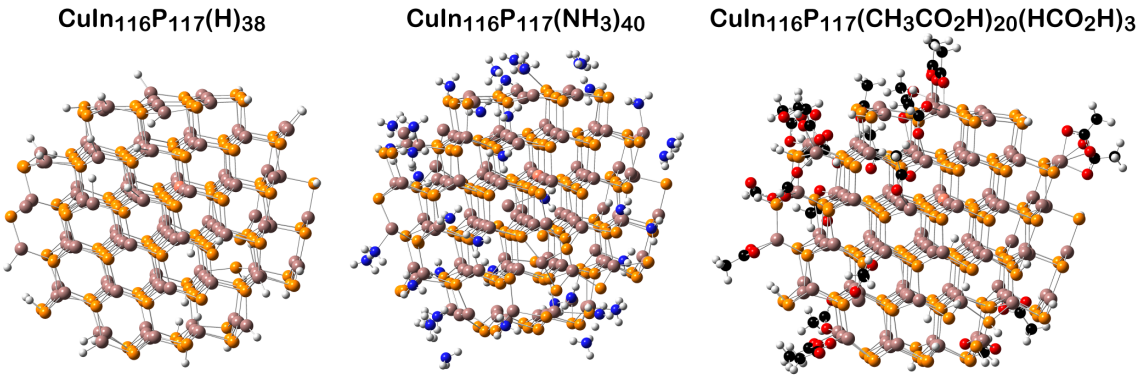


**Figure 3.8.** DFT analyses of hydride, amine, and carboxylic acid coated ~2.1 nm InP clusters ultimately proved inconclusive due to the presence of surface states, even with as many as 40 ligands passivating various surface sites.

In our previous TR-XAS study on doped CdS:$Cu_4$ NCs, DFT and TD-DFT calculations were used to confirm the localization of holes on the Cu dopant and to further investigate the roles of surface-bound species. As discussed in chapter two, this earlier investigation, revealed that the bonding of the Cu dopant is modulated when the NC hole is localized on the guest ion site. Specifically, the number of Cu-S bonds increased due to copper oxidation, which was interpreted as the guest ion attempting to regain electron density from anionic nearest neighbors. These findings were supported by

EXAFS analysis that revealed a shortening of the Cu-S bond distances in the excited state. To investigate the same here, we created very large cluster models of Cu-doped InP, $CuIn_{116}P_{117}$(ligands) (~2.1 nm diameter), with accompanying ligands of hydride as discussed earlier in Chapter 2, carboxylic acids ($CH_3CO_2H$ with additional $HCO_2H$), and amines ($NH_3$). Overall, model building in this system proved to be difficult and the results are inconclusive.

Initially, the overly simplistic hydride terminated model reported previously was enhanced by coordinating carboxylic acids to the surface following the paradigm for ligating CdSe developed by del Ben et al.,[121] whereby only surface atoms with two internal bonds are passivated. Specifically, the conjugate base $CH_3COO^-$ was coordinated to cationic sites while $H^+$ passivated the anions. After several months of optimization, it was found that the triplet state is lower in energy than the singlet. This seemed at odds with the reported ability of doped, passivated InP to fluoresce,[178] which prompted the inclusion of additional ligand surface passivation. After reoptimization the singlet became the ground state, although TDDFT calculations stipulated that the emission was anomalously low. Investigating the density of states revealed that an empty midgap energy level was present, which was identified as a surface state by visualizing the LUMO. Passivation of this state's surface atoms using even more ligands, here $(HCO_2H)_3$, removed it from the bandgap, but caused the triplet to become the ground state again. At this point, carboxylic acid coated was abandoned, in favor of an amine-terminated model shown in Figure 3.8.

The optimization of the amine terminated cluster was extremely time consuming and resulted in significant surface reconstruction. And while the model was found to be

ground state singlet with no midgap states, NBO analysis of the density demonstrated that copper is not oxidized in the excited state. This was true even when optimizing the structure of the first excited triplet state. Furthermore, it was found that the changes in electron density from the ground and excited state were localized on surface atoms as shown in the natural transition orbitals Figure 3.9A. The likely culprits are the lack of adequate surface passivation and the shift in the overall potentials of the valence and conduction bands shown in Figure 3.9B, as amine termination resulted in higher orbital potentials. As the lack of oxidation of the dopant is at odds with the experimental data, it appears that the model is deficient in some manner.

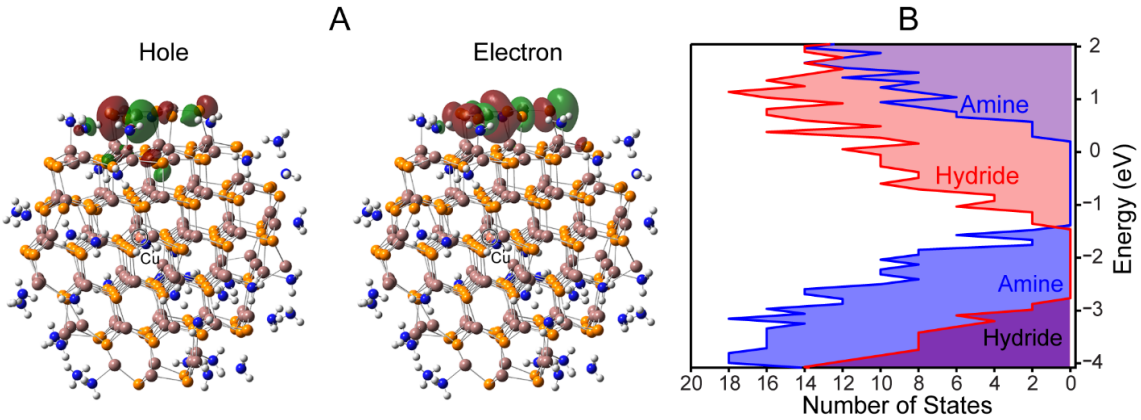


**Figure 3.9.** (A) Natural Transition Orbitals of the hole and electron in the 1st excited state of the amine-coated InP cluster are localized around surface atoms. (B) The density of states of the amine-coated $CuIn_{116}P_{117}(NH_3)_{40}$ cluster is displaced to higher energy compared to the $CuIn_{116}P_{117}(H)_{38}$ system. Amine coverage also slightly lowers the TDDFT calculated bandgap.

Clearly a greater number of surface sites require passivation in Cu-doped InP compared to our models of II-VI semiconductors. This is consistent with recent reports by Cossairt and co-workers,[166,179] who found that magic sized clusters of InP have a significantly enhanced ligand density compared to CdSe. It could also be true that the dopants reside in interstitial sites, as has been suggested in copper doped bulk InP[180] and in InAs QDs.[181] As such, DFT analyses require greatly increasing the surface ligand density and exploration of many copper sites than reported here, and we are currently studying the problem.

Although the DFT results proved inconclusive, there were observations that can be of use towards understanding the system. For example, the ligand dependence of the InP orbital energies suggests the potential for bandgap engineering of devices and the ability to shift less environmentally-sensitive dopant states into or out of the bandgap with cap exchange. Another interesting observation was the phenomenon of self-compensation in the carboxylic acid coated doped InP clusters. In this regard, a surface indium atom extrudes from the cluster surface by ~1.4 Å, regardless of the degree of ligand coverage. It is well-known that such a loss of a cationic site creates an acceptor-like defect state, which then in turn alters the electronic structure in the excited state.[182] In this system, the extruded indium atom was significantly oxidized in place of the interior copper in the excited state.

## 3.4 Conclusion.

We have demonstrated that the cluster seed doping approach was successful in preparing stable Cu-doped InP. Time-resolved XAS studies of the charge carrier dynamics clarified their fundamental optical and electronic properties. These experiments revealed that copper captures a hole in the photoexcited InP. The recombination dynamics are much faster than observed in fluorescent Cu-doped semiconductor NC; however, this is actually sensible given the lack of fluorescence in these materials. As such, our method of using TR-XAS is the only way to observe these dynamics. This report represents the first investigations of the dynamics of doped III-V semiconductor nanocrystals, which we hope will lay the groundwork for future investigations.

# 4 Anomalous Perturbation of $O_2$ Sensitivity of Poly(aromatic) Hydrocarbon by Magnetic Quantum Dots

The content of this chapter has been published as "Anomalus Peretubation of $O_2$ Sensitivity of Poly(aromatic) Hydrocarbon by Magnetic Quantum Dots", A. Hassan, A. Shamirian, X. Zhang, P. T. Snee, *Journal of Physical Chemistry C,* **2017**, 121 (7), 4060-4065. Reproduced with permission from the American Chemical Society.

## 4.1 Introduction

In the previous chapters, we investigated the electronic structure of doped semiconductor nanocrystals and we discussed how incorporation of dopants is a powerful method to control and introduce new functions to QDs. Therefore, in this chapter, we sought to demonstrate a unique application of doped NCs, which eventually led to the discovery of an unusual observation made with a ratiometric QD-based oxygen sensor and resulted in new applications. The quantification of oxygen levels is important in variety of fields such as clinical and environmental analysis.[183] Therefore, many examples of fluorescent $O_2$ sensors have been reported that function via the quenching of the lowest electronically excited singlet and triplet states of various luminophores by ground state molecular oxygen.[184] Several groups have incorporated fluorescent quantum dots for oxygen sensing applications due to their unique optical properties, such as narrow and tunable emission, high quantum yield, and resistance to photobleaching, as discussed in Chapter 1.[185,186] However, high quality NCs are almost universally prepared with an inorganic shell to passivate their surfaces.[187,188] As a result, NCs are intrinsically insensitive to their environment. A solution is to conjugate the NCs to small analyte-sensitive chromophores to create dual-emissive systems that ratiometrically report

analyte concentration. In the case of $O_2$ sensing, there are many examples of oxygen-sensitive dye-NC coupled chromophores.[189-194] Fluorescent functionalized poly(aromatic) hydrocarbons (PAHs), such as pyrene and perylene, are highly suitable for use in this regard as long as they can be derivatized for conjugation to colloidal nanocrystals.

Our group has recently reported a NC-based ratiometric fluorescent $O_2$ sensor that was successfully applied for analysis in live cells.[191] During these investigations, several combinations of $O_2$-sensitive chromophores coupled to a variety of water-soluble quantum dots were prepared and examined. To our surprise, the use of a magnetic nanomaterial rendered the organic components' emissions to be invariant with respect to the oxygen levels. This report describes the discovery of this effect and probes the nature of the dye-NC interactions that are potentially responsible, as well as how such $O_2$-insensitivity may be harnessed for analytical applications.

## 4.2 Experimental.

### 4.2.1 Materials.

All chemicals are used as received unless noted. Triphenylphosphine (99%) was purchased from Alfa Aesar. Poly(ethylene glycol) (MW: 600) was purchased from Fluka. Technical grade 1-octadecene (90%), bis-trimethylsilyl sulfide (purum, >98%), 1-pyrenebutyric acid N-hydroxysuccinimide ester (95%), manganese chloride (>99%), sodium hydroxide (97%), and triethylamine (>99.5%) were purchased from Sigma-Aldrich. Zinc acetate (99%) and n-decylamine (99%) were purchased from Acros. Stearic

acid (≥97%) was purchased from Fluka. Diethylzinc (95%) was purchased from Strem. 1-Ethyl-3-(3-dimethylaminopropyl)carbodiimide (EDC) was purchased from Advanced ChemTech. L-lysine was purchased from Chem-Impex. Benzotriazole-1-yl-oxy-tris-(dimethylamino)-phosphonium hexafluorophosphate (BOP) was purchased from Nova Biochem. Heterobifunctional $N_3$-PEG-$NH_2$ was prepared by the protocol of ref. 195. Common solvents were purchased from Fisher. Poly (ethylene glycol) carbodiimide was prepared according to ref. 63. Manganese stearate was prepared according to ref. 196.

### 4.2.2 Synthesis of Amino PEG- functionalized 1-pyrenebutyric acid and perylene.

Scheme 4.1 outlines the following procedure to prepare a conjugatable, water-soluble pyrene derivative. Approximately 7 mL of DMF was used to dissolve 0.25 g 1-pyrenebutyric acid N-hydroxysuccinimide ester (0.65 mmol) with 0.404 g $N_3$-PEG-$NH_2$ (0.65 mmol). The solution was stirred under a $N_2$ atmosphere. The next day, the solvent was removed under vacuum. The resulting solid was purified by flash chromatography over silica using a mobile phase of dichloromethane. The purified precursor was dissolved in 10 mL of THF into which 0.163 g triphenylphosphine (0.62 mmol) was added. After 4 hr stirring at room temperature, ~0.5 g water was added and the solution was stirred for another 12 hr. The next day, the solvent was removed under vacuum, and ~5 mL water was added. To purify the final product, the solution was acidified using HCl in a separatory funnel. Three portions of 50 mL methylene chloride were added to extract the byproducts. The product in the collected organic portion was extracted with ~100 mL 0.1 M HCl solution. After neutralization with diluted NaOH, the product was extracted back into methylene chloride and dried. Flash chromatography was used to purify the

product using methylene chloride (95% v/v) with 5% dry, distilled methanol over alumina. The purified product is a brown-yellow viscous solid (yield: 56%) and emits a very bright blue light under a UV lamp. NMR and optical characterizations are provided in Figures 4.1 and 4.2, respectively. The perylene dye derivative was prepared exactly as reported in ref. 191.

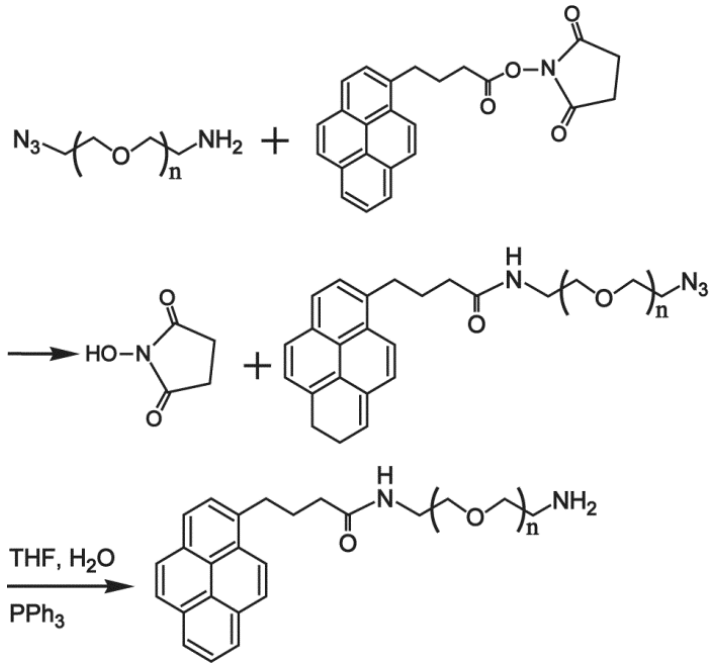


**Scheme 4.1:** The preparation of aminoPEG-functionalized 1-pyrenebutyric acid.

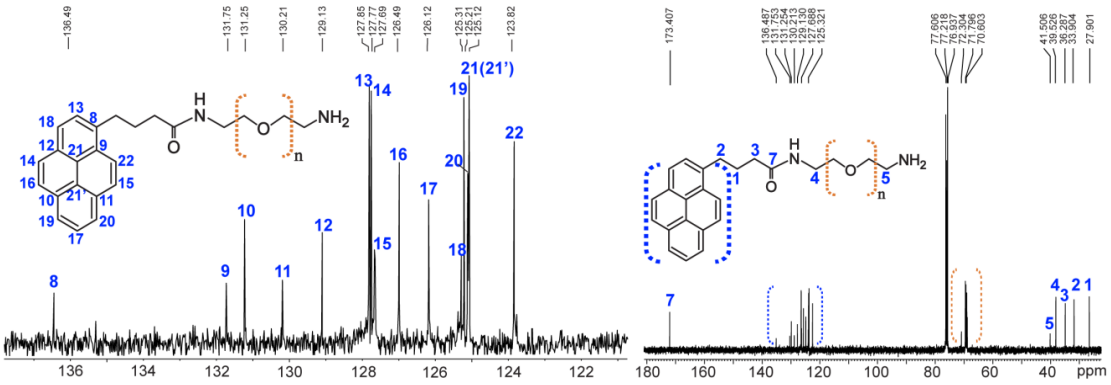

**Figure 4.1:** $^{13}C$ NMR spectrum of aminoPEG-functionalized 1-pyrenebutyric acid; assignments are enumerated.

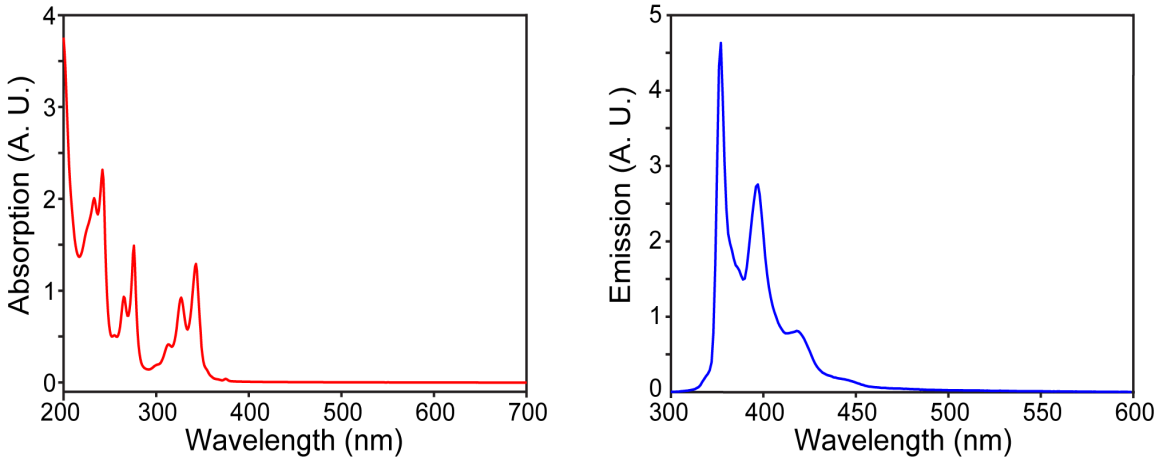


**Figure 4.2.** Absorption and emission of aminoPEG-functionalized 1-pyrenebutyric acid.

### 4.2.3 Dipyrene ligand synthesis.

Scheme 4.2 outlines the following procedure. Approximately 0.25 g 1-pyrenebutyric acid N-hydroxysuccinimide (0.65 mmol) and 0.05 g L-lysine monohydrochloride (0.274 mmol) were added in to ~15 mL DMF. Next, 0.0277 g triethylamine (0.27 mmol) was dripped in and stirred overnight. The next day the DMF was removed under vacuum. The product was dissolved in basic water and washed with dichloromethane to remove by-products. After neutralization of the basic water with dilute HCl, the product was extracted back in dichloromethane, which was then removed under low pressure. A silica column was constructed using 5% (v/v) MeOH in $CH_2Cl_2$ as the mobile phase. Several bands were isolated, and NMR was used to identify the correct product. The $^{13}C$ NMR spectrum for final product is shown in Figure 4.3 below.

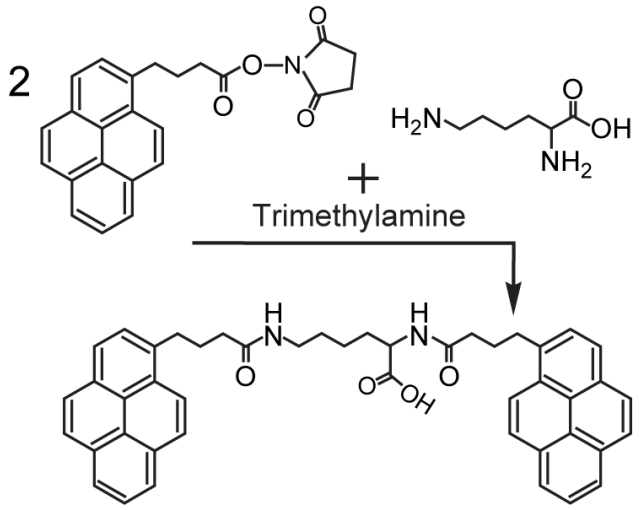


**Scheme 4.2.** The preparation of di-pyrene ligands conjoined by L-lysine.

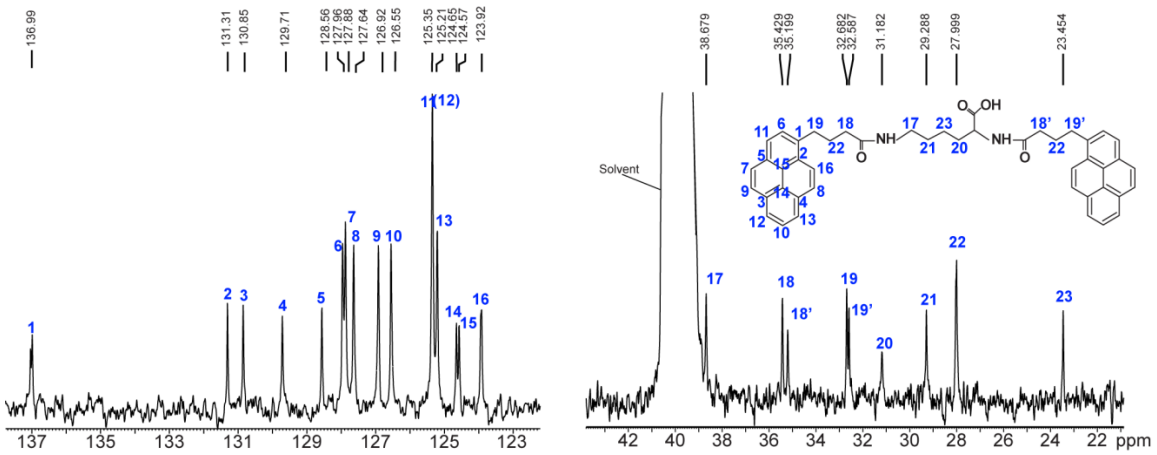


**Figure 4.3.** $^{13}$C NMR spectrum for a di-pyrene ligand conjoined by L-lysine in the aliphatic and aromatic regions with assignments enumerated.

### 4.2.4 Synthesis of CdSe/CdZnS, ZnSe/ZnMnS/ZnS, and ZnSe/ZnS/ZnS NCs.

All procedures to produce CdSe/CdZnS dots can be found in the supporting information of ref. 59. The synthesis of ZnSe/ZnMnS/ZnS is described in ref. 197. ZnSe/ZnS/ZnS NCs were prepared by the same protocol; however, no manganese precursors were added in the 1$^{st}$ shell growth, the absence of which was accounted for by additional zinc precursors.

### 4.2.5 Synthesis of CdSe Core / Magnetically Doped Shell NCs.

Core CdSe NCs were synthesized based on a previously published procedure.[59] CdSe/CdMnS NCs were prepared according to the report of Chen et al.[198] with the addition of manganese stearate during the shell growth process. The synthesis of CdSe/CdMnZnS was used in this study and is reported here. To overcoat the core with a magnetic shell, a solution of 3.383 g distilled trioctylphosphine oxide, 3.4 mL

trioctylphosphine, 25 mg cadmium acetate dihydrate (0.108 mmol) and 0.5 g tetradecylphosphonic acid (1.8 mmol) were added to a 4-neck 100 mL round bottom flask. The solution was degassed at ~100 °C, heated to 250 °C under $N_2$, cooled back ~100 °C, and degassed again. A portion of the core dots were purified with precipitation and dissolved in hexane, which was added with a small (10% relative to Zn) level of manganese stearate to the overcoating solution at ~80 °C and degassed. Next 2.8 mL decylamine was added under a strong flow of $N_2$ and the solution was allowed to stir for ~ 2 hours at 80 °C. Next, the temperature was raised to 220 °C after which two solutions of 15 mg diethyl zinc (0.122 mmol) and 35 mg bis-trimethylsilyl sulfide (0.196 mmol), each dissolved in 3 mL TOP, were separately injected over the course of 2 hours. All precursor quantities were calculated to achieve a 5 monolayer coverage for the quantity of core NCs being coated.

### 4.2.6 Protein Sensing with Dipyrene-CdSe/ZnS QDs.

A practical utility for the lack of $O_2$ sensitivity of PAH-magnetic NC coupled chromophore is demonstrated here. Recently, we reported a motif for creating protein ratiometric sensors by conjugating a protein antigen, a dye, and a NC in a three-spoke wheel structure.[199] As pyrene is an environmentally-sensitive chromophore, the perturbation in a pyrene-NC emitter by nonspecific interactions with bovine serum albumin (BSA) was examined. As this motif requires a modest dye:NC ratio, a dipyrene ligand was synthesized to assure that visible excimer emission was observed at all dye loading levels. A small quantity of the dipyrene ligand was conjugated to ethylene diamine using BOP, and then to aqueous carboxy-terminated PEG-DHLA[200] coated

CdSe/ZnS QDs using standard EDC / NHS coupling protocols. The response of the coupled chromophores was then measured as a function of the addition of BSA. The use of a similar system for cancer screening would be problematic as the pyrene would erstwhile respond to both the protein and the changing $O_2$ levels of the cancer microenvironment. Coupling the dye to a magnetic nanomaterial would thus remove this issue.

### 4.2.7 Nanocrystal functionalization.

The aminoPEG-functionalized 1-pyrenebutyric acid dye was conjugated to NCs with poly(ethylene glycol) carbodiimide using protocol discussed in ref. 63. Typical concentrations of CdSe/CdZnS NCs were 0.1 mM with 2-3 decades excess aminoPEG-functionalized pyrene and activator. Unconjugated pyrene dye was removed with Millipore concentrating filters (100 kDa MWCO) using basic (0.1 M NaOH) water; typical conjugation yields were 10% → 20%.

### 4.2.8 Characterization.

UV/Vis absorbance spectra were taken using a Varian Cary 300 Bio UV/Vis spectrophotometer. Fluorescence emission spectra were taken using a customized Fluorolog (HORIBA Jobin Yvon) modular spectrofluorometer. An EPR spectrum was measured with a Varian E-109E spectrometer. Time resolved emission and dynamics were measured using a home-built system consisting of a NL-100 Nitrogen laser excitation source to produce emission that was fed into a Jarrell Ash monochromator, the output of which was measured by an Applied Photophysics PMT coupled to a Tektronix

tds5104b digital phosphor oscilloscope (1GHz). The PMT was powered by a FLUKE 412B high voltage power supply.

When measuring emission, the absorbance of all solutions was kept near or below 0.1 OD at the excited wavelength to avoid inner-filtering effects. Excitation was set between 335 nm to 360 nm to co-excite the pyrene and NCs simultaneously and 420 nm for perylene-NC conjugates.

### 4.2.9 Molecular Dynamics Simulations.

To determine the effect of a magnetic field on the dynamics of $O_2$, a molecular dynamics simulation was performed using 2000 SPC/E water molecules[201] surrounding a $Zn_{138}S_{138}$ nanoparticle. The coordinates of the cluster were taken from the optimized geometry of a $Cd_{138}S_{138}(H_2CO_2)_{24}$ quantum dot using DFT with the PBE1/PBE hybrid functional[115,116] and the SBJKC basis set and effective core potentials.[202] This model was chosen due to the fact that a CdZnS shell on a CdSe particle grows quasi-epitaxially,[203] and thus the crystal parameters for CdS are an appropriate representation. The Lennard-Jones (LJ) parameters for ZnS were taken from ref. 204, charges from ref. 205, while the $O_2$ LJ parameters were from ref. 206. Full Ewald sums were used for the long-range electrostatic interactions. The calculations were performed using in-house software, which was verified to perform correctly by testing the properties of SPC/E water to demonstrate that correct dynamical averages were obtained (diffusion constant, enthalpy of vaporization, etc.). The system was equilibrated for ~100 ps, after which a trajectory of 140 ps was performed to characterize the average force on the $O_2$ molecule. Next, the trajectory was reinitiated from the beginning with an additional magnetic force on one of

the $O_2$ atoms towards the nearest Zn center. The net force was simulated to be the maximum aligned magnetic dipoles. There were no discernible differences in the dynamics after 40 ps. The magnitude of the force was arbitrarily multiplied by 10× to represent the presence of more Mn centers, yet the $O_2$ trajectory with and without this force was essentially identical.

## 4.3 Results & Discussion.

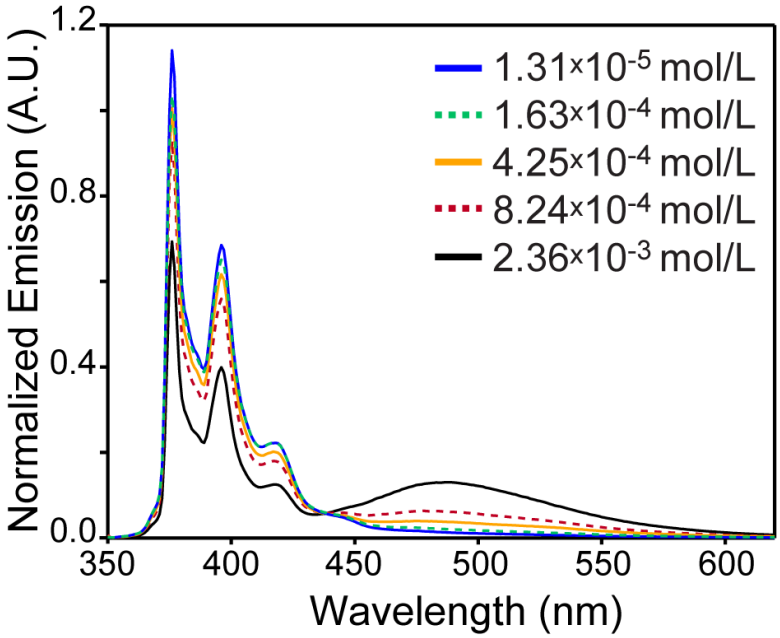


**Figure 4.4:** Normalized emission from aminoPEG-functionalized pyrene in water demonstrates concentration-dependent excimer emission.

This study began by sensibly constructing dual-emitting chromophore systems where one component is responsive to oxygen while another functions as a reference, here a nanocrystal. Several $O_2$-sensitive chromophores exist that are efficiently quenched by molecular oxygen. Among these, poly(aromatic) hydrocarbons are often employed as

they have interesting and complex luminescent features. For example, pyrene emits with sharp fluorescence bands in the UV−blue-visible (~320 nm−450 nm) in addition to a broad and structureless feature in the blue-green region (~400−550 nm) that appears at higher concentrations (Figure 4.4). The latter can also be observed by conjugating multiple copies of the dye to a singular nanostructure to create a high local concentration (Figure 4.5). This low energy feature is due to excimer emission from an excited singlet state pyrene−ground state pyrene dimer.

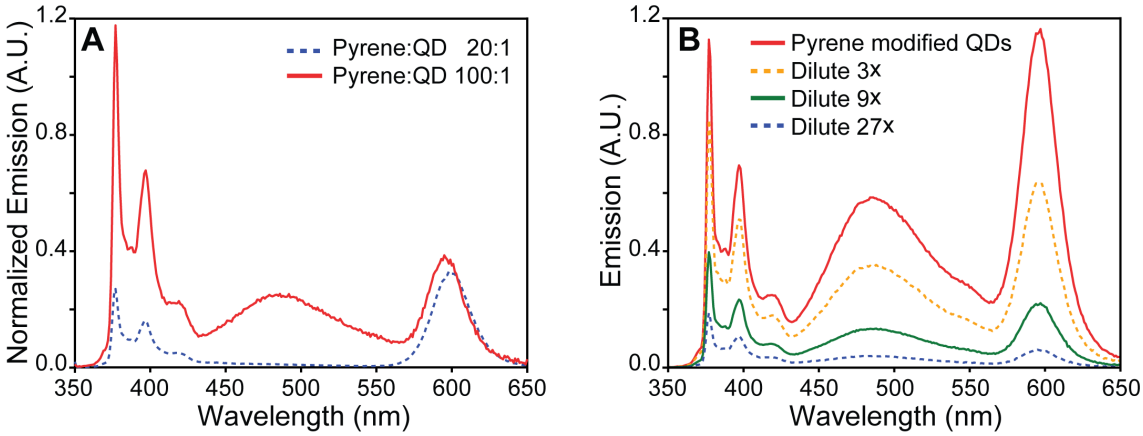


**Figure 4.5:** (A) A 20:1 pyrene-NC coupled chromophore does not have a high enough dye loading ratio to result in excimer emission, which is observed in the 100:1 conjugate. Spectra have been normalized to the NC signal at 595 nm after subtracting pyrene's excimer component. (B) Emission spectra of pyrene-NC coupled chromophore as a function of dilution demonstrate that excimer emission is present far below ~1000×, which is the critical micelle concentration of aminoPEG-functionalized pyrene (~1.6 × $10^{-4}$ M).

Further complicating matters is the phenomenon of delayed fluorescence, which is the result of triplet−triplet annihilation.[207] This process occurs due to energy transfer between two interacting excited triplet state molecules to produce a dimer in the excited singlet excimer state. This results in the observation of excimer emission over a long, triplet-lifetime time scale which is the delayed fluorescence process. These dynamics are outlined in Figure 4.6, which represents the interconnections between the excited singlet S* (blue), excimer S2* (green), and triplet T (red) states that create the rich emission spectra shown in Figure 4.5.

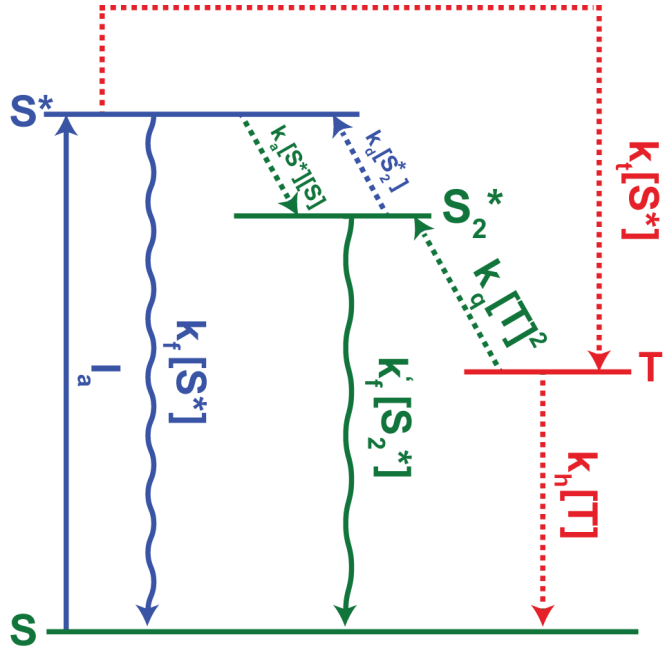


**Figure 4.6:** Jablonski diagram illustrating normal and delayed fluorescence of pyrene, adapted from ref. 207. The following symbologies are used: $I_a$, excitation rate; $k_f$ and $k'_f$, radiative singlet monomer and dimer relaxation rates, respectively (the nonradiative pathways are not represented for clarity); $k_q$, bimolecular triplet− triplet quenching rate; $k_t$, intersystem crossing rate; $k_h$, nonradiative triplet relaxation rate; $k_a$, bimolecular singlet association rate; $k_d$, excited singlet dimer dissociation rate.

One system that was explored initially is in essence a water soluble version of the oxygen-sensitive probe reported by Amelia et al.[190] A poly(ethylene glycol)-pyrene chromophore was prepared by conjugating 1-pyrenebutyric acid to a heterobifunctional PEG linker. The first studies were conducted by coupling this dye to polymer-encapsulated CdSe/CdZnS NCs as the photophysical behavior of these nanomaterials is well established. Upward of ~100 pyrene chromophores were conjugated per NC using high-yielding protocols.[63,64] As shown in Figure 4.5A, the emission of a chromophore with a low pyrene:NC ratio (~20) displays a NC feature at the semiconductor band gap at ~595 nm and sharp pyrene breathing modes from 350 to 450 nm. When the pyrene:NC ratio was increased to ~100:1, the broad excimer emission centered at ~480 nm forms due to the dimerization of the dye on the NC surface.[208] This is evident from the fact that excimer emission is observed regardless of how much the coupled chromophores are diluted, as shown above in Figure 4.5B.

The sensitivity of the coupled pyrene−NC conjugates toward oxygen was measured. The sample was sparged with $N_2$ for ~1 h, after which time the cuvette was covered, and the emission was promptly measured. The same protocol was followed after saturating the solution with oxygen. The spectra in Figure 4.7 demonstrate oxygen sensitivity via the quenching of pyrene in the presence of oxygen. Combined with the NC insensitivity toward $O_2$, the result is a self-calibrating signal that can be used to make measurements in a biological milieu, as we recently demonstrated in live HeLa cells using perylene $AgInS_2$/ZnS NC coupled chromophores.[191] As with this previous study, we next sought to use a Cd-free quantum dot component to enhance biological compatibility. To this end

the aminoPEG-functionalized pyrene derivative was conjugated to nontoxic ZnSe/ZnMnS/ZnS QDs.[197] However, the results were inexplicable: there was no response observed to the saturation of $O_2$, as shown in Figure 4.8A.

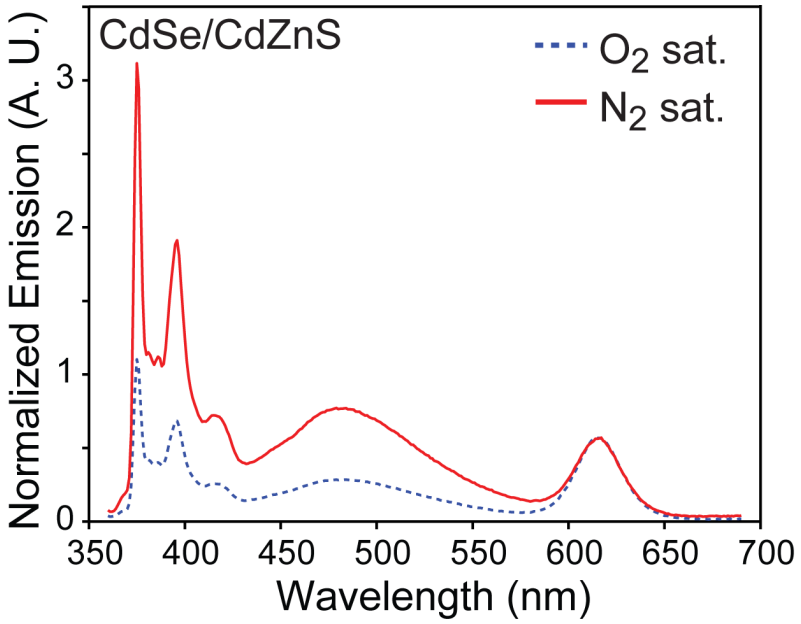


**Figure 4.7:** Emission spectra of pyrene-functionalized CdSe/CdZnS NCs after saturating with $N_2$ and $O_2$ demonstrate ratiometric fluorescent oxygen-sensing capability. Spectra have been normalized to the NC emission intensity.

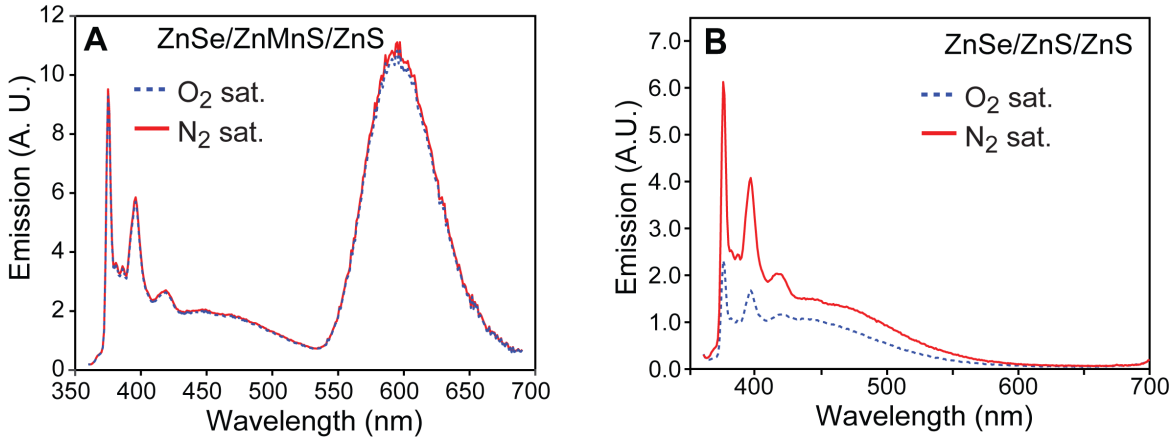


**Figure 4.8:** (A) Emission spectra of pyrene-functionalized ZnSe/ZnMnS/ZnS NCs after saturating with $O_2$ and $N_2$. (B) Emission spectra of pyrene-functionalized ZnSe/ZnS/ZnS NCs display significant fluorescence quenching by $O_2$.

To examine this issue of the nonsensitivity, we studied each component of the pyrene-ZnSe/ZnMnS/ZnS NC construct individually. First, note that the dots are doped with manganese transition-metal ions that act as visible-emitting phosphors. Not only does this alter the NC's optical properties,[196,126,38] the ions are highly magnetic as well. As a result, our hypothesis is that the presence of $Mn^{2+}$ in the shell inhibited pyrene from sensing oxygen via a magnetic interaction. This was explored by synthesizing undoped water-soluble pyrene-ZnSe/ZnS/ZnS NCs. It was found that pyrene is efficiently quenched by oxygen when conjugated to these nonmagnetic dots, which eliminates the possibility of a material dependence beyond the influence of manganese ions; these data are shown in Figure 4.8B. To further verify that $Mn^{2+}$ is the culprit, core/ doped shell Cd-based QDs were prepared, given that no odd behavior was observed previously in pyrene-CdSe/CdZnS dots, as explained above and shown in Figure 4.7.

To this end, several synthetic strategies were examined, beginning with an attempt to prepare CdSe/CdMnS dots via an alteration of the procedure reported by Chen et al.[198] This synthetic protocol is of fundamental interest due to the resulting narrow and symmetric emission spectra, which is unusually good for a core/shell material. Although we were able to reproduce these properties, it was found that doping this system results in fairly low photoluminescence quantum yields. Hence, another protocol was developed to shell-doped CdSe/CdMnZnS dots, which ultimately resulted in magnetic NCs with substantially higher QYs. Electron paramagnetic resonance (Figure 4.9) measurements confirm the presence of $Mn^{2+}$.

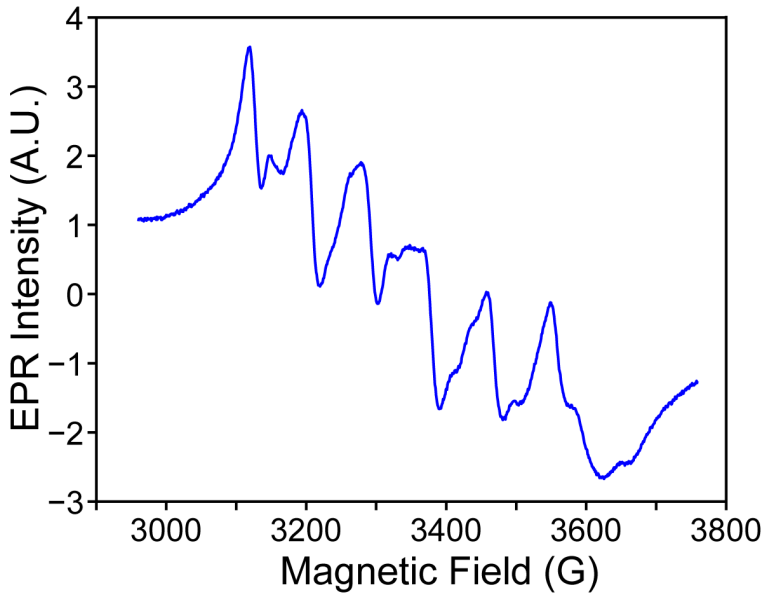


**Figure 4.9:** EPR spectrum of CdSe/CdMnZnS. The spectrum consists of a typical S=5 six-line pattern which confirms that the $Mn^{2+}$ ions are embedded within the nanocrystal.[34,209-211] There are clearly more than one type of overlapping resonance, the width of which is consistent with a high coupling constant (~$90\times10^{-4}$ $cm^{-1}$) that likely originates from octahedral $Mn^{2+}$ bound to the NC surface. A smaller, ~$60\times10^{-4}$ $cm^{-1}$ feature that is more similar to $Mn^{2+}$ embedded within the host, is likely responsible for some of the structure in the spectrum above.

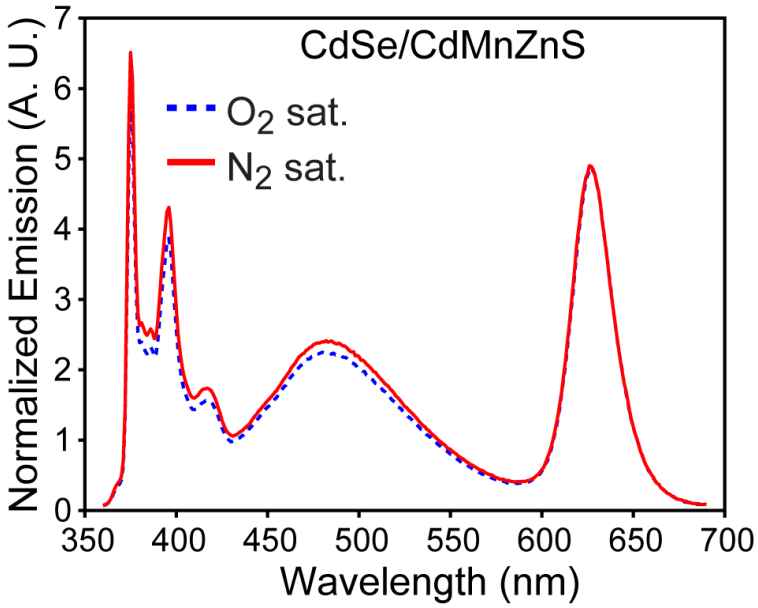


**Figure 4.10:** Emission Spectra of pyrene-functionalized CdSe/CdMnZnS NCs after saturating with $N_2$ and $O_2$. All spectra have been normalized to the NC emission intensity after subtraction of the dye component.

CdSe/CdMnZnS NCs were water-solubilized and functionalized with pyrene. In agreement with our previous results, the organic chromophore minimally responded at best to saturation of the solution with oxygen, as shown in Figure 4.10. Several investigations were conducted to further explore this odd phenomenon. Another functionalized PAH, aminoPEG-functionalized perylene, which was employed in our previous study,[191] was coupled to magnetic CdSe/CdMnZnS NCs. Again, the chromophore was minimally quenched by saturating the solution with oxygen. To verify that the sparging of the dots was not responsible, enzymatic removal of $O_2$ via the oxidation of glucose with glucose oxidase was employed.[191] The same results were obtained: the PAHs do not respond to the presence of oxygen, as shown in Figure 4.11 below. Many of these experiments were repeated; all materials were prepared multiple

times, and in every instance, we find that these nominally $O_2$ sensitive dyes do not respond to oxygen when conjugated to magnetic nanomaterials.

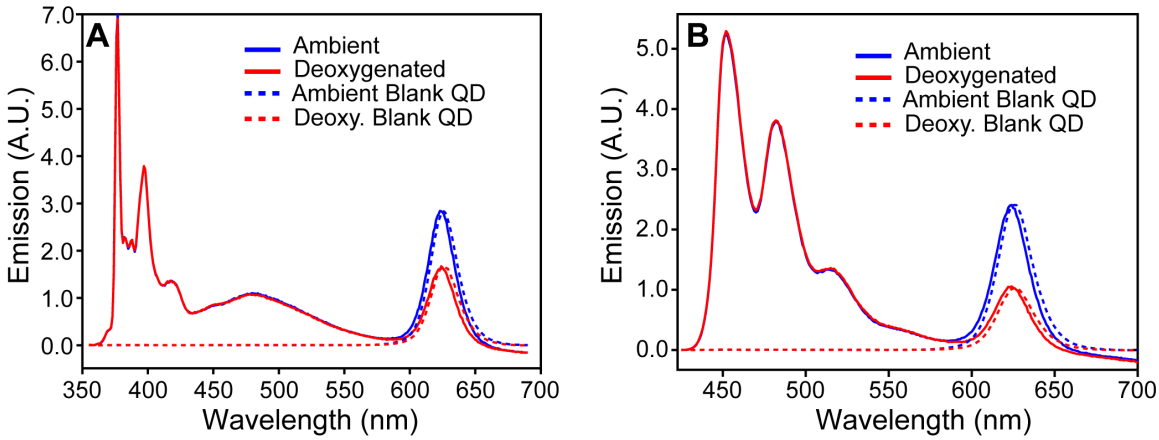


**Figure 4.11**: (A) The emission spectra of blank and pyrene-functionalized CdSe/CdMnZnS NCs after saturation with oxygen scavenging solution. (B) The same of perylene-functionalized CdSe/CdMnZnS NCs. The enzyme-based oxygen scavenging process produces hydrogen peroxide, which is known to quench QDs.[190] This was confirmed by exposing blank NCs to the same conditions. Overall, these results demonstrate that the nominally $O_2$ sensitive dyes is not quenched by oxygen when conjugated to magnetic nanomaterials, which is not the result of an artifact of the $O_2$ removal process.

We next sought to determine a physical reason for this phenomenon. Motivated by the well-known undergraduate demo of the capture of liquid $O_2$ by a magnet, the possibility of physical sequestration of oxygen by magnetic forces was studied by molecular dynamics simulation. A simplistic model was used, where a ZnS cluster with no ligands was equilibrated with a single $O_2$ and 2000 SPC/E water molecules under periodic boundary conditions. An equilibrated trajectory was initiated with and without

the addition of a $\mu(m_{O2}m_{Mn})/r^4$ magnetic force between $O_2$ and a surface Zn atom site chosen to represent $Mn^{2+}$. Although the magnetic dipoles were modeled as perfectly aligned to provide the strongest attractive interaction, it was found that the $O_2$ molecule was not perturbed by a magnetic force. This is sensible, as the average rms force on $O_2$ was found to be ~120 kJ/mol/nm, as shown in Figure 4.12, which is overwhelmingly strong compared to a $2.6 \times 10^{-4}$ kJ/mol/nm force imparted by one $Mn^{2+}$ at a ~1 nm distance. Overall, the lack of oxygen sensitivity is unlikely due to perturbation of $O_2$ diffusion due to magnetic interactions.

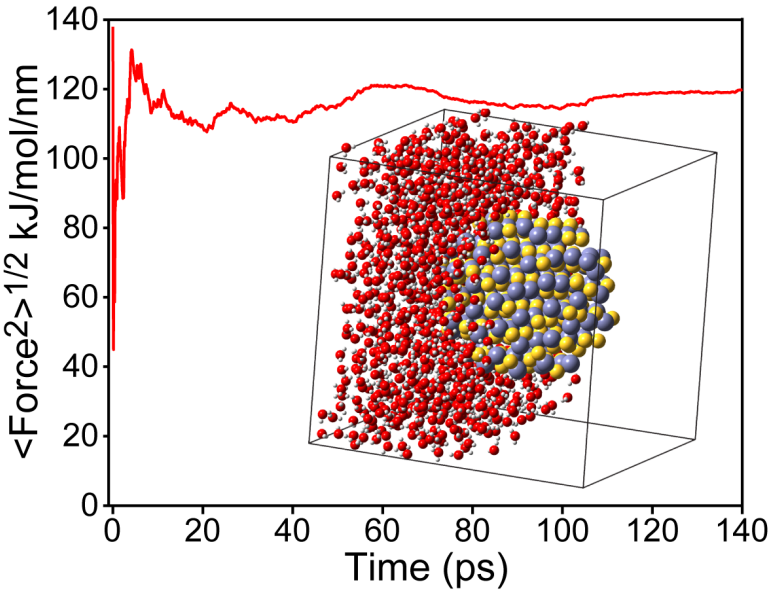


**Figure 4.12:** Running average of the rms force on an oxygen site of the Lennard-Jones $O_2$ molecule in a bath of 2000 SPC/E water molecules surrounding a ZnS nanoparticle. Inset is a cut-away configuration of the system.

Next, pyrene's photophysical properties were examined. First, we verified that the chemical derivatization of pyrene did not alter the excited singlet and triplet energy splitting. Phosphorescence emission of the aminoPEG pyrene was observed at ~600 nm in water, the same as that reported for neat pyrene in an aqueous micelle.[212] Regardless, this is somewhat of a nonissue, as it has already been established that the singlet−triplet excited state energy splitting does not affect the ability of oxygen to quench the fluorescence of a PAH.[213] Next, the quantum yield of the dye was measured to determine whether conjugation to a magnetic QD had an effect, one that overwhelms the quenching of oxygen that might explain the lack of $O_2$ sensitivity. However, as shown in Table 4.1, there is essentially no difference in the dye's brightness due to conjugation to the magnetic quantum dot.

| **Pyrene-NC** | **QY %** |
|---|---|
| Pyrene-CdSe/CdZnS | 67 |
| Pyrene-CdSe/CdMnZnS | 65 |

**Table 4.1:** Fluorescence quantum yield of the dye component of pyrene-NC conjugates were obtained in the absence of $O_2$ (samples were equilibrated under vacuum). The absorbance of all solution was kept below 0.1 OD. Quinine dissolved in 0.5 M $H_2SO_4$ was used as a reference (54.6%).

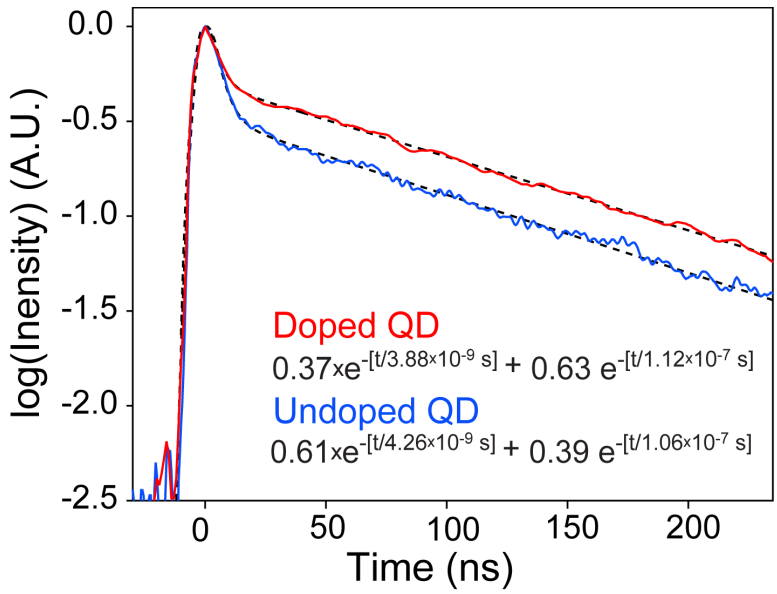


**Figure 4.13:** Time-resolved emission dynamics of pyrene in the excimer region (490 nm) conjugated to CdSe/CdZnS and CdSe/CdMnZnS NCs reveals a higher branching ratio into the delayed fluorescence channel when the dye is attached to magnetic nanomaterials. Dashed lines are fits to the data; errors are on the order of 1%.

Perturbation of the excited state dynamics of the dye was also studied. In this regard, the time-resolved emission spectra of the pyrene-NC in both magnetic and nonmagnetic systems were measured in the excimer region, as shown in Figure 4.13. In both cases, nearly identical ~$10^{-9}$ and ~$10^{-7}$ s biexponential decay patterns are observed, which clearly corresponds to "prompt" and delayed florescence, respectively. However, the branching ratios diverge, whereas the magnetic system has a greater delayed fluorescence dynamical component. This indicates that more pyrene molecules in the singlet state become triplet when conjugated to $Mn^{2+}$ doped QDs, likely due to the mixing of singlet−triplet states in the presence of a magnetic field.[214] This is possible because the excited singlet and triplet states have the proper symmetry to interact via a magnetic

perturbation given the $D_{2h}$ point group of the molecule. The question arises as to whether these differences would account for the observed lack of $O_2$ sensitivity. This is unlikely, as increasing the singlet−triplet splitting would enhance the oxygen sensitivity rather than completely suppress it.[215] To summarize, the time-resolved data demonstrate interesting differences in the dye dynamics, and the results are sensible and expected. The lack of $O_2$ sensitivity is not.

All attempts to derive a physical basis of this phenomenon have not yielded an acceptable explanation. Furthermore, a review of the literature does not help. For example, Tachikawa and Bard reported some suppression of oxygen sensitivity of pyrene in the presence of a magnetic field,[216] although the effect was on the order of a few percent, even at very high field strengths. Several other studies have been performed on the magnetic field dependence of the triplet−triplet annihilation process that yields delayed fluorescence;[217,218] however, there is no mention of oxygen-nonsensitivity in these reports.[215] As such, there must be a disruption of the quenching process that results from both the microenvironment of the NC and a magnetic field component. Specifically, the process of $O_2$-induced excited state dye quenching is due to an exchange interaction[219] which is highly distance- and orientation-dependent.[220] This leads us to propose that the microenvironment of the NC restricts the interaction of the dye and oxygen molecule into orientations that are maximally perturbed by the magnetic field. The inhomogeneity of the magnetic field may also play a role.[221] Unfortunately, we are not aware of an experimental or theoretical method to interrogate such an interaction in a transient species.

## 4.4 Conclusion.

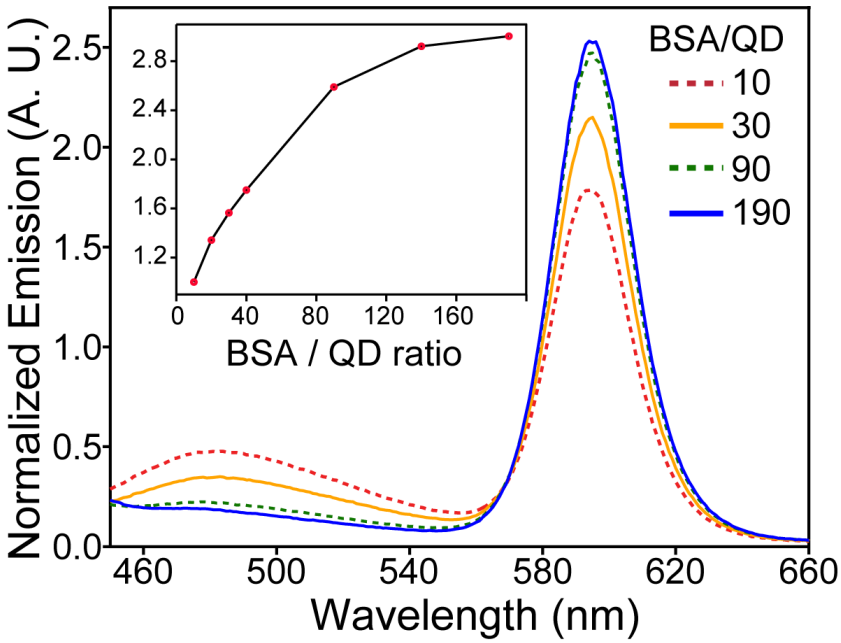


**Figure 4.14:** Titration of a dipyrene-NC conjugate with increasing levels of bovine serum albumin cause a suppression of the dye emission with a concomitant increase in the NC luminescence. Inset: Ratio of the integrated intensities is a calibratable signal for the presence of the protein.

Demonstrated here is a newly discovered phenomenon that offers the ability to modulate the optical properties of organic chromophores using magnetic nanomaterials. Despite the mystery that envelops these observations, the effect of magnetic nanomaterial-induced loss of oxygen sensitivity has potential utility. For example, pyrene is a well-known environmentally sensitive dye, and its use in a dye-NC platform may offer analytical development opportunities. In this regard, we have generated preliminary data that suggest pyrene−NC conjugates may be employed as ratiometric sensors for proteins as shown in Figure 4.14. Analyte selectivity for a protein such as COX-2, which is upregulated in cancer, could be created by synthesizing a three-spoke wheel motif

where pyrene, a COX-2 antigen such as indocin,[222] and a NC are all conjugated together.[199] Thus, it would be advantageous to eliminate the oxygen cross-sensitivity of the dye component as shown here, especially as $O_2$ levels are abnormal in a cancer microenvironment.

# 5 Conclusion

Colloidal semiconductor nanocrystals are emerging as an important class of materials with superior photophysical properties and significant potential for applications in optoelectronic devices. However, their applicability is greatly limited by the low carrier concentration of most intrinsic semiconductor NCs. As a result, dopants must be incorporated into the semiconductor matrix to add (subtract) electrons from the conduction (valence) bands to increase its charge carrier density, and thereby its conductivity. Therefore, part of my research in Snee group focused on elucidating the electronic structure of doped semiconductors where I discovered that that dopants rearrange their bonding environment due to their interaction with charge carriers. This dynamic was revealed using time-resolved X-ray absorption spectroscopy study that demonstrated the generation of an exciton causes one of the charge carriers to be captured by the dopants, which then reconfigures its coordination sphere to gain further electron density from the surrounding host matrix. Essential to the success of this project was our recently developed method to synthesize doped semiconductor NCs using the cluster seed method that allowed for the synthesis of a large quantity of exactly-doped materials, which are necessary substrates to perform these experiments.

The recent development of time-resolved X-ray absorption spectroscopy and the discovery that charge carriers modulate dopant bonding has opened avenues for fundamental research on doped semiconductors. The III-V semiconductor family is very important for many technological applications. As such, I explored the electronic dynamics in doped III-V semiconductor nanocrystals using copper doped InP as the

model system by monitoring the photophysical properties of copper guest ions in the presence of photogenerated charge carriers using time-resolved X-ray absorption spectroscopy. I demonstrated that the dopant interacts with holes, and characterized the kinetics of electron-hole recombination which would be erstwhile impossible in a non-emissive indium phosphide semiconductor system.

The introduction of dopants into semiconductor nanocrystals is an efficient way to manipulate the optical, electronic and magnetic properties of semiconductor NCs. In this vein, I have developed a doping scheme for Cd and Zn-based II-VI NCs with manganese impurities and I reported the discovery of some remarkable effects of the magnetic field on the fluorescence quenching of polycyclic aromatic hydrocarbons by oxygen. The ability to modulate the oxygen quenching efficiency of a chromophore creates an additional parameter space of sensing chromophore design.

## CITED LITERATURE


1. 'Plenty of room'; revisited. *Nature Nanotechnology* **2009,** *4*, 781.
2. Brus, L. E. A simple model for the ionization potential, electron affinity, and aqueous redox potentials of small semiconductor crystallites. *The Journal of Chemical Physics* **1983,** *79*, 5566-5571.
3. Bawendi, M. G.; Steigerwald, M. L.; Brus, L. E. The quantum mechanics of larger semiconductor clusters ("quantum dots"). *Annual Review of Physical Chemistry* **1990,** *41*, 477-496.
4. Colvin, V. L.; Alivisatos, A. P.; Tobin, J. G. Valence-band photoemission from a quantum-dot system. *Physical Review Letters* **1991,** *66*, 2786-2789.
5. Efros, A. L.; Rosen, M. Quantum size level structure of narrow-gap semiconductor nanocrystals: Effect of band coupling. *Physical Review B* **1998,** *58*, 7120-7135.
6. Brus, L. E. Electron–electron and electron-hole interactions in small semiconductor crystallites: The size dependence of the lowest excited electronic state. *The Journal of Chemical Physics* **1984,** *80*, 4403-4409.
7. Rossetti, R.; Brus, L. Electron-hole recombination emission as a probe of surface chemistry in aqueous cadmium sulfide colloids. *The Journal of Physical Chemistry* **1982,** *86*, 4470-4472.
8. Klimov, V. I. Spectral and dynamical properties of multiexcitons in semiconductor nanocrystals. *Annual Review of Physical Chemistry* **2007,** *58*, 635-673.
9. Efros, A. L.; Rosen, M. The electronic structure of semiconductor nanocrystals. *Annual Review of Materials Science* **2000,** *30*, 475-521.
10. Gaponenko, S. V., *Introduction to nanophotonics*. Cambridge University Press: 2010.
11. Henderson, B; Imbusch, G.F. Optical spectroscopy of inorganic solids. *Journal of Modern Optics* **1990,** *37*, 1688-1688.
12. Shim, M.; Guyot-Sionnest, P. N-type colloidal semiconductor nanocrystals. *Nature* **2000,** *407*, 981.
13. Mikulec, F. V.; Kuno, M.; Bennati, M.; Hall, D. A.; Griffin, R. G.; Bawendi, M. G. Organometallic synthesis and spectroscopic characterization of manganese-doped CdSe nanocrystals. *Journal of the American Chemical Society* **2000,** *122*, 2532-2540.
14. p Johnson, N. M.; Ponce, F. A.; Street, R. A.; Nemanich, R. J. Defects in single-crystal silicon induced by hydrogenation. *Physical Review B* **1987,** *35*, 4166-4169.
15. Zhang, S. B.; Wei, S. H.; Zunger, A. Intrinsic n-type versus p-type doping asymmetry and the defect physics of ZnO. *Physical Review B* **2001,** *63*, 075205.
16. Chiang, C. K.; Fincher, C. R.; Park, Y. W.; Heeger, A. J.; Shirakawa, H.; Louis, E. J.; Gau, S. C.; MacDiarmid, A. G. Electrical conductivity in doped polyacetylene. *Physical Review Letters* **1977,** *39*, 1098-1101.
17. Šklovskij, B. I.; Shklovskiĭ, B. I.; Ėfros, A. L., *Electronic properties of doped semiconductors*. Springer London, Limited: 1984.
18. Murray, C. B.; Norris, D. J.; Bawendi, M. G. Synthesis and characterization of nearly monodisperse CdE (E = sulfur, selenium, tellurium) semiconductor nanocrystallites. *Journal of the American Chemical Society* **1993,** *115*, 8706-8715.

19. LaMer, V. K.; Dinegar, R. H. Theory, production and mechanism of formation of monodispersed hydrosols. *Journal of the American Chemical Society* **1950,** *72*, 4847-4854.
20. Rossetti, R.; Nakahara, S.; Brus, L. E. Quantum size effects in the redox potentials, resonance raman spectra, and electronic spectra of CdS crystallites in aqueous solution. *The Journal of Chemical Physics* **1983,** *79*, 1086-1088.
21. Rossetti, R.; Ellison, J. L.; Gibson, J. M.; Brus, L. E. Size effects in the excited electronic states of small colloidal CdS crystallites. *The Journal of Chemical Physics* **1984,** *80*, 4464-4469.
22. Rossetti, R.; Hull, R.; Gibson, J. M.; Brus, L. E. Excited electronic states and optical spectra of ZnS and CdS crystallites in the ≅15 to 50 Å size range: Evolution from molecular to bulk semiconducting properties. *The Journal of Chemical Physics* **1985,** *82*, 552-559.
23. Katari, J. E. B.; Colvin, V. L.; Alivisatos, A. P. X-ray photoelectron spectroscopy of CdSe nanocrystals with applications to studies of the nanocrystal surface. *The Journal of Physical Chemistry* **1994,** *98*, 4109-4117.
24. Peng, X.; Wickham, J.; Alivisatos, A. P. Kinetics of II-VI and III-V colloidal semiconductor nanocrystal growth: "Focusing" of size distributions. *Journal of the American Chemical Society* **1998,** *120*, 5343-5344.
25. Jun, Y.-w.; Lee, S.-M.; Kang, N.-J.; Cheon, J. Controlled synthesis of multi-armed cds nanorod architectures using monosurfactant system. *Journal of the American Chemical Society* **2001,** *123*, 5150-5151.
26. Malik, M. A.; Revaprasadu, N.; O'Brien, P. Air-stable single-source precursors for the synthesis of chalcogenide semiconductor nanoparticles. *Chemistry of Materials* **2001,** *13*, 913-920.
27. Cumberland, S. L.; Hanif, K. M.; Javier, A.; Khitrov, G. A.; Strouse, G. F.; Woessner, S. M.; Yun, C. S. Inorganic clusters as single-source precursors for preparation of CdSe, ZnSe, and CdSe/ZnS nanomaterials. *Chemistry of Materials* **2002,** *14*, 1576-1584.
28. Bawendi, M. G.; Carroll, P. J.; Wilson, W. L.; Brus, L. E. Luminescence properties of CdSe quantum crystallites: Resonance between interior and surface localized states. *The Journal of Chemical Physics* **1992,** *96*, 946-954.
29. Nirmal, M.; Murray, C. B.; Bawendi, M. G. Fluorescence-line narrowing in CdSe quantum dots: Surface localization of the photogenerated exciton. *Physical Review B* **1994,** *50*, 2293-2300.
30. Guyot-Sionnest, P.; Shim, M.; Matranga, C.; Hines, M. Intraband relaxation in CdSe quantum dots. *Physical Review B* **1999,** *60*, R2181-R2184.
31. Dabbousi, B. O.; Rodriguez-Viejo, J.; Mikulec, F. V.; Heine, J. R.; Mattoussi, H.; Ober, R.; Jensen, K. F.; Bawendi, M. G. (CdSe)ZnS core−shell quantum dots: Synthesis and characterization of a size series of highly luminescent nanocrystallites. *The Journal of Physical Chemistry B* **1997,** *101*, 9463-9475.
32. Hines, M. A.; Guyot-Sionnest, P. Synthesis and characterization of strongly luminescing ZnS-capped CdSe nanocrystals. *The Journal of Physical Chemistry* **1996,** *100*, 468-471.

33. Peng, X.; Schlamp, M. C.; Kadavanich, A. V.; Alivisatos, A. P. Epitaxial growth of highly luminescent CdSe/CdS core/shell nanocrystals with photostability and electronic accessibility. *Journal of the American Chemical Society* **1997,** *119*, 7019-7029.
34. Norris, D. J.; Yao, N.; Charnock, F. T.; Kennedy, T. A. High-quality manganese-doped ZnSe nanocrystals. *Nano Letters* **2001,** *1*, 3-7.
35. Erwin, S. C.; Zu, L.; Haftel, M. I.; Efros, A. L.; Kennedy, T. A.; Norris, D. J. Doping semiconductor nanocrystals. *Nature* **2005,** *436*, 91-94.
36. Meulenberg, R. W.; van Buuren, T.; Hanif, K. M.; Willey, T. M.; Strouse, G. F.; Terminello, L. J. Structure and composition of Cu-doped CdSe nanocrystals using soft X-ray absorption spectroscopy. *Nano Letters* **2004,** *4*, 2277-2285.
37. Srivastava, B. B.; Jana, S.; Pradhan, N. Doping Cu in semiconductor nanocrystals: Some old and some new physical insights. *Journal of the American Chemical Society* **2011,** *133*, 1007-1015.
38. Beaulac, R.; Schneider, L.; Archer, P. I.; Bacher, G.; Gamelin, D. R. Light-induced spontaneous magnetization in doped colloidal quantum dots. *Science* **2009,** *325*, 973-976.
39. Shim, M.; Wang, C.; Norris, D. J.; Guyot-Sionnest, P. Doping and charging in colloidal semiconductor nanocrystals. *MRS Bulletin* **2012,** *26*, 1005-1008.
40. Rashba, E. I.; Efros, A. L. Orbital mechanisms of electron-spin manipulation by an electric field. *Physical Review Letters* **2003,** *91*, 126405.
41. Wu, S.; Han, G.; Milliron, D. J.; Aloni, S.; Altoe, V.; Talapin, D. V.; Cohen, B. E.; Schuck, P. J. Non-blinking and photostable upconverted luminescence from single lanthanide-doped nanocrystals. *Proceedings of the National Academy of Sciences* **2009,** *106*, 10917-10921.
42. Mocatta, D.; Cohen, G.; Schattner, J.; Millo, O.; Rabani, E.; Banin, U. Heavily doped semiconductor nanocrystal quantum dots. *Science* **2011,** *332*, 77-81.
43. Jawaid, A. M.; Chattopadhyay, S.; Wink, D. J.; Page, L. E.; Snee, P. T. Cluster-seeded synthesis of doped CdSe:$Cu_4$ quantum dots. *ACS Nano* **2013,** *7*, 3190-3197.
44. Hassan, A.; Zhang, X.; Liu, X.; Rowland, C. E.; Jawaid, A. M.; Chattopadhyay, S.; Gulec, A.; Shamirian, A.; Zuo, X.; Klie, R. F.; Schaller, R. D.; Snee, P. T. Charge carriers modulate the bonding of semiconductor nanoparticle dopants as revealed by time-resolved X-ray spectroscopy. *ACS Nano* **2017,** *11*, 10070-10076.
45. Bhargava, R. N.; Gallagher, D.; Hong, X.; Nurmikko, A. Optical properties of manganese-doped nanocrystals of ZnS. *Physical Review Letters* **1994,** *72*, 416-419.
46. Lesnyak, V.; Gaponik, N.; Eychmuller, A. Colloidal semiconductor nanocrystals: The aqueous approach. *Chemical Society Reviews* **2013,** *42*, 2905-2929.
47. Chan, W. C. W.; Nie, S. Quantum dot bioconjugates for ultrasensitive nonisotopic detection. *Science* **1998,** *281*, 2016-2018.
48. Bruchez, M.; Moronne, M.; Gin, P.; Weiss, S.; Alivisatos, A. P. Semiconductor nanocrystals as fluorescent biological labels. *Science* **1998,** *281*, 2013-2016.
49. Mattoussi, H.; Mauro, J. M.; Goldman, E. R.; Anderson, G. P.; Sundar, V. C.; Mikulec, F. V.; Bawendi, M. G. Self-assembly of CdSe−ZnS quantum dot bioconjugates using an engineered recombinant protein. *Journal of the American Chemical Society* **2000,** *122*, 12142-12150.
50. Liu, D.; Snee, P. T. Water-soluble semiconductor nanocrystals cap exchanged with metalated ligands. *ACS Nano* **2011,** *5*, 546-550.

51. Dai, M.-Q.; Yung, L.-Y. L. Ethylenediamine-assisted ligand exchange and phase transfer of oleophilic quantum dots: Stripping of original ligands and preservation of photoluminescence. *Chemistry of Materials* **2013,** *25*, 2193-2201.
52. Aldana, J.; Wang, Y. A.; Peng, X. Photochemical instability of CdSe nanocrystals coated by hydrophilic thiols. *Journal of the American Chemical Society* **2001,** *123*, 8844-8850.
53. Wu, X.; Liu, H.; Liu, J.; Haley, K. N.; Treadway, J. A.; Larson, J. P.; Ge, N.; Peale, F.; Bruchez, M. P. Immunofluorescent labeling of cancer marker Her2 and other cellular targets with semiconductor quantum dots. *Nature Biotechnology* **2003,** *21*, 41-46.
54. Pellegrino, T.; Manna, L.; Kudera, S.; Liedl, T.; Koktysh, D.; Rogach, A. L.; Keller, S.; Rädler, J.; Natile, G.; Parak, W. J. Hydrophobic nanocrystals coated with an amphiphilic polymer shell: A general route to water soluble nanocrystals. *Nano Letters* **2004,** *4*, 703-707.
55. Yu, W. W.; Chang, E.; Falkner, J. C.; Zhang, J.; Al-Somali, A. M.; Sayes, C. M.; Johns, J.; Drezek, R.; Colvin, V. L. Forming biocompatible and nonaggregated nanocrystals in water using amphiphilic polymers. *Journal of the American Chemical Society* **2007,** *129*, 2871-2879.
56. Smith, A. M.; Duan, H.; Rhyner, M. N.; Ruan, G.; Nie, S. A systematic examination of surface coatings on the optical and chemical properties of semiconductor quantum dots. *Physical Chemistry Chemical Physics* **2006,** *8*, 3895-3903.
57. Tyrakowski, C. M.; Snee, P. T. A primer on the synthesis, water-solubilization, and functionalization of quantum dots, their use as biological sensing agents, and present status. *Physical Chemistry Chemical Physics.* **2014,** *16*, 837-855.
58. Vannoy, C. H.; Leblanc, R. M. Effects of DHLA-capped CdSe/ZnS quantum dots on the fibrillation of human serum albumin. *The Journal of Physical Chemistry B* **2010,** *114*, 10881-10888.
59. Snee, P. T.; Tyrakowski, C. M.; Page, L. E.; Isovic, A.; Jawaid, A. M. Quantifying quantum dots through förster resonant energy transfer. *The Journal of Physical Chemistry C* **2011,** *115*, 19578-19582.
60. Halpert, J. E.; Tischler, J. R.; Nair, G.; Walker, B. J.; Liu, W.; Bulović, V.; Bawendi, M. G. Electrostatic formation of quantum dot/J-aggregate FRET pairs in solution. *The Journal of Physical Chemistry C* **2009,** *113*, 9986-9992.
61. Chen, Y.; Thakar, R.; Snee, P. T. Imparting nanoparticle function with size-controlled amphiphilic polymers. *Journal of the American Chemical Society* **2008,** *130*, 3744-3745.
62. Sheehan, J.; Cruickshank, P.; Boshart, G. Notes- a convenient synthesis of water-soluble carbodiimides. *The Journal of Organic Chemistry* **1961,** *26*, 2525-2528.
63. Shen, H.; Jawaid, A. M.; Snee, P. T. Poly(ethylene glycol) carbodiimide coupling reagents for the biological and chemical functionalization of water-soluble nanoparticles. *ACS Nano* **2009,** *3*, 915-923.
64. Zhang, X.; Mohandessi, S.; Miller, L. W.; Snee, P. T. Efficient functionalization of aqueous CdSe/ZnS nanocrystals using small-molecule chemical activators. *Chemical Communications* **2011,** *47*, 3532-3534.
65. Dif, A.; Boulmedais, F.; Pinot, M.; Roullier, V.; Baudy-Floc'h, M.; Coquelle, F. M.; Clarke, S.; Neveu, P.; Vignaux, F.; Borgne, R. L.; Dahan, M.; Gueroui, Z.; Marchi-Artzner, V. Small and stable peptidic pegylated quantum dots to target polyhistidine-

tagged proteins with controlled stoichiometry. *Journal of the American Chemical Society* **2009,** *131*, 14738-14746.
66. Roullier, V.; Clarke, S.; You, C.; Pinaud, F.; Gouzer, G.; Schaible, D.; Marchi-Artzner, V.; Piehler, J.; Dahan, M. High-affinity labeling and tracking of individual histidine-tagged proteins in live cells using $Ni^{2+}$ tris-nitrilotriacetic acid quantum dot conjugates. *Nano Letters* **2009,** *9*, 1228-1234.
67. Jennings, T. L.; Becker-Catania, S. G.; Triulzi, R. C.; Tao, G.; Scott, B.; Sapsford, K. E.; Spindel, S.; Oh, E.; Jain, V.; Delehanty, J. B.; Prasuhn, D. E.; Boeneman, K.; Algar, W. R.; Medintz, I. L. Reactive semiconductor nanocrystals for chemoselective biolabeling and multiplexed analysis. *ACS Nano* **2011,** *5*, 5579-5593.
68. Brunel, F. M.; Lewis, J. D.; Destito, G.; Steinmetz, N. F.; Manchester, M.; Stuhlmann, H.; Dawson, P. E. Hydrazone ligation strategy to assemble multifunctional viral nanoparticles for cell imaging and tumor targeting. *Nano Letters* **2010,** *10*, 1093-1097.
69. Ekimov, A. I.; Efros, A. L.; Onushchenko, A. A. Quantum size effect in semiconductor microcrystals. *Solid State Communications* **1985,** *56*, 921-924.
70. Yu, W. W.; Qu, L.; Guo, W.; Peng, X. Experimental determination of the extinction coefficient of CdTe, CdSe, and CdS nanocrystals. *Chemistry of Materials* **2003,** *15*, 2854-2860.
71. Alén, B.; Bickel, F.; Karrai, K.; Warburton, R. J.; Petroff, P. M. Stark-shift modulation absorption spectroscopy of single quantum dots. *Applied Physics Letters* **2003,** *83*, 2235-2237.
72. Leatherdale, C. A.; Woo, W. K.; Mikulec, F. V.; Bawendi, M. G. On the absorption cross section of CdSe nanocrystal quantum dots. *The Journal of Physical Chemistry B* **2002,** *106*, 7619-7622.
73. Adam, S.; Talapin, D. V.; Borchert, H.; Lobo, A.; McGinley, C.; de Castro, A. R. B.; Haase, M.; Weller, H.; Möller, T. The effect of nanocrystal surface structure on the luminescence properties: Photoemission study of HF-etched InP nanocrystals. *The Journal of Chemical Physics* **2005,** *123*, 084706.
74. Kuçur, E.; Bücking, W.; Giernoth, R.; Nann, T. Determination of defect states in semiconductor nanocrystals by cyclic voltammetry. *The Journal of Physical Chemistry B* **2005,** *109*, 20355-20360.
75. Pal, D.; Stoleru, V. G.; Towe, E.; Firsov, D. Quantum dot-size variation and its impact on emission and absorption characteristics: An experimental and theoretical modeling investigation. *Japanese Journal of Applied Physics* **2002,** *41*, 482.
76. Bunker, G., *Introduction to XAFS: A practical guide to X-ray absorption fine structure spectroscopy*. Cambridge University Press: Cambridge, 2010.
77. Chen, L. X.; Zhang, X. Photochemical processes revealed by X-ray transient absorption spectroscopy. *The Journal of Physical Chemistry Letters* **2013,** *4*, 4000-4013.
78. Chen, L. X. Probing transient molecular structures in photochemical processes using laser-initiated time-resolved x-ray absorption spectroscopy. *Annual Review of Physical Chemistry* **2004,** *56*, 221-254.
79. Chen, L. X. Taking snapshots of photoexcited molecules in disordered media by using pulsed synchrotron X-rays. *Angewandte Chemie International Edition* **2004,** *43*, 2886-2905.

80. Bearden, J. A.; Burr, A. F. Reevaluation of X-ray atomic energy levels. *Reviews of Modern Physics* **1967,** *39*, 125-142.
81. Rehr, J. J.; Albers, R. C. Theoretical approaches to X-ray absorption fine structure. *Reviews of Modern Physics* **2000,** *72*, 621-654.
82. Bearden, J. A. X-ray wavelengths. *Reviews of Modern Physics* **1967,** *39*, 78-124.
83. Lamberti, Carlo. In *Characterization of semiconductor heterostructures and nanostructures*, Elsevier: Amsterdam, 2008; p III.
84. Kelly, S. D.; Hesterberg, D.; Ravel, B., Analysis of soils and minerals using X-ray absorption spectroscopy. In *Methods of soil analysis part 5—mineralogical methods*, Soil Science Society of America: Madison, WI, 2008; pp 387-463.
85. Rehr, J. J.; Kas, J. J.; Vila, F. D.; Prange, M. P.; Jorissen, K. Parameter-free calculations of X-ray spectra with FEFF9. *Physical Chemistry Chemical Physics* **2010,** *12*, 5503-5513.
86. Francesco, d. A. Advanced methods for the analysis of X-ray absorption spectroscopy data applied to semiconductors. *Semiconductor Science and Technology* **2011,** *26*, 064004.
87. d'Acapito, F.; Milita, S.; Satta, A.; Colombo, L. Depth resolved study of impurity sites in low energy ion implanted As in Si. *Journal of Applied Physics* **2007,** *102*, 043524.
88. Bersani, M.; Pepponi, G.; Giubertoni, D.; Gennaro, S.; Sahiner, M. A.; Kelty, S. P.; Kah, M.; Kirkby, K. J.; Doherty, R.; Foad, M. A.; Meirer, F.; Streli, C.; Woicik, J. C.; Pianetta, P. In *Characterization of junction activation and deactivation using non-equilibrium annealing: Solid phase epitaxy, spike annealing, laser annealing instructions for* International Workshop on Junction Technology, 11-12 June 2009; 2009; pp 64-68.
89. Giubertoni, D.; Pepponi, G.; Sahiner, M. A.; Kelty, S. P.; Gennaro, S.; Bersani, M.; Kah, M.; Kirkby, K. J.; Doherty, R.; Foad, M. A.; Meirer, F.; Streli, C.; Woicik, J. C.; Pianetta, P. Deactivation of submelt laser annealed arsenic ultrashallow junctions in silicon during subsequent thermal treatment. *Journal of Vacuum Science & Technology B, Nanotechnology and Microelectronics: Materials, Processing, Measurement, and Phenomena* **2010,** *28*, C1B1-C1B5.
90. Coe, S.; Woo, W.-K.; Bawendi, M.; Bulović, V. Electroluminescence from single monolayers of nanocrystals in molecular organic devices. *Nature* **2002,** *420*, 800.
91. Klimov, V. I.; Ivanov, S. A.; Nanda, J.; Achermann, M.; Bezel, I.; McGuire, J. A.; Piryatinski, A. Single-exciton optical gain in semiconductor nanocrystals. *Nature* **2007,** *447*, 441.
92. Klimov, V. I.; Mikhailovsky, A. A.; Xu, S.; Malko, A.; Hollingsworth, J. A.; Leatherdale, C. A.; Eisler, H. J.; Bawendi, M. G. Optical gain and stimulated emission in nanocrystal quantum dots. *Science* **2000,** *290*, 314.
93. Konstantatos, G.; Howard, I.; Fischer, A.; Hoogland, S.; Clifford, J.; Klem, E.; Levina, L.; Sargent, E. H. Ultrasensitive solution-cast quantum dot photodetectors. *Nature* **2006,** *442*, 180.
94. Gur, I.; Fromer, N. A.; Geier, M. L.; Alivisatos, A. P. Air-stable all-inorganic nanocrystal solar cells processed from solution. *Science* **2005,** *310*, 462.

95. Yu, G.; Gao, J.; Hummelen, J. C.; Wudl, F.; Heeger, A. J. Polymer photovoltaic cells: Enhanced efficiencies via a network of internal donor-acceptor heterojunctions. *Science* **1995,** *270*, 1789.
96. IFC - Editorial board. *Solar Energy Materials and Solar Cells* **2005,** *87*, CO2.
97. Dubertret, B.; Skourides, P.; Norris, D. J.; Noireaux, V.; Brivanlou, A. H.; Libchaber, A. *In vivo* imaging of quantum dots encapsulated in phospholipid micelles. *Science* **2002,** *298*, 1759.
98. Gao, X.; Cui, Y.; Levenson, R. M.; Chung, L. W. K.; Nie, S. *In vivo* cancer targeting and imaging with semiconductor quantum dots. *Nature Biotechnology* **2004,** *22*, 969.
99. Stroh, M.; Zimmer, J. P.; Duda, D. G.; Levchenko, T. S.; Cohen, K. S.; Brown, E. B.; Scadden, D. T.; Torchilin, V. P.; Bawendi, M. G.; Fukumura, D.; Jain, R. K. Quantum dots spectrally distinguish multiple species within the tumor milieu *in vivo*. *Nature Medicine* **2005,** *11*, 678.
100. Moore, G. E. Cramming more components onto integrated circuits, reprinted from electronics, volume 38,1965, pp.114
101. Bardeen, J.; Brattain, W. H. The transistor, a semi-conductor triode. *Physical Review* **1948,** *74*, 230-231.
102. Conwell, E.; Weisskopf, V. F. Theory of impurity scattering in semiconductors. *Physical Review* **1950,** *77*, 388-390.
103. Chattopadhyay, D.; Queisser, H. J. Electron scattering by ionized impurities in semiconductors. *Reviews of Modern Physics* **1981,** *53*, 745-768.
104. Chen, L. X.; Jäger, W. J. H.; Jennings, G.; Gosztola, D. J.; Munkholm, A.; Hessler, J. P. Capturing a photoexcited molecular structure through time-domain X-ray absorption fine structure. *Science* **2001,** *292*, 262-264.
105. Saes, M.; Bressler, C.; Abela, R.; Grolimund, D.; Johnson, S. L.; Heimann, P. A.; Chergui, M. Observing photochemical transients by ultrafast X-ray absorption spectroscopy. *Physical Review Letters* **2003,** *90*, 047403.
106. Bressler, C.; Chergui, M. Molecular structural dynamics probed by ultrafast X-ray absorption spectroscopy. *Annual Review of Physical Chemistry* **2010,** *61*, 263-282.
107. Pickett, N. (Nanoco Technologies Limited, GB) Controlled Preparation of Nanoparticle Materials. U.S. Patent 7,867,556, October 27, **2006**..
108. Santiago-González, B.; Monguzzi, A.; Pinchetti, V.; Casu, A.; Prato, M.; Lorenzi, R.; Campione, M.; Chiodini, N.; Santambrogio, C.; Meinardi, F.; Manna, L.; Brovelli, S. "Quantized" doping of individual colloidal nanocrystals using size-focused metal quantum clusters. *ACS Nano* **2017,** *11*, 6233-6242.
109. Chikan, V. Challenges and prospects of electronic doping of colloidal quantum dots: Case study of CdSe. *The Journal of Physical Chemistry Letters* **2011,** *2*, 2783-2789.
110. Nelson, H. D.; Li, X.; Gamelin, D. R. Computational studies of the electronic structures of copper-doped CdSe nanocrystals: Oxidation states, Jahn–Teller distortions, vibronic bandshapes, and singlet–triplet splittings. *The Journal of Physical Chemistry C* **2016,** *120*, 5714-5723.
111. Dance, I. G.; Choy, A.; Scudder, M. L. Syntheses, properties, and molecular and crystal-structures of $(Me_4N)_4[E_4M_{10}(SPh)_{16}]$ (E = sulfur or selenium; m = zinc or cadmium): Molecular supertetrahedral fragments of the cubic metal chalcogenide lattice. *Journal of the American Chemical Society.* **1984,** *106*, 6285-6295.

112. Bain, G. A.; Berry, J. F. Diamagnetic corrections and Pascal's constants. *Journal of Chemical Education* **2008,** *85*, 532.
113. Ilavsky, J.; Jemian, P. R. Irena: Tool suite for modeling and analysis of small-angle scattering. Journal *of Applied Crystallogra114phy.* **2009,** *42*, 347-353.
114. U.S. Environmental Protection Agency. Method 3050B: Acid Digestion of Sediments, Sludges, and Soils; 1996.
115. Adamo, C.; Barone, V. Toward reliable density functional methods without adjustable parameters: The PBE0 model. *Journal of Chemical Physics.* **1999,** *110*, 6158-6170.
116. Perdew, J. P.; Burke, K.; Ernzerhof, M. Generalized gradient approximation made simple. *Physical Review.* **1996,** *77*, 3865-3868.
117. Stevens, W. J.; Krauss, M.; Basch, H.; Jasien, P. G. Relativistic compact effective potentials and efficient, shared-exponent basis sets for the third-, fourth-, and fifth-row atoms. *Canadian Journal of Chemistry* **1992,** *70*, 612-630.
118. Hay, P. J.; Wadt, W. R. Abinitio effective core potentials for molecular calculations potentials for the transition-metal atoms Sc to Hg. *Journal of Chemical Physics.* **1985,** *82*, 270-283.
119. Hay, P. J.; Wadt, W. R. Ab initio effective core potentials for molecular calculations potentials for K to Au including the outermost core orbitals. *Journal of Chemical Physics* **1985,** *82*, 299-310.
120. Wadt, W. R.; Hay, P. J. Abinitio effective core potentials for molecular calculations potentials for main group elements Na to Bi. *Journal of Chemical Physics.* **1985,** *82*, 284-298.
121. Del Ben, M.; Havenith, R. W. A.; Broer, R.; Stener, M. Density functional study on the morphology and photoabsorption of CdSe nanoclusters. *Journal of Physical Chemistry C* **2011,** *115*, 16782-16796.
122. Frisch, M. J.; Trucks, G. W.; Schlegel, H. B.; Scuseria, G. E.; Robb, M. A.; Cheeseman, J.R.; Scalmani, G.; Barone, V.; Mennucci, B.; Petersson, G.A.; Nakatsuji H.; Caricato, M.; Li, X.; Hratchian, H.P.; Izmaylov, A.F.; Bloino, J.; Zheng, G.; Sonnenb erg, J. L.; Hada, M.; Ehara, M.; *Gaussian 09*, revision B.01; Gaussian Inc.: Wallingford, CT, **2009**.
123. Martin, R. L. Natural transition orbitals. *Journal of Chemical Physics* **2003,** *118*, 4775-4777.
124. Glendening, E. D.; Badenhoop, J. K.; Reed, A. E.; Carpenter, J. E.; Bohmann, J. A.; Morales, C. M.; Landis, C. R.; Weinhold, F. *NBO 6.0*, Theoretical Chemistry Institute: University of Wisconsin, Madison, 2013.
125. GaussView, V., Roy Dennington, Todd A. Keith, and John M. Millam, Semichem Inc., Shawnee Mission, KS, 2016.
126. Pradhan, N.; Goorskey, D.; Thessing, J.; Peng, X. An alternative of CdSe nanocrystal emitters: Pure and tunable impurity emissions in ZnSe nanocrystals. *Journal of the American Chemical Society* **2005,** *127*, 17586-17587.
127. Viswanatha, R.; Brovelli, S.; Pandey, A.; Crooker, S. A.; Klimov, V. I. Copper-doped inverted core/shell nanocrystals with "permanent" optically active holes. *Nano Letters* **2011,** *11*, 4753-4758.

128. Knowles, K. E.; Hartstein, K. H.; Kilburn, T. B.; Marchioro, A.; Nelson, H. D.; Whitham, P. J.; Gamelin, D. R. Luminescent colloidal semiconductor nanocrystals containing copper: Synthesis, photophysics, and applications. *Chemical Reviews* **2016,** *116*, 10820-10851.
129. Grandhi, G. K.; Tomar, R.; Viswanatha, R. Study of surface and bulk electronic structure of II–VI semiconductor nanocrystals using Cu as a nanosensor. *ACS Nano* **2012,** *6*, 9751-9763.
130. Gul, S.; Cooper, J. K.; Glans, P.-A.; Guo, J.; Yachandra, V. K.; Yano, J.; Zhang, J. Z. Effect of $Al^{3+}$ co-doping on the dopant local structure, optical properties, and exciton dynamics in $Cu^{+}$-doped ZnSe nanocrystals. *ACS Nano* **2013,** *7*, 8680-8692.
131. Kau, L. S.; Spira-Solomon, D. J.; Penner-Hahn, J. E.; Hodgson, K. O.; Solomon, E. I. X-ray absorption edge determination of the oxidation state and coordination number of copper. Application to the type 3 site in Rhus vernicifera laccase and its reaction with oxygen. *Journal of the American Chemical Society* **1987,** *109*, 6433-6442.
132. Bocharov, S.; Kirchner, T.; Dräger, G.; Šipr, O.; Šimůnek, A. Dipole and quadrupole contributions to polarized Cu k X-ray absorption near-edge structure spectra of CuO. *Physical Review B* **2001,** *63*, 045104.
133. Yokoyama, T.; Kosugi, N.; Kuroda, H. Polarized XANES spectra of $CuCl_2 \cdot 2H_2O$. Further evidence for shake-down phenomena. *Chemical Physics* **1986,** *103*, 101-109.
134. Blackburn, N. J.; Strange, R. W.; Farooq, A.; Haka, M. S.; Karlin, K. D. X-ray absorption studies of three-coordinate dicopper(I) complexes and their dioxygen adducts. *Journal of the American Chemical Society* **1988,** *110*, 4263-4272.
135. Mara, M. W.; Jackson, N. E.; Huang, J.; Stickrath, A. B.; Zhang, X.; Gothard, N. A.; Ratner, M. A.; Chen, L. X. Effects of electronic and nuclear interactions on the excited-state properties and structural dynamics of copper(I) diimine complexes. *The Journal of Physical Chemistry B* **2013,** *117*, 1921-1931.
136. Choi, D.; Pyo, J.-Y.; Jang, D.-J. Impurity location-dependent relaxation dynamics of Cu:CdS quantum dots. *Nanoscale Research Letters* **2017,** *12*, 49.
137. Holmberg, V. C.; Collier, K. A.; Korgel, B. A. Real-time observation of impurity diffusion in silicon nanowires. *Nano Letters* **2011,** *11*, 3803-3808.
138. E. D. Glendening, J., K. Badenhoop, A. E. Reed, J. E. Carpenter, J. A. Bohmann, C. M. Morales, C. R. Landis, and F. Weinhold *NBO 6.0*, University of Wisconsin, Madison: Theoretical Chemistry Institute, 2013.
139. Johnson, B. J.; Antholine, W. E.; Lindeman, S. V.; Graham, M. J.; Mankad, N. P. A one-hole $Cu_4S$ cluster with $N_2O$ reductase activity: A structural and functional model for $Cu_Z$*. *Journal of the American Chemical Society* **2016,** *138*, 13107-13110.
140. Mott, N. F. Metal-insulator transition. *Reviews of Modern Physics* **1968,** *40*, 677-683.
141. Kobashi, M.; Takeuchi, H. Inhomogeneity of spin-coated and cast non-regioregular poly(3-hexylthiophene) films. Structures and electrical and photophysical properties. *Macromolecules* **1998,** *31*, 7273-7278.
142. Sirringhaus, H.; Brown, P. J.; Friend, R. H.; Nielsen, M. M.; Bechgaard, K.; Langeveld-Voss, B. M. W.; Spiering, A. J. H.; Janssen, R. A. J.; Meijer, E. W.; Herwig, P.; de Leeuw, D. M. Two-dimensional charge transport in self-organized, high-mobility conjugated polymers. *Nature* **1999,** *401*, 685-688.

143. Veamatahau, A.; Jiang, B.; Seifert, T.; Makuta, S.; Latham, K.; Kanehara, M.; Teranishi, T.; Tachibana, Y. Origin of surface trap states in CdS quantum dots: Relationship between size dependent photoluminescence and sulfur vacancy trap states. *Physical Chemistry Chemical Physics* **2015,** *17*, 2850-2858.
144. Hässelbarth, A.; Eychmüller, A.; Weller, H. Detection of shallow electron traps in quantum sized CdS by fluorescence quenching experiments. *Chemical Physics Letters* **1993,** *203*, 271-276.
145. Erwin, S. C.; Zu, L.; Haftel, M. I.; Efros, A. L.; Kennedy, T. A.; Norris, D. J. Doping semiconductor nanocrystals. *Nature* **2005,** *436*, 91.
146. Norris, D. J.; Efros, A. L.; Erwin, S. C. Doped nanocrystals. *Science* **2008,** *319*, 1776.
147. Pradhan, N.; Das Adhikari, S.; Nag, A.; Sarma, D. D. Luminescence, plasmonic, and magnetic properties of doped semiconductor nanocrystals. *Angewandte Chemie International Edition* **2017,** *56*, 7038-7054.
148. Pradhan, N.; Sarma, D. D. Advances in light-emitting doped semiconductor nanocrystals. *The Journal of Physical Chemistry Letters* **2011,** *2*, 2818-2826.
149. Debnath, T.; Maiti, S.; Ghosh, H. N. Unusually slow electron cooling to charge-transfer state in gradient CdTeSe alloy nanocrystals mediated through Mn atom. *The Journal of Physical Chemistry Letters* **2016,** *7*, 1359-1367.
150. Thakar, R.; Chen, Y. C.; Snee, P. T. Efficient emission from core/(doped) shell nanoparticles: Applications for chemical sensing. *Nano Letters* **2007,** *7*, 3429-3432.
151. Wood, V.; Halpert, J. E.; Panzer, M. J.; Bawendi, M. G.; Bulovic, V. Alternating current driven electroluminescence from ZnSe/ZnS:Mn/ZnS nanocrystals. *Nano Letters* **2009,** *9*, 2367-2371.
152. Liu, H.; Zhitomirsky, D.; Hoogland, S.; Tang, J.; Kramer, I. J.; Ning, Z. J.; Sargent, E. H. Systematic optimization of quantum junction colloidal quantum dot solar cells. *Applied Physics Letters* **2012,** *101*.
153. Ning, Z. J.; Voznyy, O.; Pan, J.; Hoogland, S.; Adinolfi, V.; Xu, J. X.; Li, M.; Kirmani, A. R.; Sun, J. P.; Minor, J.; Kemp, K. W.; Dong, H. P.; Rollny, L.; Labelle, A.; Carey, G.; Sutherland, B.; Hill, I. G.; Amassian, A.; Liu, H.; Tang, J.; Bakr, O. M.; Sargent, E. H. Air-stable n-type colloidal quantum dot solids. *Nature Materials* **2014,** *13*, 822-828.
154. Talapin, D. V.; Lee, J.-S.; Kovalenko, M. V.; Shevchenko, E. V. Prospects of colloidal nanocrystals for electronic and optoelectronic applications. *Chem. Rev* **2010,** *110*, 389-458.
155. Erdem, T.; Demir, H. V. Semiconductor nanocrystals as rare-earth alternatives. *Nature Photonics* **2011,** *5*, 126-126.
156. Brazis, P. W., Quantum dots and their potential impact on lighting and display applications. Underwriters Laboratories: 2017.
157. Puzzo, D. P.; Henderson, E. J.; Helander, M. G.; Wang, Z.; Ozin, G. A.; Lu, Z. Visible colloidal nanocrystal silicon light-emitting diode. *Nano letters* **2011,** *11*, 1585-1590.
158. Wang, A.; Shen, H.; Zang, S.; Lin, Q.; Wang, H.; Qian, L.; Niu, J.; Li, L. S. Bright, efficient, and color-stable violet ZnSe-based quantum dot light-emitting diodes. *Nanoscale* **2015,** *7*, 2951-2959.

159. Tan, Z.; Zhang, Y.; Xie, C.; Su, H.; Liu, J.; Zhang, C.; Dellas, N.; Mohney, S. E.; Wang, Y.; Wang, J. Near-band-edge electroluminescence from heavy-metal-free colloidal quantum dots. *Advanced Materials* **2011,** *23*, 3553-3558.
160. Zhang, Y.; Xie, C.; Su, H.; Liu, J.; Pickering, S.; Wang, Y.; Yu, W. W.; Wang, J.; Wang, Y.; Hahm, J.-I. Employing heavy metal-free colloidal quantum dots in solution-processed white light-emitting diodes. *Nano letters* **2010,** *11*, 329-332.
161. Yang, X.; Zhao, D.; Leck, K. S.; Tan, S. T.; Tang, Y. X.; Zhao, J.; Demir, H. V.; Sun, X. W. Full visible range covering InP/ZnS nanocrystals with high photometric performance and their application to white quantum dot light-emitting diodes. *Advanced Materials* **2012,** *24*, 4180-4185.
162. Williams, E.; Elder, W.; Astles, M.; Webb, M.; Mullin, J.; Straughan, B.; Tufton, P. Indium phosphide I. A photoluminescence materials study. *Journal of The Electrochemical Society* **1973,** *120*, 1741-1749.
163. Duan, X.; Huang, Y.; Cui, Y.; Wang, J.; Lieber, C. M. Indium phosphide nanowires as building blocks for nanoscale electronic and optoelectronic devices. *Nature* **2001,** *409*, 66-69.
164. Xie, L.; Harris, D. K.; Bawendi, M. G.; Jensen, K. F. Effect of trace water on the growth of indium phosphide quantum dots. *Chemistry of Materials* **2015,** *27*, 5058-5063.
165. Franke, D.; Harris, D. K.; Xie, L.; Jensen, K. F.; Bawendi, M. G. The unexpected influence of precursor conversion rate in the synthesis of III-V quantum dots. *Angewandte Chemie-International Edition* **2015,** *54*, 14299-14303.
166. Cossairt, B. M. Shining light on indium phosphide quantum dots: Understanding the interplay among precursor conversion, nucleation, and growth. *Chemistry of Materials* **2016,** *28*, 7181-7189.
167. Heath, J. R. Covalency in semiconductor quantum dots. *Chemical Society Reviews* **1998,** *27*, 65-71.
168. Wu, J.; Walukiewicz, W.; Yu, K. M.; Ager, J. W.; Haller, E. E.; Lu, H.; Schaff, W. J.; Saito, Y.; Nanishi, Y. Unusual properties of the fundamental band gap of InN. *Applied Physics Letters* **2002,** *80*, 3967-3969.
169. Neufeld, C. J.; Toledo, N. G.; Cruz, S. C.; Iza, M.; DenBaars, S. P.; Mishra, U. K. High quantum efficiency InGaN/GaN solar cells with 2.95 eV band gap. *Applied Physics Letters* **2008,** *93*.
170. Nakamura, S.; Fasol, G., *The blue laser diode. GaN based light emitters and lasers*. Springer-Verlag: New York, 1997.
171. Brennan, K. F., *The physics of semiconductors: With applications to optoelectronic devices*. Cambridge University Press: 1999.
172. Morkoc, H.; Strite, S.; Gao, G. B.; Lin, M. E.; Sverdlov, B.; Burns, M. Large-band-gap SiC, III-V nitride, and II-VI ZnSe-based semiconductor-device technologies. *Journal of Applied Physics* **1994,** *76*, 1363-1398.
173. Gratzel, M. Photoelectrochemical cells. *Nature* **2001,** *414*, 338-344.
174. del Alamo, J. A. In *The high-electron mobility transistor at 30: Impressive accomplishments and exciting prospects*, 2011 International Conference on Compound Semiconductor Manufacturing Technology, Indian Wells, California, Indian Wells, California, 2011.

175. Koningsberger, D.; Prins, R. X-ray absorption: Principles, applications, techniques of EXAFS, SEXAFS, and XANES. **1988**.
176. Stern, E.; Heald, S. Basic principles and applications of EXAFS. *Handbook on synchrotron radiation* **1983,** *1*, 955-1014.
177. Gul, S.; Cooper, J. K.; Corrado, C.; Vollbrecht, B.; Bridges, F.; Guo, J. H.; Zhang, J. Z. Synthesis, optical and structural properties, and charge carrier dynamics of Cu-doped ZnSe nanocrystals. *Journal of Physical Chemistry C* **2011,** *115*, 20864-20875.
178. Xie, R.; Peng, X. Synthesis of Cu-doped InP nanocrystals (d-dots) with ZnSe diffusion barrier as efficient and color-tunable NIR emitters. *Journal of the American Chemical Society* **2009,** *131*, 10645-10651.
179. Gary, D. C.; Flowers, S. E.; Kaminsky, W.; Petrone, A.; Li, X. S.; Cossairt, B. M. Single-crystal and electronic structure of a 1.3 nm indium phosphide nanocluster. *Journal of the American Chemical Society* **2016,** *138*, 1510-1513.
180. Skolnick, M. S.; Dean, P. J.; Pitt, A. D.; Uihlein, C.; Krath, H.; Deveaud, B.; Foulkes, E. J. Optical-properties of copper-related centers in InP. *Journal of Physics C-Solid State Physics* **1983,** *16*, 1967-1985.
181. Amit, Y.; Eshet, H.; Faust, A.; Patllola, A.; Rabani, E.; Banin, U.; Frenkel, A. I. Unraveling the impurity location and binding in heavily doped semiconductor nanocrystals: The case of Cu in InAs nanocrystals. *Journal of Physical Chemistry C* **2013,** *117*, 13688-13696.
182. Chadi, D. J. The problem of doping in II-VI semiconductors. *Annual Review of Materials Science* **1994,** *24*, 45-62.
183. Carter, R. Oxygen: The molecule that made the world. *Journal of the Royal Society of Medicine* **2003,** *96*, 46-47.
184. Amao, Y. Probes and polymers for optical sensing of oxygen. *Microchimica Acta* **2003,** *143*, 1-12.
185. Somers, R. C.; Bawendi, M. G.; Nocera, D. G. CdSe nanocrystal based chem-/bio-sensors. *Chemical Society Reviews* **2007,** *36*, 579-591.
186. Jin, T.; Sasaki, A.; Kinjo, M.; Miyazaki, J. A quantum dot-based ratiometric pH sensor. *Chemical Communications* **2010,** *46*, 2408-2410.
187. Zhan, N.; Palui, G.; Mattoussi, H. Preparation of compact biocompatible quantum dots using multicoordinating molecular-scale ligands based on a zwitterionic hydrophilic motif and lipoic acid anchors. *Nature Protocols* **2015,** *10*, 859-874.
188. Liu, L.; Hu, R.; Roy, I.; Lin, G.; Ye, L.; Reynolds, J. L.; Liu, J.; Liu, J.; Schwartz, S. A.; Zhang, X.; Yong, K.-T. Synthesis of luminescent near-infrared $AgInS_2$ nanocrystals as optical probes for *in vivo* applications. *Theranostics* **2013,** *3*, 109-115.
189. McLaurin, E. J.; Greytak, A. B.; Bawendi, M. G.; Nocera, D. G. Two-photon absorbing nanocrystal sensors for ratiometric detection of oxygen. *Journal of the American Chemical Society* **2009,** *131*, 12994-13001.
190. Amelia, M.; Lavie-Cambot, A.; McClenaghan, N. D.; Credi, A. A ratiometric luminescent oxygen sensor based on a chemically functionalized quantum dot. *Chemical Communications* **2011,** *47*, 325-327.
191. Shamirian, A.; Samareh Afsari, H.; Hassan, A.; Miller, L. W.; Snee, P. T. In vitro detection of hypoxia using a ratiometric quantum dot-based oxygen sensor. *ACS Sensors* **2016,** *1*, 1244-1250.

192. Lemon, C. M.; Karnas, E.; Bawendi, M. G.; Nocera, D. G. Two-photon oxygen sensing with quantum dot-porphyrin conjugates. *Inorganic Chemistry* **2013,** *52*, 10394-10406.
193. Lemon, C. M.; Curtin, P. N.; Somers, R. C.; Greytak, A. B.; Lanning, R. M.; Jain, R. K.; Bawendi, M. G.; Nocera, D. G. Metabolic tumor profiling with pH, oxygen, and glucose chemosensors on a quantum dot scaffold. *Inorganic Chemistry* **2014,** *53*, 1900-1915.
194. Lemon, C. M.; Karnas, E.; Han, X. X.; Bruns, O. T.; Kempa, T. J.; Fukumura, D.; Bawendi, M. G.; Jain, R. K.; Duda, D. G.; Nocera, D. G. Micelle-encapsulated quantum dot-porphyrin assemblies as *in vivo* two-photon oxygen sensors. *Journal of the American Chemical Society* **2015,** *137*, 9832-9842.
195. Schwabacher, A. W.; Lane, J. W.; Schiesher, M. W.; Leigh, K. M.; Johnson, C. W. Desymmetrization reactions: Efficient preparation of unsymmetrically substituted linker molecules. *Journal of Organic Chemistry* **1998,** *63*, 1727-1729.
196. Pradhan, N.; Peng, X. Efficient and color-tunable Mn-doped ZnSe nanocrystal emitters: Control of optical performance via greener synthetic chemistry. *Journal of the American Chemical Society* **2007,** *129*, 3339-3347.
197. Thakar, R.; Chen, Y.; Snee, P. T. Efficient emission from core/(doped) shell nanoparticles: Applications for chemical sensing. *Nano Letters* **2007,** *7*, 3429-3432.
198. Chen, O.; Zhao, J.; Chauhan, V. P.; Cui, J.; Wong, C.; Harris, D. K.; Wei, H.; Han, H.-S.; Fukumura, D.; Jain, R. K.; Bawendi, M. G. Compact high-quality CdSe–CdS core–shell nanocrystals with narrow emission linewidths and suppressed blinking. *Nature Materials* **2013,** *12*, 445.
199. Tyrakowski, C. M.; Snee, P. T. Ratiometric CdSe/ZnS quantum dot protein sensor. *Analytical Chemistry* **2014,** *86*, 2380-2386.
200. Susumu, K.; Mei, B. C.; Mattoussi, H. Multifunctional ligands based on dihydrolipoic acid and polyethylene glycol to promote biocompatibility of quantum dots. *Nature Protocols* **2009,** *4*, 424.
201. Berendsen, H. J. C.; Grigera, J. R.; Straatsma, T. P. The missing term in effective pair potentials. *Journal of Physical Chemistry* **1987,** *91*, 6269-6271.
202. Stevens, W. J.; Krauss, M.; Basch, H.; Jasien, P. G. Relativistic compact effective potentials and efficient, shared-exponent basis-sets for the 3$^{rd}$-row, 4$^{th}$-row, and 5$^{th}$-row atoms. *Canadian Journal of Chemistry-Revue Canadienne De Chimie* **1992,** *70*, 612-630.
203. McBride, J.; Treadway, J.; Feldman, L. C.; Pennycook, S. J.; Rosenthal, S. J. Structural basis for near unity quantum yield core/shell nanostructures. *Nano Letters* **2006,** *6*, 1496-1501.
204. Namsani, S.; Nair, N. N.; Singh, J. K. Interaction potential models for bulk ZnS, ZnS nanoparticle, and ZnS nanoparticle-PMMA from first-principles. *Journal of Computational Chemistry* **2015,** *36*, 1176-1186.
205. Grunwald, M.; Zayak, A.; Neaton, J. B.; Geissler, P. L.; Rabani, E. Transferable pair potentials for CdS and ZnS crystals. *Journal of Chemical Physics* **2012,** *136*,136.
206. Bouanich, J. P. Site site Lennard-Jones potential parameters for $N_2$, $O_2$, $H_2$, Co and $Co_2$. *Journal of Quantitative Spectroscopy & Radiative Transfer* **1992,** *47*, 243-250.
207. Parker, C. A.; Hatchard, C. G. Delayed fluorescence of pyrene in ethanol. *Transactions of the Faraday Society* **1963,** *59*, 284-295.

208. Birks, J. B. Photophysics of Aromatic Molecules; John Wiley & Sons Ltd: New York, 1970.
209. Kennedy, T. A.; R. Glaser, E.; B. Klein, P.; N. Bhargava, R., Symmetry and electronic structure of the Mn impurity in ZnS nanocrystals. 1995; Vol. 52, p 14356-14359.
210. Yatsunenko, S.; Świątek, K.; Godlewski, M.; Fröba, M.; Klar, P.; Heimbrodt, W., Electron spin resonance investigations of ZnMnS nanoparticles. 2008; Vol. 30, p 753-755.
211. Magana, D.; Perera, S. C.; Harter, A. G.; Dalal, N. S.; Strouse, G. F. Switching-on superparamagnetism in Mn/CdSe quantum dots. *Journal of the American Chemical Society* **2006,** *128*, 2931-2939.
212. Humphry-Baker, R.; Moroi, Y.; Grätzel, M. Perturbation studies of the photophysics of arenes in functionalized micellar assemblies. Drastic phosphorescence enhancements. *Chemical Physics Letters* **1978,** *58*, 207-210.
213. Parmenter, C. S.; Rau, J. D. Fluorescence quenching in aromatic hydrocarbons by oxygen. *The Journal of Chemical Physics* **1969,** *51*, 2242-2246.
214. Belaid, R.; Barhoumi, T.; Hachani, L.; Hassine, L.; Bouchriha, H. Magnetic field effect on recombination light in anthracene crystal. *Synthetic Metals* **2002,** *131*, 23-30.
215. Faulkner, L. R.; Bard, A. J. Magnetic field effects on anthracene triplet-triplet annihilation in fluid solutions. *Journal of the American Chemical Society* **1969,** *91*, 6495-6497.
216. Tachikawa, H.; Bard, A. J. Magnetic field effects on oxygen quenching of delayed fluorescence of anthracene and pyrene in fluid solution. *Journal of the American Chemical Society* **1973,** *95*, 1672-1673.
217. Johnson, R. C.; Merrifield, R. E. Effects of magnetic fields on the mutual annihilation of triplet excitons in anthracene crystals. *Physical Review B* **1970,** *1*, 896-902.
218. Köhler, A.; Bässler, H. Triplet states in organic semiconductors. *Materials Science and Engineering: R: Reports* **2009,** *66*, 71-109.
219. Watkins, A. R. Oxygen quenching of the fluorescence of aromatic hydrocarbons in a polar solvent. *Chemical Physics Letters* **1979,** *65*, 380-384.
220. Geacintov, N. E.; Swenberg, C. E. Possible effects of magnetic fields on the quenching of triplet excited states of polynuclear hydrocarbons by oxygen. *The Journal of Chemical Physics* **1972,** *57*, 378-389.
221. Tsubomura, H.; Mulliken, R. S. Molecular complexes and their spectra. XII. Ultraviolet absorption spectra caused by the interaction of oxygen with organic molecules1. *Journal of the American Chemical Society* **1960,** *82*, 5966-5974.
222. Uddin, M. J.; Crews, B. C.; Ghebreselasie, K.; Marnett, L. J. Design, synthesis, and structure–activity relationship studies of fluorescent inhibitors of cycloxygenase-2 as targeted optical imaging agents. *Bioconjugate Chemistry* **2013,** *24*, 712-723.

# VITA


## Asra Hassan

## Department of Chemistry

## University of Illinois at Chicago


## EDUCATION

**Doctor of Philosophy (PhD), Chemistry** **2013 – present**
University of Illinois at Chicago (UIC) – Chicago, IL

**Bachelor of Science (BS), Chemistry** **2009 - 2013**
University of Illinois at Chicago (UIC) | *Graduated with Honors*

## PROFESSIONAL EXPERIENCE

**Graduate Research Assistant,** with Prof Preston Snee **2013 – present**
Department of Chemistry, University of Illinois at Chicago (UIC)
Thesis Title: "Synthesis, Characterization, & Photophysical Investigations of Doped Semiconductor Nanocrystals "

**Graduate Teaching Assistant,** **2013 – present**
Department of Chemistry, University of Illinois at Chicago (UIC)
For courses including Physical Chemistry, Analytical Chemistry, and General Chemistry

## HONORS AND AWARDS

**LAS PhD Student Travel Award** **2016**
University of Illinois at Chicago (UIC)
**The Outstanding Teaching Assistant Award** **2014**
University of Illinois at Chicago (UIC)
**American Chemical Society Excellence in Analytical Chemistry Award** **2013**
University of Illinois at Chicago (UIC)
**Dean's List** **2009 - 2013**
University Of Illinois at Chicago

## PROFESSIONAL AFFILIATIONS

**American Chemical Society** – Member **2016 – Present**
**Graduate Women in Chemistry, UIC** –Member **2015 – 2016**
**Chemistry Graduate Student Association (CGSA)** – Member **2013 – present**

## PUBLICATIONS

**1. Asra Hassan**, Xiaoyi Zhang, Cumming, Liu, Preston Snee, "**Time Electronic Structure and Dynamics of Copper Doped Indium Phosphide Nanocrystals Studied with Time-Resolved X-ray Absorption and Large Scale DFT Calculations"** *J. Phys. Chem. C,* **2017, ASAP**.

**2. Asra Hassan**, Xiaoyi Zhang, Xiaohan Liu, Claire E. Rowland, Soma Chattopadhyay, Xiaobing Zuo, Robert F. Klie, Richard D. Schaller, and Preston T. Snee, "**Charge Carriers Modulate the Bonding of Semiconductor Dopants as Revealed by Time-Resolved X-ray Spectroscopy** " *ACS Nano, 2017* 11, 10070-10076; DOI: 10.1021/acsnano.7b04414.

**3. Asra Hassan,** Armen Shamirian, Xi Zhang and Preston T. Snee. "**Anomalous Perturbation of the $O_2$ Sensitivity of Poly (aromatic) Hydrocarbons by Magnetic Quantum Dots"** *J. Phys. Chem. C,* **2017**, *121*, 4060-4065; DOI: 10.1021/acs.jpcc.6b12699.

**4.** Armen Shamirian, Hamed Afsari, **Asra Hassan**, Lawrence Miller and Preston Snee. "**I *n vitro* Detection of Hypoxia using a Ratiometic Quantum Dot-Based Oxygen Sensor**" *ACS Sensors*, **2016**, *1*, 1244-1250; DOI: 10.1021/acssensors.6b00452.

**5.** Xi Zhang, Armen Shamirian, Ali M. Jawaid, Christina M. Tyrakowski, Leah E. Page, Adita Das, Ou chen, Adela Isovic, **Asra Hassan**, Preston T. Snee, "**Monolayer Silane-Coated, Water-Soluble Quantum Dots**" *Small* **2015**, *11*, 6091–6096; DOI: 10.1002/smll.201501886.

**6.** Chunyan Li, **Asra Hassan**, Preston Snee, Philippe Baveye and Christophe Darnault. "**Aggregation Kinetics and Stability of Organic Ligand-Quantum Dot Nanoparticle Complexes as a Function of pH**" (*submitted*).

7. Chunyan Li, **Asra Hassan**, Preston Snee, Philippe Baveye and Christophe Darnault. "**Interplay of Electrolytes and Organic Ligands on Heteroaggregation Kinetics and Stability of Quantum Dot Nanoparticle**" (*submitted*).

# APPENDIX

Copyright Clearance Center RightsLink®

Home | Create Account | Help

ACS Publications
Most Trusted. Most Cited. Most Read.

**Title:** Charge Carriers Modulate the Bonding of Semiconductor Nanoparticle Dopants As Revealed by Time-Resolved X-ray Spectroscopy

**Author:** Asra Hassan, Xiaoyi Zhang, Xiaohan Liu, et al

**Publication:** ACS Nano

**Publisher:** American Chemical Society

**Date:** Oct 1, 2017



**LOGIN**

**If you're a copyright.com user,** you can login to RightsLink using your copyright.com credentials.

Already **a RightsLink user** or want to learn more?

**PERMISSION/LICENSE IS GRANTED FOR YOUR ORDER AT NO CHARGE**

This type of permission/license, instead of the standard Terms & Conditions, is sent to you because no fee is being charged for your order. Please note the following:

- Permission is granted for your request in both print and electronic formats, and translations.
- If figures and/or tables were requested, they may be adapted or used in part.
- Please print this page for your records and send a copy of it to your publisher/graduate school.
- Appropriate credit for the requested material should be given as follows: "Reprinted (adapted) with permission from (COMPLETE REFERENCE CITATION). Copyright (YEAR) American Chemical Society." Insert appropriate information in place of the capitalized words.
- One-time permission is granted only for the use specified in your request. No additional uses are granted (such as derivative works or other editions). For any other uses, please submit a new request.

**Title:** Anomalous Perturbation of the O2 Sensitivity of Poly(aromatic) Hydrocarbons by Magnetic Quantum Dots

**Author:** Asra Hassan, Armen Shamirian, Xi Zhang, et al

**Publication:** The Journal of Physical Chemistry C

**Publisher:** American Chemical Society

**Date:** Feb 1, 2017



**PERMISSION/LICENSE IS GRANTED FOR YOUR ORDER AT NO CHARGE**

This type of permission/license, instead of the standard Terms & Conditions, is sent to you because no fee is being charged for your order. Please note the following:

- Permission is granted for your request in both print and electronic formats, and translations.
- If figures and/or tables were requested, they may be adapted or used in part.
- Please print this page for your records and send a copy of it to your publisher/graduate school.
- Appropriate credit for the requested material should be given as follows: "Reprinted (adapted) with permission from (COMPLETE REFERENCE CITATION). Copyright (YEAR) American Chemical Society." Insert appropriate information in place of the capitalized words.
- One-time permission is granted only for the use specified in your request. No additional uses are granted (such as derivative works or other editions). For any other uses, please submit a new request.

Copyright Clearance Center RightsLink®

Home | Create Account | Help

ACS Publications
Most Trusted. Most Cited. Most Read.

**Title:** Electronic Structure and Dynamics of Copper Doped Indium Phosphide Nanocrystals Studied with Time-Resolved X-ray Absorption and Large Scale DFT Calculations

**Author:** Asra Hassan, Xiaoyi Zhang, Cunming Liu, et al

**Publication:** The Journal of Physical Chemistry C

**Publisher:** American Chemical Society

**Date:** Apr 1, 2018





**PERMISSION/LICENSE IS GRANTED FOR YOUR ORDER AT NO CHARGE**

This type of permission/license, instead of the standard Terms & Conditions, is sent to you because no fee is being charged for your order. Please note the following:

- Permission is granted for your request in both print and electronic formats, and translations.
- If figures and/or tables were requested, they may be adapted or used in part.
- Please print this page for your records and send a copy of it to your publisher/graduate school.
- Appropriate credit for the requested material should be given as follows: "Reprinted (adapted) with permission from (COMPLETE REFERENCE CITATION). Copyright (YEAR) American Chemical Society." Insert appropriate information in place of the capitalized words.
- One-time permission is granted only for the use specified in your request. No additional uses are granted (such as derivative works or other editions). For any other uses, please submit a new request.

BACK | CLOSE WINDOW

**ROYAL SOCIETY OF CHEMISTRY LICENSE**
**TERMS AND CONDITIONS**

Mar 19, 2018

This Agreement between University of Illinois at Chicago ("You") and Royal Society of Chemistry ("Royal Society of Chemistry") consists of your license details and the terms and conditions provided by Royal Society of Chemistry and Copyright Clearance Center.

| | |
|---|---|
| License Number | 4312561062854 |
| License date | Mar 19, 2018 |
| Licensed Content Publisher | Royal Society of Chemistry |
| Licensed Content Publication | Physical Chemistry Chemical Physics |
| Licensed Content Title | A primer on the synthesis, water-solubilization, and functionalization of quantum dots, their use as biological sensing agents, and present status |
| Licensed Content Author | Christina Marie Tyrakowski,Preston Todd Snee |
| Licensed Content Date | Nov 11, 2013 |
| Licensed Content Volume | 16 |
| Licensed Content Issue | 3 |
| Type of Use | Thesis/Dissertation |
| Requestor type | non-commercial (non-profit) |
| Portion | figures/tables/images |
| Number of figures/tables/images | 1 |
| Format | print and electronic |
| Distribution quantity | 100 |
| Will you be translating? | no |
| Order reference number | |
| Title of the thesis/dissertation | Synthesis, Characterization, & Photophysical Investigations of Doped Semiconductor Nanocrystals |
| Expected completion date | May 2018 |
| Estimated size | 150 |
| Requestor Location | University of Illinois at Chicago<br>1550 S BLUE ISLAND AVE, Unit 401<br>4500 SES,Department of Chemistry<br><br>CHICAGO, IL 60607<br>United States<br>Attn: University of Illinois at Chicago |
| Billing Type | Invoice |
| Billing Address | University of Illinois at Chicago<br>1550 S BLUE ISLAND AVE, Unit 401<br>4500 SES,Department of Chemistry<br><br>CHICAGO, IL 60607<br>United States<br>Attn: University of Illinois at Chicago |

Total 0.00 USD

Terms and Conditions

This License Agreement is between {Requestor Name} ("You") and The Royal Society of Chemistry ("RSC") provided by the Copyright Clearance Center ("CCC"). The license consists of your order details, the terms and conditions provided by the Royal Society of Chemistry, and the payment terms and conditions.

RSC / TERMS AND CONDITIONS

INTRODUCTION

The publisher for this copyrighted material is The Royal Society of Chemistry. By clicking "accept" in connection with completing this licensing transaction, you agree that the following terms and conditions apply to this transaction (along with the Billing and Payment terms and conditions established by CCC, at the time that you opened your RightsLink account and that are available at any time at .

LICENSE GRANTED

The RSC hereby grants you a non-exclusive license to use the aforementioned material anywhere in the world subject to the terms and conditions indicated herein. Reproduction of the material is confined to the purpose and/or media for which permission is hereby given.

RESERVATION OF RIGHTS

The RSC reserves all rights not specifically granted in the combination of (i) the license details provided by your and accepted in the course of this licensing transaction; (ii) these terms and conditions; and (iii) CCC's Billing and Payment terms and conditions.

REVOCATION

The RSC reserves the right to revoke this license for any reason, including, but not limited to, advertising and promotional uses of RSC content, third party usage, and incorrect source figure attribution.

THIRD-PARTY MATERIAL DISCLAIMER

If part of the material to be used (for example, a figure) has appeared in the RSC publication with credit to another source, permission must also be sought from that source. If the other source is another RSC publication these details should be included in your RightsLink request. If the other source is a third party, permission must be obtained from the third party. The RSC disclaims any responsibility for the reproduction you make of items owned by a third party.

PAYMENT OF FEE

If the permission fee for the requested material is waived in this instance, please be advised that any future requests for the reproduction of RSC materials may attract a fee.

ACKNOWLEDGEMENT

The reproduction of the licensed material must be accompanied by the following acknowledgement:

Reproduced ("Adapted" or "in part") from {Reference Citation} (or Ref XX) with permission of The Royal Society of Chemistry.

If the licensed material is being reproduced from New Journal of Chemistry (NJC), Photochemical & Photobiological Sciences (PPS) or Physical Chemistry Chemical Physics (PCCP) you must include one of the following acknowledgements:

For figures originally published in NJC:

Reproduced ("Adapted" or "in part") from {Reference Citation} (or Ref XX) with permission of The Royal Society of Chemistry (RSC) on behalf of the European Society for Photobiology, the European Photochemistry Association and the RSC.

For figures originally published in PPS:

Reproduced ("Adapted" or "in part") from {Reference Citation} (or Ref XX) with permission of The Royal Society of Chemistry (RSC) on behalf of the Centre National de la Recherche Scientifique (CNRS) and the RSC.

For figures originally published in PCCP:

Reproduced ("Adapted" or "in part") from {Reference Citation} (or Ref XX) with permission of the PCCP Owner Societies.

HYPERTEXT LINKS

With any material which is being reproduced in electronic form, you must include a hypertext link to the original RSC article on the RSC's website. The recommended form for the hyperlink is http://dx.doi.org/10.1039/DOI suffix, for example in the link http://dx.doi.org/10.1039/b110420a the DOI suffix is 'b110420a'. To find the relevant DOI suffix for the RSC article in question, go to the Journals section of the website and locate the article in the list of papers for the volume and issue of your specific journal. You will find the DOI suffix quoted there.

LICENSE CONTINGENT ON PAYMENT

While you may exercise the rights licensed immediately upon issuance of the license at the end of the licensing process for the transaction, provided that you have disclosed complete and accurate details of your proposed use, no license is finally effective unless and until full payment is received from you (by CCC) as provided in CCC's Billing and Payment terms and conditions. If full payment is not received on a timely basis, then any license preliminarily granted shall be deemed automatically revoked and shall be void as if never granted. Further, in the event that you breach any of these terms and conditions or any of CCC's Billing and Payment terms and conditions, the license is automatically revoked and shall be void as if never granted. Use of materials as described in a revoked license, as well as any use of the materials beyond the scope of an unrevoked license, may constitute copyright infringement and the RSC reserves the right to take any and all action to protect its copyright in the materials.

WARRANTIES

The RSC makes no representations or warranties with respect to the licensed material.

INDEMNITY

You hereby indemnify and agree to hold harmless the RSC and the CCC, and their respective officers, directors, trustees, employees and agents, from and against any and all claims arising out of your use of the licensed material other than as specifically authorized pursuant to this licence.

NO TRANSFER OF LICENSE

This license is personal to you or your publisher and may not be sublicensed, assigned, or transferred by you to any other person without the RSC's written permission.

NO AMENDMENT EXCEPT IN WRITING

This license may not be amended except in a writing signed by both parties (or, in the case of "Other Conditions, v1.2", by CCC on the RSC's behalf).

OBJECTION TO CONTRARY TERMS

You hereby acknowledge and agree that these terms and conditions, together with CCC's Billing and Payment terms and conditions (which are incorporated herein), comprise the entire agreement between you and the RSC (and CCC) concerning this licensing transaction, to the exclusion of all other terms and conditions, written or verbal, express or implied (including any terms contained in any purchase order, acknowledgment, check endorsement or other writing prepared by you). In the event of any conflict between your obligations established by these terms and conditions and those established by CCC's Billing and Payment terms and conditions, these terms and conditions shall control.

JURISDICTION

This license transaction shall be governed by and construed in accordance with the laws of the District of Columbia. You hereby agree to submit to the jurisdiction of the courts located in the District of Columbia for purposes of resolving any disputes that may arise in connection with this licensing transaction.

LIMITED LICENSE

The following terms and conditions apply to specific license types:

Translation

This permission is granted for non-exclusive world English rights only unless your license was granted for translation rights. If you licensed translation rights you may only translate

this content into the languages you requested. A professional translator must perform all translations and reproduce the content word for word preserving the integrity of the article.

Intranet

If the licensed material is being posted on an Intranet, the Intranet is to be password-protected and made available only to bona fide students or employees only. All content posted to the Intranet must maintain the copyright information line on the bottom of each image. You must also fully reference the material and include a hypertext link as specified above.

Copies of Whole Articles

All copies of whole articles must maintain, if available, the copyright information line on the bottom of each page.

Other Conditions

v1.2

Gratis licenses (referencing $0 in the Total field) are free. Please retain this printable license for your reference. No payment is required.

If you would like to pay for this license now, please remit this license along with yourpayment made payable to "COPYRIGHT CLEARANCE CENTER" otherwise you will be invoiced within 48 hours of the license date. Payment should be in the form of a check or money order referencing your account number and this invoice number {Invoice Number}. Once you receive your invoice for this order, you may pay your invoice by credit card. Please follow instructions provided at that time.

Make Payment To:
Copyright Clearance Center
29118 Network Place
Chicago, IL 60673-1291

For suggestions or comments regarding this order, contact Rightslink Customer Support: customercare@copyright.com or +1-855-239-3415 (toll free in the US) or +1-978-646-2777.

**Questions? customercare@copyright.com or +1-855-239-3415 (toll free in the US) or +1-978-646-2777.**